VELOCITY FIELD MEASUREMENTS IN THE NEAR WAKE OF A PARACHUTE CANOPY

by

Kenneth J. Desabrais

A Dissertation

Submitted to the faculty

of the

WORCESTER POLYTECHNIC INSTITUTE

in partial fulfillment of the requirements for the

Degree of Doctor of Philosophy

in

Mechanical Engineering

by

_____

April 2002

APPROVED:

_____

Dr. Hamid Johari, Major Advisor

_____

Dr. William W. Durgin, Committee Member

_____

Dr. James C. Hermanson, Committee Member

_____

Dr. Mayer Humi, Committee Member

_____

Dr. Nikolaos A. Gatsonis, Graduate Committee Representative

Abstract

The velocity field in the wake of a small scale flexible parachute canopy was measured using two-dimensional particle image velocimetry. The experiments were performed in a water tunnel with the Reynolds number ranging from $3.0 - 6.0 \times 10^4$. Both a fully inflated canopy and the inflation phase were investigated in a constant freestream (*i.e.* an infinite mass condition). The fully inflated canopy experienced a cyclic "breathing" which corresponded to the shedding of a vortex ring from the canopy. The normalized breathing frequency had a value of 0.56 ± 0.03. The investigation of the canopy inflation showed that during the early stages of the inflation, the boundary layer on the canopy surface remains attached to the canopy while the canopy diameter increases substantially. The boundary layer begins to separate near the apex region when the diameter is ~68% of the fully inflated diameter. The separation point then progresses upstream from the canopy apex region toward the canopy skirt. During this time period, the force rapidly increases to its maximum value while the separation point of the boundary layer moves upstream towards the skirt. The force then declines rapidly and the separated boundary layer rolls-up into a large vortex ring near the canopy skirt. At the same time, the canopy is drawn into an over-expanded state after which the cyclic breathing initiates. The unsteady potential force was estimated from the rate of change of the canopy volume. It contributed no more than 10% of the peak opening force and was only significant during the early stages of inflation. The majority of the opening force was the result of the time rate of change of the fluid impulse. It accounts for approximately 60% of the peak opening force. This result shows that the formation of the viscous wake is the primary factor in the peak drag force of the canopy.

Acknowledgements

The author would like to thank Dr. Hamid Johari for advising and supporting this research effort and also for being patient over the past eight years. The completion of the research was a result of his knowledge and excellent advice throughout my tenure at WPI. The author also needs to thank Dr. William W. Durgin, Dr. James C. Hermanson, Dr. Mayer Humi, and Dr. Nikolaos A. Gatsonis for serving on my graduate committee. Special thanks to Dr. Calvin Lee at the U.S. Army Natick Soldier Center for providing the data from the full-scale parachute and advice on the research. The author would also like to acknowledge the financial support of the U.S. Army Research Office under the grant number DAAG55-98-1-0171.

Special thanks goes to all my friends for their support and the entertaining distractions they provided to me at usually just the right time to prevent me from going insane. The author would like to thank the following people for their assistance and support: Sue Milkman, Bruce Plasse and the whole Plasse family, Marc Vadnais, Barbara Edilberti, Barbara Furhman, Janice Dresser, Pam St. Louis, Gail Hayes, Van Bluemel, Logan Yanson, Greg Rixon, Kellie Popp, Jim Usowicz, Frank Weber, Steve Derosier, Todd Billings, Sev Ritchie, Gary Adamowicsz, and Jim O'Rourke. The author would like to thank Derek Bond for developing the vortex tracking software and for some truly entertaining and thought provoking discussions on fluid dynamics. Also the author needs to thank Lee Evans for designing the electrical circuits used throughout the research.

And lastly, a very special thanks to my family and especially my parents for all their love and support. I would not have been able to complete this work without them providing me a reality check every now and then.

Table of Contents

List of Figures

List of Tables

Nomenclature

A_i	imaged area
C_D	canopy drag coefficient
C_{Du}	uncorrected drag coefficient
C_F	force coefficient
D_m	maximum projected diameter
D_o	canopy constructed diameter
D_p	mean projected diameter during steady descent
D'_{rms}	*rms*-value of the canopy diameter oscillations
D_{t2}	canopy diameter at time $t = t_2$
D_{t3}	canopy diameter at time $t = t_3$
D_v	vent hole diameter
Δt	time separation between laser pulses
F	canopy force
$\overline{F}$	mean canopy force
F'_{rms}	*rms*-value of the canopy force
F_p	canopy force due to the unsteady potential flow
$(F_p)_{rms}$	*rms*-value of the canopy force due to the unsteady potential flow
F_ω	canopy force due to vorticity
g	gravity
H	canopy height
$\mathbf{I}$	unit tensor
k_p	proportionality constant for potential flow
K_M	blockage factor
l_s	suspension line length
m_a	apparent mass
m_i	mass of fluid enclosed by the parachute canopy
m_p	mass of parachute canopy
m_s	mass of the suspend payload
$\hat{n}$	outward normal

q_o	dynamic pressure
q_{ou}	uncorrected dynamic pressure
r	radial distance
Re_{Do}	Reynolds number based on constructed diameter ($U_\infty D_o/\nu$)
s	path of integration
S	canopy area
S_o	surface area of canopy (*i.e.* $\pi D_o^2/4$)
S_p	projected area of canopy
S_T	cross-sectional area of tunnel test section
St	Strouhal number
$\mathbf{T}$	traction tensor
t	time
t_2	time when boundary layer first separates from canopy
t_3	time when boundary layer separates from canopy skirt
t_f	filling time
t_f^*	normalized filling time ($t_f U_\infty/D_o$)
t_{max}	time at maximum diameter
t_{max}^*	normalized t_{max} ($t_{max} U_\infty/D_o$)
t_o	opening time
t_o^*	normalized opening time ($t_o U_\infty/D_o$)
U_∞	freestream velocity
$\vec{u}$	velocity vector
$\vec{u}_s$	surface velocity
u	system velocity
u_c	vortex celerity
u_r	radial velocity of fluid
u_z	axial velocity of fluid
U'_{rms}	*rms*-value of freestream velocity fluctuations
u_{ti}	tangential velocity component at an interior canopy position
u_{tr}	tangential velocity component at a reflected interior canopy position

u_{ni}	normal velocity component at an interior canopy position
u_{nr}	normal velocity component at a reflected interior canopy position
V	volume enclosed by canopy
V_{steady}	volume enclosed by canopy at steady descent
$\dot{V}$	rate of change of enclosed canopy volume (dV/dt).
$\overline{V}$	mean canopy volume in steady descent
V'	volume fluctuations in steady descent
$(\dot{V}')_{rms}$	*rms*-value of the time rate of change of the volume fluctuations
$\vec{x}$	position vector

Greek Symbols

α_{fb}	forebody wake correction factor
ε^{sb}	solid blockage
Γ	circulation
ρ	fluid density
$\rho_{x,y}$	correlation coefficient
τ	normalized time (t/t_o)
τ_2	normalized separation time (t_2/t_o)
τ_3	normalized separation time (t_3/t_o)
ν	kinematic viscosity
$\vec{\omega}$	vorticity ($\nabla \times \vec{u}$)
ω_θ	azimuthal component of vorticity

1. Introduction

1.1 Literature Review

The kinematics and dynamics of a parachute system incorporate many facets of the engineering field from the fluid dynamics of the canopy to the structural mechanics of the suspension lines and the devices used to attach the payload to the parachute. The flow physics around the canopy is perhaps one of the least understood components of the parachute system. For instance, the connection between the large opening force (*i.e.* the opening shock) and the fluid kinematics that produce it has not been extensively examined. What flow field phenomena primarily contributes to the opening force? Does the force come primarily from the acceleration of the fluid due to increasing canopy size (an added mass effect) or are wake effects responsible? Similar questions can be posed about how the flow physics affects the inflation time of the canopy or are there any dominate shedding frequency from a fully inflated canopy. This research attempts to add to the understanding of the flow physics of a parachute.

The idea of using a device to aerodynamically decelerate the fall of an object has been around for centuries. The first known formal depiction of such a device was done by Leonardo Da Vinci in the late 15th century when he sketched a drawing of rigid framed canvas pyramid from which a person was suspended below it. Although there is no evidence that Da Vinci ever attempted to use his design, the design he proposed was recently shown to work when a British skydiver constructed and used a Da Vinci inspired parachute to safely descend from a hot air balloon at 10,000 feet (Carrington, 2000). It is generally acknowledged that the first use of parachutes occurred in the late 18th century where the first documented case of using a parachute to escape an exploding hot air

balloon in a basket over Paris was by Andre-Jacques Garnerin in October 22, 1797. After which he made many more jumps to entertain crowds of people. Until the early 20th century, parachutes were mainly used as entertainment devices and had very little practical uses.

With the advent of modern flight, it was realized that parachutes could be put into more practical purposes. This eventually resulted in the need for formal studies into the dynamics of parachutes. G.I. Taylor performed early experiments on the use of a parachute as a brake to shorten the landing distance of an aircraft in 1915 which expanded into a study of the shape of a parachute canopy (Taylor, 1963). Müller (1927) proposed an inflation process based on the enclosed volume of the parachute using the theory of the conservation of mass. He concluded that the parachute inflated in a constant distance for geometrically similar canopies (*i.e.* canopies that have similar geometric construction). This leads directly to the concept of an inflation time for a given speed and parachute. It was from these conclusions that many theories were developed based on an opening or filling time (O'Hara, 1949; French, 1963; Heinrich, 1969; Heinrich & Noreen, 1970; Heinrich, 1972; Payne, 1973). These theories did not rely on the details of the flow around the canopies, just the time it took to inflate the canopy based on various assumptions about the canopy shape and the inlet/outlet conditions.

In these theories, the force is estimated from application of Newton's second law (Heinrich , 1969),

$$m_s \frac{du}{dt} = m_s g - \frac{1}{2}\rho C_D S u^2 - u\left(\frac{dm_i}{dt} + \frac{dm_a}{dt}\right) - \left(m_p + m_i + m_a\right)\frac{du}{dt} \qquad 1.1$$

where m_s is the mass of the suspended payload, m_i is the mass of the fluid enclosed or included by the canopy, m_p is the mass of the canopy, m_a is the apparent mass, u is the system velocity, C_D is the drag coefficient of the canopy, S is the area of the canopy, and ρ is the density of the fluid. The two unsteady mass terms are the included mass and the apparent mass. Each of these unsteady mass terms is proportional to the enclosed volume of the canopy,

$$u\frac{dm}{dt} \propto \rho u\dot{V} \tag{1.2}$$

where $\dot{V}$ is the time derivative of the enclosed volume. For the time rate of change of the included mass, the proportionality constant is equal to one while the proportionality constant for the apparent mass depends on the geometry of the canopy. The apparent mass (or sometimes called the virtual mass) of the flow is based on the assumption of potential flow around the canopy. The model in Eq. 1.1 then requires any viscous effects to be accounted for in the u^2 drag coefficient term. However, it has traditionally been assumed that the drag coefficient (derived from experimental data) is constant. Any transient behavior is therefore associated with the rate of change of the unsteady mass terms and the deceleration of the system. The parachute can inflate under two possible conditions, either a finite or an infinite mass condition. During a finite mass inflation, the velocity of the system decays as the parachute inflates. However during an infinite mass inflation, the velocity does not decay and remains (nearly) constant during the inflation; the parachute behaves as if an infinite mass is attached to the parachute. This implies that under an infinite mass inflation or while the parachute is in steady descent, the last term listed in Eq. 1.1 can be neglected since $du/dt \to 0$. Therefore, during an infinite mass

inflation, this model assumes any unsteadiness is associated with the time rate of change of the mass terms (*i.e.* the rate of change of the enclosed canopy volume).

Theories have been developed for estimates of the apparent mass of the flow around the canopy during a finite mass inflation (Ibrahim, 1967; Eaton, 1983; Yavuz, 1989). The models assume a rigid canopy and the unsteadiness in the apparent mass is associated only with the deceleration of the canopy since the enclosed canopy volume does not change in the models. These models oversimplify the complex fluid dynamics and kinematics of the parachute inflation process. From a parachute designers standpoint, these simplification are justified for the prediction of the parameters such as inflation time and the maximum opening forces. The research has primarily focused on obtaining these parameters from analytical theories as well as experimental data (French, 1964; Knacke, 1992; Wolf, 1999). The existing theories provide reasonable results for well known canopy geometries and conditions but are limited in new situations. However, from an aerodynamic view point, these simplifications and theories obscure the flow physics that drive the canopy inflation process.

The limitations of the inflation time theories was recognized by Müller (1927) when he acknowledged the flow around the canopy was turbulent and separated but he applied simplifying assumption to eliminate the difficulties introduced by these flows. Studies and mathematical models for parachutes systems (*i.e.* the canopy and payload combination) have been developed which acknowledge and account for the unsteady flow conditions that the canopy encounters during inflation (Wolf, 1974; McVey & Wolf, 1974; Purvis, 1982) but still do not provide much insight into the details of the flow field around the canopy itself.

The canopy inflation has been modeled in the past by replacing the canopy surface with a vortex sheet (Klimas, 1972, 1977, 1979; Reddy, 1974). Another modeling method used a starting vortex that was placed near the canopy skirt and the flow field was allowed to develop (Roberts, 1974). These methods have been utilized in more recent numerical studies as computational methods and practices have evolved with the modern digital computer. A review of some of the methods used for numerically calculating the canopy inflation process and bluff body flows in general was given by Peterson *et al.* (1996). Recently, computational algorithms have been developed to solve the three-dimensional Navier-Stokes equations with fluid-structure interaction between the canopy and the surrounding fluid (Stein, 1999; Stein *et al.*, 1999; Stein *et al.*, 2000). These computational models are currently limited to only modeling a fully inflated parachute canopy. Additionally, studies have been performed to examine and model the structural dynamics of the canopy material in the flow field (Accorsi *et al.*, 1999). However, almost no experimental data exists to verify the fidelity of either the structural or fluid dynamic simulations.

Few experimental studies have been performed that measure specific flow field parameters around a parachute canopy either during inflation or once it has reached a steady state condition. DeSantis (1970) measured the flow entering and in the wake of an inflating canopy using a hot-wire probe along a radial at a few cross-sectional planes. Klimas (1973) and Klimas & Rogers (1977) measured the velocity field of an inflating canopy using a helium bubble survey which provided mean isovelocity contours around the canopy. The measurement of the pressure distribution of a fully inflated parachute canopy was conducted by Pepper & Reed (1976) in which they showed the integrated

pressure provided a reasonable estimate of the drag force. The only other known measurement of the velocity field around an inflating parachute model was conducted by Lingard (1978). He was able to measure several tens of velocity vectors around an inflating small scale parachute model in both a water tow tank and a wind tunnel. The limited resolution of the measurements however precluded computations of the vorticity or the integrated measures of the flow such as circulation or impulse.

A study of the flow past a slotted bluff body model in a constant freestream was performed by Higuchi (1989) which showed the effects porosity of the body has on the overall characteristics of the body wake. Studies of the wakes around rigid three-dimensional bluff bodies that at least qualitatively should behave similarly to parachutes (*i.e.* disks and cups) in steady and accelerating flows have been performed to understand the unsteady flow field around these bodies (Roberts, 1980; Higuchi, 1991; Higuchi *et al.*, 1996; Higuchi *et al.*, 1996; Lamberson *et al.*, 1999). The rigid nature of these bodies though limit the applicability of these flows to the flow around a flexible parachute canopy.

1.2 Objectives

The objectives of the research is to investigate the fluid dynamics of a flexible parachute canopy and how these characteristics affect the behavior of the canopy. A review of the available literature shows that knowledge of the flow field evolution around a canopy is limited and not well understood. So the aim of the study is summarized as

- measure the temporal evolution of the velocity field (and by extension the vorticity field) in the near wake of a flexible canopy both during an infinite mass inflation and once the canopy is fully inflated,
- obtain simultaneous measurements of the canopy shape and drag that are correlated with the velocity field measurements,
- identify any features of the flow field that affect the behavior of the canopy both during the inflation of the canopy (particularly around the time of the peak opening force) and once it is fully inflated,
- examine whether the primary source of the drag force is the result of an unsteady potential flow (*i.e.* an apparent mass effect from the change in the enclosed canopy volume) or the formation of a turbulent wake behind the canopy.

To accomplish these objectives, small scale parachute canopies were constructed for testing in the WPI water tunnel facilities. The particle image velocimetry technique along with image processing routines are used to measure the evolving velocity field in the near wake region of the inflating canopy models. From these measurements, the connection between the flow field and the canopy dynamics and motion are examined.

1.3 Full Scale Parachute Inflation

The inflation of a full-scale parachute develops in a few stages. Inflation of a 64-ft. round full-scale canopy is shown in Fig. 1.1. Initially, the cargo is released from the aircraft with the main parachute packed into a deployment bag. Attached to the deployment bag is a small parachute (usually called a drogue chute) that pulls the

deployment bag off the main parachute canopy. The process of the drogue chute extracting the main parachute is photographed in the first four images of Fig. 1.1. Once the deployment bag has been removed, the main parachute resembles a collapsed sock or hose. Air begins to enter the mouth or skirt area of the parachute causing the entrance region of the canopy to form into a cylindrical shape while the upper or crown region of the canopy remains in a collapsed state. The air being forced into the canopy mouth causes the canopy material to expand into a cylindrical shape along the whole length of the canopy with the crown region having a hemi-spherical shape. At this point, air begins to collect at the apex region of the canopy causing the canopy material to bulge while the skirt region remains collapsed in a cylindrical shape. The maximum diameter of the inflating canopy is in the bulging region of the canopy. The air continues to accumulate in the apex region of the canopy further increasing the size of the bulge in both axial and transverse directions. The axial expansion of the bulge starts from the apex region of the canopy and moves towards the canopy skirt. The canopy continues to expand or inflate until it reaches its fully inflated size (the last two images in Fig. 1.1) and the maximum canopy diameter is realized at the skirt. The canopy diameter however continues to grow beyond this point into an over-expanded state (not shown in Fig. 1.1). During the over-expanded state, the canopy achieves its maximum diameter and the canopy apex region becomes partially collapsed or buckled as the canopy skirt is drawn out into the over-expanded state. After the over-expansion, the canopy size decreases to a shape similar to that seen in the last frame of Fig. 1.1. By this time, the canopy has reached its steady descent mode and the parachute system develops a few new oscillation modes which depend on the design of the canopy and the overall parachute system. These modes could

include a symmetric breathing of the canopy itself and a helical oscillation of the entire parachute system around a common axis. The whole inflation process occurs in a time span of a few seconds.

A graph of the opening force that a full-scale parachute experiences during the inflation is shown in Fig. 1.2. It should be noted that the force shown in Fig. 1.2 does not correspond to the images in Fig. 1.1. The force initially begins with a short sharp spike when the drogue chute pulls the canopy from the deployment bag and the suspension lines on the canopy are drawn taunt. The force then drops until the canopy begins to inflate and the force rapidly rises to its maximum value then declines to its steady descent drag value. The connection between the canopy shape and size and the force depends on whether the canopy inflates in a finite or infinite mass condition (Knacke, 1992). Recall during a finite mass inflation, the velocity of the parachute system decays as the parachute inflates. In this case, the canopy achieves its fully inflated shape (but has not yet over-expanded) at a time well after the peak opening force has occurred. In an infinite mass parachute inflation, the canopy diameter first becomes equal to the mean steady state diameter at approximately the same time the peak opening force occurs. It should not be assumed that an infinite mass inflation is strictly a research condition, there are many examples of an infinite mass parachute inflation used in real applications. Parachutes are often used as a stabilizing component on payloads. These parachutes are opened at high speeds and help orientate the payload in a certain direction before larger parachutes are deployed which actually decelerate the payload. For example, planetary probes released from orbit often have small parachutes that deploy high in the atmosphere of the planet that act to stabilize the payload before larger parachutes are

deployed lower in the atmosphere that decelerate the payload. Also, often extraction parachutes are used to pull payloads out of an aircraft. These extraction chutes open at the speed of the aircraft which remains constant and therefore the parachute inflates under an infinite mass condition.

1.4 Fluid Dynamic Forces

Lighthill (1986) has suggested that the force a body experiences in a fluid flow can be decomposed into vortex-flow forces and potential-flow forces. He further hypothesized that the vortex forces are proportional to the time derivative of the flow impulse over the wake of the body. An *exact* expression for obtaining the instantaneous force exerted on a body by the fluid was developed by Noca *et al.* (1999). This expression requires knowledge of only the velocity field (and therefore by extension the vorticity field) in a finite region around the body. No knowledge of the pressure field is necessary. This is particularly useful in this research since the PIV measurements of the velocity field provide no knowledge of the pressure field. The aerodynamic force per unit mass of a body with an unsteady, arbitrary shape, using the control volume shown in Fig. 1.3, is

$$\begin{aligned}\frac{\vec{F}}{\rho} = &-\frac{1}{N-1}\frac{d}{dt}\iiint_{V_f(t)} \vec{x}\times\vec{\omega}\,dV \\ &+\frac{1}{N-1}\frac{d}{dt}\oint_{S_b(t)} \vec{x}\times\left(\hat{n}\times\vec{u}\right)dS - \oint_{S_b(t)} \hat{n}\cdot\left(\vec{u}-\vec{u}_s\right)\vec{u}\,dS \\ &+\oint_{S_f(t)} \hat{n}\cdot\vec{\gamma}\,dS\end{aligned} \qquad 1.3$$

where

$$\vec{\gamma} = \frac{1}{2}u^2\mathbf{I} - \vec{u}\vec{u} - \frac{1}{N-1}(\vec{u} - \vec{u}_s)(\vec{x} \times \vec{\omega}) + \frac{1}{N-1}\vec{\omega}(\vec{x} \times \vec{u}) + \frac{1}{N-1}\left[\vec{x} \cdot (\nabla \cdot \mathbf{T})\mathbf{I} - \vec{x}(\nabla \cdot \mathbf{T})\right] + \mathbf{T} \quad . \tag{1.4}$$

and V_f is the volume of the control volume, S_b is the surface area of the body, and S_f is the surface of the control volume (Noca, 1999). In Eq. 1.3 and Eq. 1.4, the position vector is given as $\vec{x}$, the velocity in the control volume is $\vec{u}$, the vorticity is $\vec{\omega}$, the outward normal unit vector is $\hat{n}$, and N is the dimension of space ($N = 3$ for three dimensional flows and $N = 2$ for two dimensional flows). The velocity of the body surface is denoted as $\vec{u}_s$, the unit tensor is **I**, and the traction tensor is **T**. This relationship requires detailed knowledge of the flow at and near the body surface as well as the velocity on the body surface. An alternative form of this expression is given when the body contains a fluid of a known flow pattern. It is given by Noca (1996) as

$$\vec{F} = -\frac{1}{2}\frac{d}{dt}\iiint_{V_f(t)} \rho \vec{x} \times \vec{\omega}\, dV + \frac{d}{dt}\iiint_{V(t)} \rho \vec{u} dV - \frac{1}{2}\frac{d}{dt}\iiint_{V(t)} \rho \vec{x} \times \vec{\omega}\, dV + \oint_{S_f(t)} \rho \hat{n} \cdot \vec{\gamma}\, dS \tag{1.5}$$

where V is the volume of the body and we have assumed a three-dimensional flow. Examination of each term on the right-side of Eq. 1.5 shows that this relation can be simplified further for its use in this study.

The first term on the right-side of Eq. 1.5 is the time derivative of the impulse of the flow in the control volume where the impulse is defined as

$$\vec{I} \equiv -\frac{1}{2}\iiint_{V_f(t)} \rho \vec{x} \times \vec{\omega}\, dV \, . \tag{1.6}$$

This term shows how the vortical portions of the external flow affect the force on the body. If we assume a cylindrical coordinate system, as shown in Fig. 1.4, the largest aerodynamic forces on the canopy will be those in the axial direction (*i.e.* the drag). Therefore, taking only the axial component of the impulse, Eq. 1.6 simplifies to

$$I_z = -\frac{1}{2}\iiint_{V_f} \rho r^2 \omega_\theta dr d\theta dz \tag{1.7}$$

where r is the radial distance from the centerline of the canopy and ω_θ is the azimuthal component of the vorticity. Further, if we assume incompressible and axisymmetric flow then, the axial impulse reduces to

$$I_z = -\pi\rho\iint r^2 \omega_\theta dr dz\,. \tag{1.8}$$

Therefore, the drag force associated with the impulse of the flow around the canopy (*i.e.* the vortical force) is given as

$$F_\omega = \frac{dI_z}{dt} = -\pi\rho\frac{d}{dt}\iint r^2 \omega_\theta dr dz\,. \tag{1.9}$$

Therefore, the vortical force can be altered by either changing the amount of vorticity in the flow or by moving the vorticity radially in the flow. It should be noted, that in this study, the velocity field was measured in a two-dimensional plane that was parallel to the centerline of the canopy. It was therefore only possible to calculate the azimuthal component of the vorticity. Also, forces in the radial and azimuthal directions can be estimated from the time derivatives of the impulse in these directions. However, it is necessary to know the vorticity in the radial and axial directions (which are not known in these experiments) to calculate these forces.

The second term on the right-side of Eq. 1.5 can be related to the unsteady potential flow around the canopy. The velocity in the integrand is the velocity of the fluid interior to the body, in this case, the velocity of the fluid inside the inflating canopy. As a limiting case, since the canopy material is nearly impermeable to flow through it, the maximum velocity on the canopy interior is expected to be no more than the freestream velocity, U_∞. Assuming the interior velocity remains approximately uniform and constant, then this term reduces to

$$\frac{d}{dt}\iiint \rho \vec{u} dV \le \rho U_\infty \frac{dV}{dt} = \rho U_\infty \dot{V} \tag{1.10}$$

This result is reasonable since it can be shown that the drag of a translating, expanding sphere in an inviscid flow is proportional to the rate of change of the volume of the sphere (Karamcheti, 1980 and Panton, 1996). However, Eq. 1.10 is a limiting case since the average velocity on the interior is expected to always be less than the freestream velocity. The flow should either stagnate on the interior of the canopy (Lamberson *et al.*, 1999) or at most a recirculation region may establish itself inside the canopy. This recirculation would introduce vorticity into the interior flow but the magnitude of the maximum interior velocity is expected to be on the order of the freestream velocity. Introducing a proportionality constant, k_p, of order one to account for the limiting case analysis, the force due to the unsteady potential flow would be

$$F_p = k_p \rho U_\infty \dot{V} \tag{1.11}$$

where k_p is taken to be one in our calculations.

The third term is related to the impulse of the interior flow. Since measurements of the interior flow were not possible in the experiments, we have no knowledge of the

vorticity in this region. Again this region of the flow would be a stagnation point, so even if there is considerable vorticity contained in the region, it would not be expected to change rapidly with time and the derivative of the interior impulse is expected to be small. Based on this assumption, this term in Eq. 1.5 will be neglected.

Finally, the last term of Eq. 1.5, relates to the flow at the outer surface of the control volume. The control volume used in the calculation should be as large as possible so as to contain the vorticity in the wake and also to place as much of the control surface in the freestream. However, due to the experimental setup portions of the control volume used in the calculations (namely, the flow upstream of the canopy) are located in regions where the velocity is not well defined. This term can also be decomposed into viscous terms and other terms that contain velocity and vorticity. Since this portion of the control volume will be far from the body, viscous effects will be small since the flow will be inviscid in this region. It is expected that the primary forces the body experiences will be from the time derivative of the impulse near the body and all the other terms will be neglected. Therefore, the aerodynamic forces that the canopy experiences can be estimated by

$$F = F_p + F_\omega \approx k_p \rho U_\infty \dot{V} - \pi\rho \frac{d}{dt} \iint r^2 \omega_\theta dr dz \,. \qquad 1.12$$

Based on this relationship, the drag can be estimated from measurements of the velocity field in the wake of the canopy and the volume enclosed by the canopy. This estimate can then be compared to direct drag measurements and the significance of the various flow field features can be established.

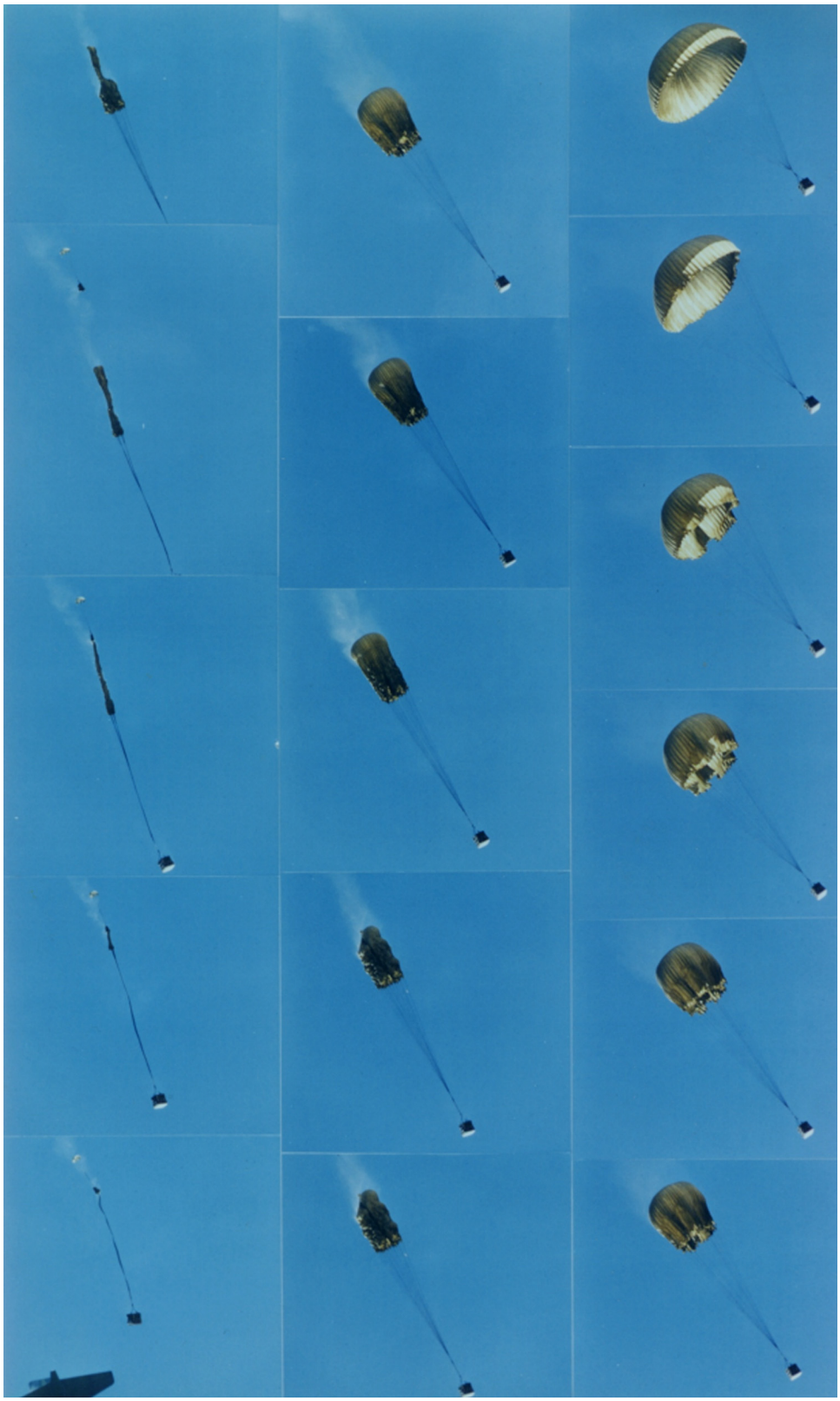

Figure 1.1. Images of a full scale parachute inflation (Lee, 1998).

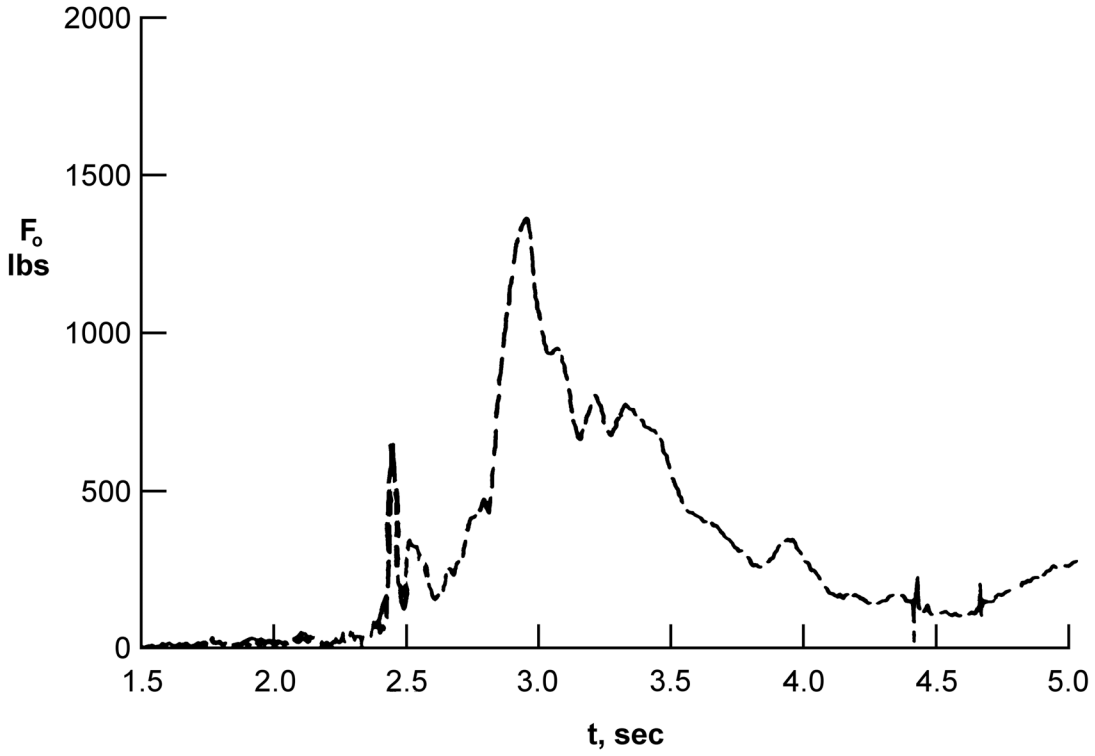

Figure 1.2. Opening force during full scale parachute inflation (adapted from Lee, 1994).

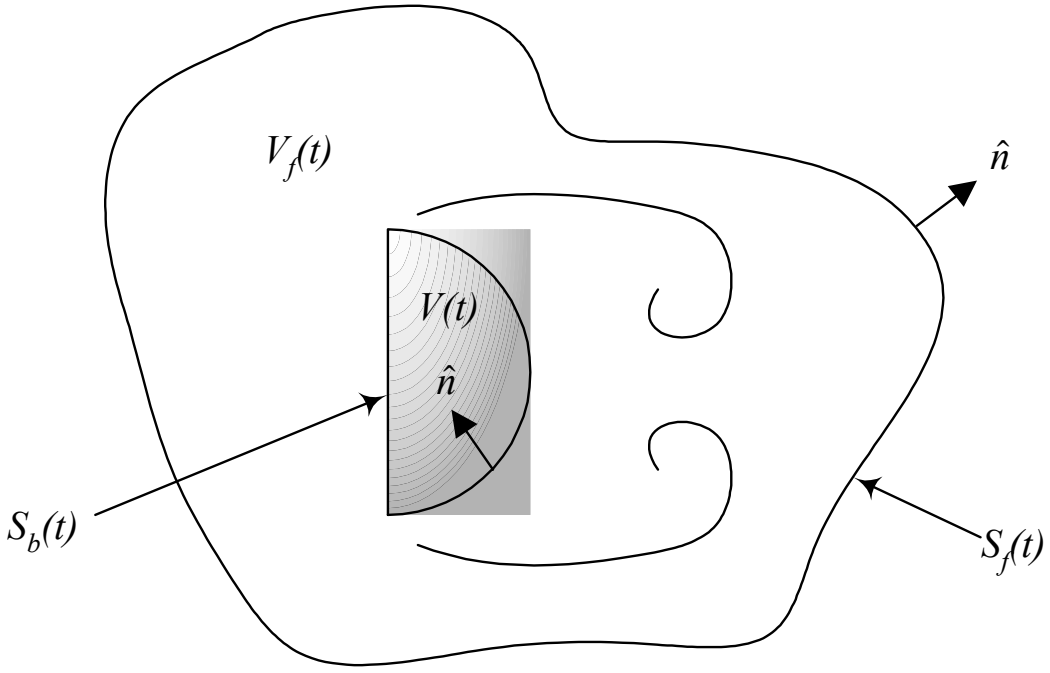

Figure 1.3. Control volume used for calculation of aerodynamic forces.

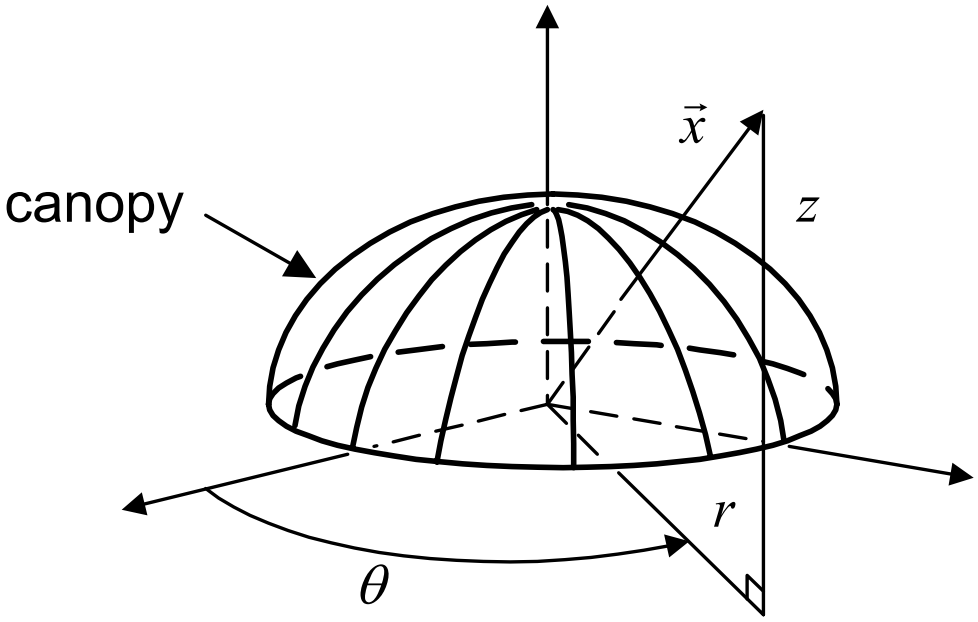

Figure 1.4. Cylindrical coordinate system for canopy.

2. Experimental Setup

2.1 Water Tunnel Apparatus

The experiments were conducted in the WPI free-surface water tunnel facilities. A schematic of the experimental setup is shown in Fig. 2.1 and photographs of the experimental setup are shown in Fig. 2.2. The experiments were conducted in the water tunnel to aid in the measurement of the velocity field around the canopy. The velocity field measurements were made using the Particle Image Velocimetry (PIV) technique. The PIV technique is more easily implemented in water than air. Also in water, longer inflation times were achieved for the canopies tested than would be achieved if the tests were performed in a wind tunnel. The water tunnel test section has internal dimensions of 0.6 m wide by 0.6 m deep by 2.4 m long. The water tunnel was operated at the nominal speeds listed in Table 2.1. The actual speeds, U_∞, were measured using a Laser Doppler Velocimetry (LDV) system which also provided a measure of *rms*-value of the velocity fluctuations, U'_{rms}. These measurements were taken along the tunnel centerline approximately 0.5 m downstream of the test section entrance.

Table 2.1. Freestream velocities in water tunnel.

Nominal U_∞ (cm/s)	Actual U_∞ (cm/s)	U'_{rms}/U_∞
20	19.622	1.19%
25	24.585	1.16%
30	29.328	1.23%
35	34.452	1.05%
40	39.134	1.29%

The parachute assembly was attached to a stationary streamlined forebody in the water tunnel (see Fig. 2.3). This placed the parachute assembly in a horizontal orientation. The forebody had a diameter of 1.4 cm and a length of approximately

17.5 cm. By keeping the forebody streamlined and minimizing its dimensions, the wake effects were also kept to a minimum. Flow visualization was performed to confirm that the forebody wake minimally affected the parachute. The forebody was supported by 0.64 cm diameter rods in the center of the water tunnel test section and approximately 60 cm downstream of the test section entrance.

For the canopy inflation experiments, the canopy was packed into a round deployment tube downstream of the forebody which was pulled away to start the inflation process. The canopy packing process is explained in the next section. The ratio of deployment tube diameter to constructed canopy diameter, D_o, was fixed at 7%. The deployment tube was pulled away by a thin nylon string which passed through a series of pulleys and was attached to a stepper motor (see Fig. 2.4). The stepper motor extracted the deployment tube at a time which was synchronized with the force measurement and the imaging systems. The details of the synchronization and stepper motor control are presented in Section 2.4. The tube was pulled at a speed of approximately 65 cm/s.

2.2 Canopy Specifications

The parachute models were constructed using a solid cloth, flat circular geometry. The canopies studied had constructed diameters of 15.2 cm and 30.5 cm. A diagram of the canopy geometry along with definitions of the dimensions associated with the canopy is shown in Fig. 2.5. The canopies tested had no vent hole. A Reynolds number, Re_{Do}, based on the constructed diameter is

$$Re_{Do} = \frac{U_\infty D_o}{\nu}, \tag{2.1}$$

where ν is the kinematic viscosity of water ($\nu = 0.01$ cm^2/s). Table 2.2 lists the Reynolds numbers as well as the water tunnel solid blockage, ε^{sb}, for the canopies and velocities tested under a steady state condition. For blockages of 10% or less (Cockrell, 1987), corrections for the dynamic pressure were applied for the data measured in the steady state canopy experiments (Macha and Buffington, 1989). The dynamic pressure, q_o, was corrected as

$$q_o = q_{o_u}\left[1 + K_M \frac{C_{D_u} S_p}{S_T}\right] \qquad 2.2$$

where q_{ou} is the uncorrected dynamic pressure, K_M is a blockage factor derived from previous experimental data (Macha and Buffington, 1989), C_{Du} is the uncorrected drag coefficient of the canopy, S_p is the projected area of the canopy diameter, and S_T is the cross-sectional area of the tunnel test section. No corrections were applied to the canopy inflation experiments primarily due to the low blockage that occurs during most of the inflation process.

Table 2.2. Reynolds number and solid blockage.

U_∞ (cm/s)	D_o (cm)	$Re_{Do} \times 10^{-4}$	ε^{sb}
20	15.2	2.98	2.5%
25	15.2	3.73	2.5%
30	15.2	4.45	2.5%
35	15.2	5.23	2.5%
40	15.2	5.94	2.5%
20	30.5	5.96	9.9%

Full-scale canopies have dimensions on the order of 10-30 m, thus the canopies in this study are on a very small geometric scale which naturally leads to the question of Reynolds number and scale effects. Typically full scale canopies descend at a speed of 5-

10 m/s which would result in a Reynolds number on the order of 10^6-10^7. These values are very difficult to achieve in any laboratory setting especially in a water tunnel. Knacke (1992) shows that Reynolds number has little effect on the drag of a canopy over the range of Reynolds number 10^5-10^6. The present research was limited to the Reynolds number range listed in Table 2.2 due to the limitations of the experimental facilities. Scale effects are an important characteristic of parachute modeling. Heinrich and Hektner (1971) and Lee (1989) showed that the canopy flexibility is an important characteristic. The overall performance of the canopy is affected by the stiffness of the canopy. However, given the proper scaling parameters, the scale effects can be accounted for in the inflation characteristics (Johari and Desabrais, 2001).

The significant scale difference also introduces technical difficulties in the construction of the canopy models. New methods were needed for constructing the canopy models. Traditional full-scale parachute canopies are constructed by sewing individual panels or "gores" together to form an approximate circular geometry (Knacke, 1992). Constructing the canopy models in this method would result in the models having larger than necessary stiffness due to the sewing seams along the edge of each gore. In order to minimize the stiffness effects at these small scales, it was decided that the canopy should be made from one solid piece of material instead of individual gores being sewn together. The parachutes were constructed from standard 1.1 oz/yd^2 rip-stop nylon and manufactured by cutting the material around a flat circular template at the appropriate diameter. The edge of the nylon material was seared, preventing it from fraying. An image of the canopy edge between two suspension lines in shown in Fig. 2.6.

The permeability of the canopy material is characterized by the mean flow across the canopy material. This flow velocity through the material is a function of the pressure differential and the material pore size. An estimate of the pressure differential can be made based on the dynamic pressure. A full size parachute descents at ~6 m/s in air ($\rho = 1.2$ kg/m^3) which results in a dynamic pressure of ~22 Pa. The small scale models were placed in a freestream of 20 cm/s in water ($\rho = 1000$ kg/m^3) which results in a dynamic pressure of ~20 Pa. This shows that the scale models in water operate at similar dynamic pressures regimes as full scale canopies where the permeability characteristics of full scale canopies is well known. It is therefore expected that the small scale model permeability characteristic will be similar to those of the full scale canopies. However it should be noted that the viscosity of air and water differ by two orders of magnitude which may effect the permeability characteristics of the material.

The suspension lines were made from 100 μm diameter nylon thread. The length of the suspension lines, l_s, was approximately equal to the constructed diameter of the parachute canopy, *i.e.* $l_s \cong D_o$. It was decided that the number of suspension lines on each parachute assembly should be 24. This number was based on early preliminary experiments in which only 8 or 12 suspension lines were used. The low number of suspension lines caused significant bulging or "ballooning" of the canopy between the suspension lines. By increasing the suspension line count to 24, the inflated canopy shape qualitatively matched those observed on full-scale parachutes. Full-scale parachutes typically have 16-28 suspensions lines (Knacke, 1992).

The suspension lines were attached to the canopy by creating a small loop at the end of the suspension line that was passed through a hole near the edge of the canopy

skirt (see Fig. 2.6). The loop in the suspension line was created using a bowline knot (Bigon and Regazzoni, 1982). The hole in the canopy was seared again to reduce the potential for fraying. The other ends of the suspension lines were attached to a parachute mount. The mount was designed to allow for the adjustments of the length of each suspension line separately (see Fig. 2.3). This ensured that all the suspension lines were of equal length. The parachute mount was attached to the end of the forebody, which was also the end of a load cell used to measure the force the canopy experienced.

Based on the measured force the canopy experiences, the maximum force occurs during the inflation of the canopy (see Chapter 4). The highest peak opening force was approximately 6 N. This results in a stress of approximately 32 MPa (4600 psi) in each suspension line. This results in an estimated elongation of the suspension lines (based on stress-strain curves for nylon published in Bixby *et al.*, 1978) of ~0.03% (0.05 mm) which is negligible. It is therefore reasonable to assume the suspension lines as inelastic.

Flat circular canopy geometries are notorious for large off-axis oscillations when fully inflated. In order to minimize this motion, a thin (0.5 mm diameter) flexible nylon retention line was attached to the forebody and passed through the apex of the canopy. The end of the retention line was held rigidly far downstream of the canopy. The retention line applied the necessary force to restrain the canopy wandering but should not adversely affect other aeroelastic effects. At the apex of the canopies, a small (~5 mm diameter) hard grommet (see Fig. 2.7) was secured to the canopy material so as to allow a place for the retention line to pass through the material without substantially damaging or altering the canopy.

The packing of the canopy into the deployment tube for the inflation experiments consisted of drawing the canopy into a roughly cylindrical shape by hand with the water tunnel turned off. The canopy was then pushed into the deployment tube until the canopy was fully encased by the tube with only the suspension lines visible. The packed canopy (with the deployment tube) was then pulled to a position where the suspension lines were taunt. The water tunnel was then turned on and the freestream velocity was established in the test section after which the deployment tube was extracted to begin the inflation process. This packing process created difficulties in measuring the inflation process (mainly inflation times) since it resulted in inconsistent folding of the canopy material. The canopy packing had to be performed underwater to prevent air bubbles from being trapped inside the canopy. This reduced the ability to observe the packing process to a viewing plane above the canopy (*i.e.* the test section access point). The water also significantly reduced the ability to manipulate the canopy material into desired positions. The geometric scale of the canopies also prevented development of a method to fold the canopy in a repeatable and prescribed manner. However, preliminary experiments showed that the final packing method utilized, resulted in an overall inflation process that was symmetric and, given a large enough sample, statistically repeatable.

2.3 Imaging System

The experiments were recorded using a CCD camera to observe the development of the canopy geometry and the flow field surrounding the canopy. Sample images obtained from the experiments are shown in Fig. 2.8. The camera was mounted at a right angle to the parachute assembly so as to view it from the side. Also the camera was

mounted on its side so that in the images, the parachute assembly had a vertical orientation with the fluid flow from the bottom to the top of the image and gravity was directed to the right of the image. The camera used (a Pulnix model no. TM-1040) was a progressive scan 8-bit monochrome CCD camera with a 1k × 1k pixel resolution and a 30 Hz frame rate. A 24 mm lens was mounted on the camera with the *f*-number and the shutter speed set depending on the experiments to be recorded. The images were digitally transferred (in real-time) from the camera to the system memory of a PC through a video capture card (μTech model no. MV-1000/1100). The computer had 512 MB of RAM which allowed for approximately 450 frames (or ~15 s) to be recorded at the maximum camera resolution. Each recorded frame was then stored on the hard disk of the computer as a separate image file and subsequently transferred to compact discs for archival purposes.

The imaging of the experiments can be separated into two groups, one group in which only the canopy geometry was imaged and another group where the velocity field around the canopy was imaged. Each case required significantly different lighting requirements. For the former case, the water tunnel test section was back lit by a floodlight through a white diffuser screen mounted on the back of the water tunnel wall. This arrangement allowed for a clean white background behind the dark gray image of the canopy which creates a clear contrast between the background and foreground for use in image processing (see Fig. 2.8a). The *f*-number of the lens was set to a half-click less than the 5.6 setting and the shutter speed of the camera was set to 1/250 s. An image processing routine was developed to extract the temporal evolution of the maximum projected diameter, D_m, the canopy height, H, and an estimate of the volume enclosed by

the canopy, V, from each sequence of images. The uncertainty in the maximum projected diameter and the canopy height was ± 5 pixels $\approx 0.005\, D_o$ and the volume has an uncertainty of 15% estimated from the uncertainty of the diameter and height. The details of the image processing routine are given in Appendix A.

For the case of imaging the canopy and the velocity field around the canopy, the overall lighting requirements were dictated by the requirements of the Digital Particle Image Velocimetry (DPIV) system. In this case, the laser used in the DPIV system provided the illumination for the region of interest in the water tunnel. The overall details of the DPIV system are presented below; details of the laser orientation are presented here. The DPIV system uses a laser sheet to illuminate the flow field. The sheet originates in the upper right corner of the images towards the lower left corner and is parallel to the centerline of the canopy. The intersection of the laser sheet with the canopy caused part of the upper surface of the canopy to be brightly lit, providing a sharp contrast between the canopy edge and the dark background. However, the laser light did not completely penetrate through the material of the canopy which caused a shadow to be formed where the canopy blocked the laser sheet. The shadow can be seen directly below and in the lower left corner of the image in Fig. 2.8b. The *f*-number of the lens was set to 2.5 and no external shutter was used. The CCD was readout at a time of 1/60 s. The geometry of the canopy was extracted manually from these images. A simple closed polygon was manually selected to estimate the shape of the canopy at each instant of time throughout the sequence. An example of this is shown in Fig. 2.9. Also, the maximum projected diameter was manually measured from these image sequences. The uncertainty in the maximum projected diameter, measured by this method, was ± 10 pixels $\approx 0.01 D_o$.

2.4 Force Measurements

The force, F, measurements were made with a strain gage based load cell mounted in the stationary forebody (see Fig. 2.3). The load cell was mounted such that the only forces it measured were those being directly applied to the canopy through the suspension lines. The load cell was powered by two 9V batteries and the output voltage of the load cell was passed through a custom designed low noise amplifier. A wiring diagram of the amplifier is shown in Appendix B. The amplifier provided a gain of 200. The output voltage of the amplifier was measured by a 12-bit A/D data acquisition system (Data Translation model no. DT2805). The data was sampled at a rate of 150 Hz with no gain applied at the data acquisition card. The uncertainty of the force measurement system was 0.4% at full scale of the load cell or 0.027 N. This corresponds to approximately 10% of the smallest steady state drag force measured. The load cell was calibrated using static loads with the load cell mounted in place. The calibration was performed prior to and after a set of experiments was executed. Also, a measurement of the load cell output with zero applied load was performed prior to each sequence.

A body in front of a canopy tends to reduce the force a canopy experiences due to the wake from the body. Knacke (1992) suggests a linear correction (for a given downstream location of the canopy from the body) for these wake effects which were applied to the steady state canopy,

$$C_D = \frac{C_{D_u}}{\alpha_{fb}}, \qquad 2.3$$

where C_D is the drag coefficient and α_{fb} is the forebody wake correction factor which was set to 1.05 for the conditions tested in this research.

The force measurement system was synchronized with imaging system and the deployment tube extraction. A schematic of the synchronization system is shown in Fig. 2.10. The timing sequences of the various events during the deployment are shown in the upper left corner of Fig. 2.10. The deployment process began by pushing a one-shot button that simultaneously activated a small LED, positioned in the field of view of the camera (the LED can be seen in the upper left corner of the image in Fig. 2.8b), while at the same time sending a triggering signal to the data acquisition card, directing it to start recording data. This method allows for a synchronization uncertainty of ±½ frame or ±17 ms between the imaging system and the force measurement system. After a fixed delay of 1.0 s from when the data acquisition was activated, a signal was sent to the stepper motor controller causing it to pull the deployment tube away. The frequency generator connected to the stepper motor controller set the speed at which the stepper motor rotated. The details of the timing circuit for this synchronization and the specification of the other components are presented in Appendix B.

2.5 PIV System

The velocity field in the near wake of the canopy was measured using a DPIV system. The particulars of the DPIV method are described by Willert & Gharib (1991) and Raffel *et al.* (1998). A dual pulsed Nd:YAG laser was utilized in the experiments. The laser pulses were synchronized with the CCD camera frame rate, and the time separation, Δt, between successive pulses was established by a counter/timer board in a

PC. The time separation between pulses was set depending on the freestream velocity. Table 2.3 lists the pulse separations used at each speed as well as the area imaged, A_i, for each canopy.

Table 2.3. Laser pulse separation and imaging areas.

U_∞ (cm/s)	D_o (cm)	Δt (ms)	A_i (cm^2)
20	15.2	6.00	20.0 × 20.0
30	15.2	4.56	20.0 × 20.0
40	15.2	3.00	20.0 × 20.0
20	30.5	6.00	23.9 × 23.9

Each laser pulse had a duration of 5 ns and an energy output of approximately 15 mJ. The laser was pulsed at a frequency of 30 Hz that generated velocity fields at a rate of 15 Hz, due to the frame straddling method used in DPIV measurements. The laser pulses were directed through a negative cylindrical lens (focal length of - 6.35 mm) to create a laser sheet for illumination of the flow field directly behind the canopy. The laser sheet had a thickness of 4-5 mm and was oriented parallel with the freestream velocity. The flow field was seeded with neutrally buoyant silver-coated particles that had a mean particle diameter of 45 μm. Figures 2.8b and 2.9 provide good examples of the seeding density in the flow fields.

The DPIV vector processing algorithm used interrogation windows of 32 × 32 pixels with an overlap step of 8 pixels in each direction. This produces a discrete array of approximately 13700 velocity vectors per field. The spatial resolution of the velocity vectors was 1.7 mm for the experiments with the 15 cm canopy and 2.0 mm with the 30 cm canopy. The vector processing algorithm is outlined in Willert & Gharib (1991). The area of the velocity field measured was approximately 1.5 diameters

downstream of the canopy apex (refer to Table. 2.3). The origin of the coordinate system was defined as the bottom of the field of view along the centerline of the canopy. The uncertainty of the velocity vector is approximately 3% which is comparable to estimates made Willert & Gharib (1991).

The existence of a boundary in the images of the flow field (*i.e.* the canopy) causes the velocity vectors near the boundary to be calculated improperly. This is due to a deficiency of particles in the interrogation windows that contain a large portion of the imaged boundary with only a small region of the flow field itself imaged. A moving boundary only compounds the issue since the PIV processing algorithm may estimate a particle displacement that was corrupted by the motion of the boundary. In the images in this research, the canopy (*i.e.* the moving boundary) appears as a continuously varying gray-scale region that changes appearance in the image pair that is used to calculate the displacement vectors by the PIV processing algorithm. The processing algorithm calculates a corrupted displacement vector in and near the canopy region due to the changing pixel values of the canopy region in the image pair. In order to minimize this corruption effect, the pixel gray-scale level in the canopy region was set to black (the background color) in both images in the pair. Therefore, the only pixel motion seen in each interrogation window was that associated with the motion of the imaged particles. The region of the image where the canopy was located was selected by the process described in Section 2.3. It should be noted that this method of canopy region blackout does not necessarily establish the correct boundary condition at the canopy surface. The correct boundary condition would have to be imposed either pre- or post- processing of the images or velocity field. This would require knowledge of the boundary condition at

the canopy surface. However, the boundary condition at the canopy surface is not well known or established. It was therefore decided that no boundary condition would be imposed on the calculated velocity field at the canopy surface. It should also be stated that the flow field in the interior of the canopy is not measured.

The azimuthal vorticity, ω_θ, of the flow field was calculated from the velocity field using a method suggested in Raffel *et al.* (1998). The method estimates the average vorticity at a grid point in the field by evaluating the circulation around the eight neighboring points and dividing by the area enclosed by the eight points. The uncertainty of the vorticity calculations is 8%.

The circulation, Γ, around any closed path can be found from the velocity and vorticity fields. The circulation of the boundary layer formed on the canopy surface was estimated by integrating the velocity along a contour of constant vorticity. An example of the integration path used to calculate the circulation is shown in Fig. 2.11.

The impulse of the flow was calculated using a discrete form of Eq. 1.8. The region used in the integration was a rectangular area that enclosed all the vorticity in the plane to the right of the canopy centerline (*i.e.* $r \geq 0$). The edges of the integration region were located five vector grid points from the sides of the full vector field. A sample of the integration path is shown in Fig. 2.12.

The parachute canopy shed a series of vortex rings after it had fully inflated and achieved a steady state condition. In order to assess the shedding frequency of these vortices, the position of the vortex ring was tracked in each vorticity field. This results in a temporal evolution of the vortex position as well as the celerity of the vortex.

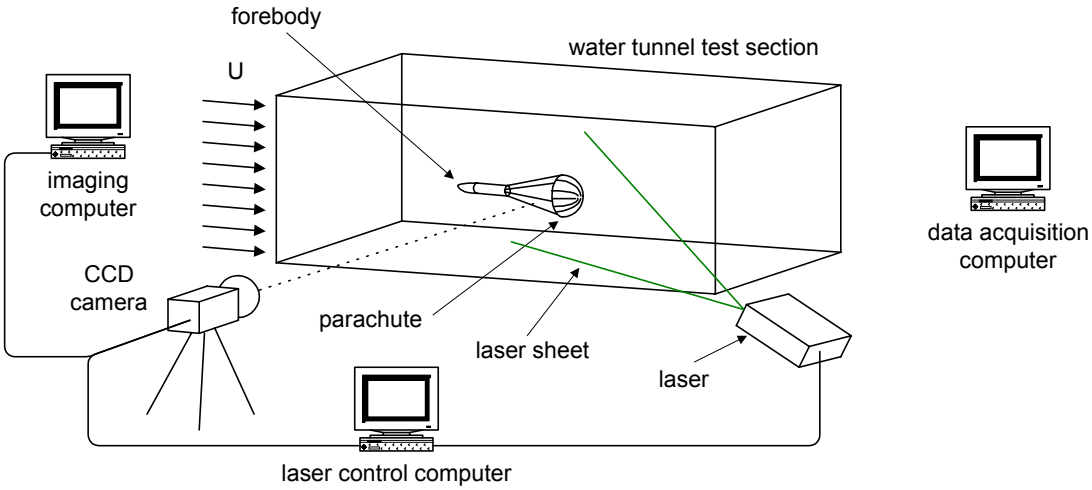

Figure 2.1. Schematic of experimental setup.

a) b)

Figure 2.2. Photographs of experimental setup, a) imaging computer, camera, and parachute model in water tunnel; b) data acquisition computer and lasers used in DPIV system.

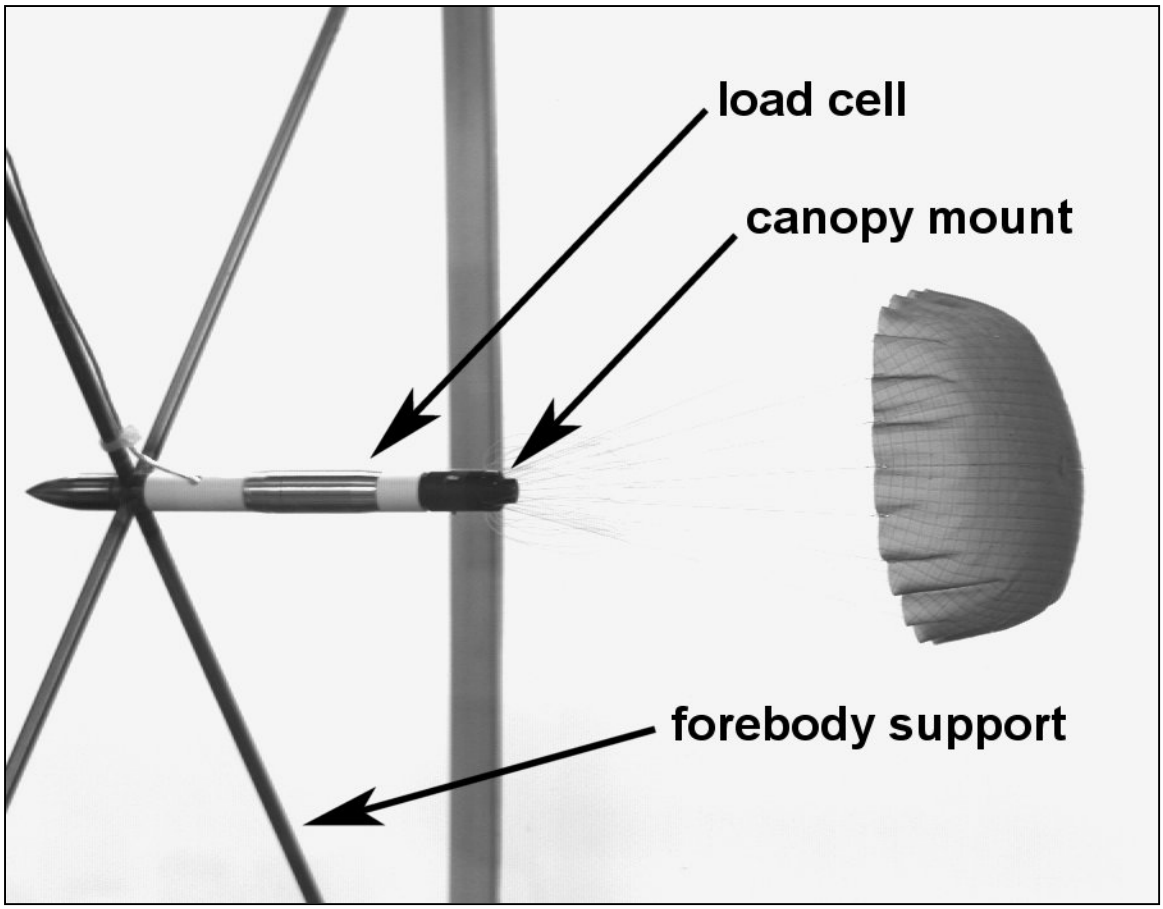

a)

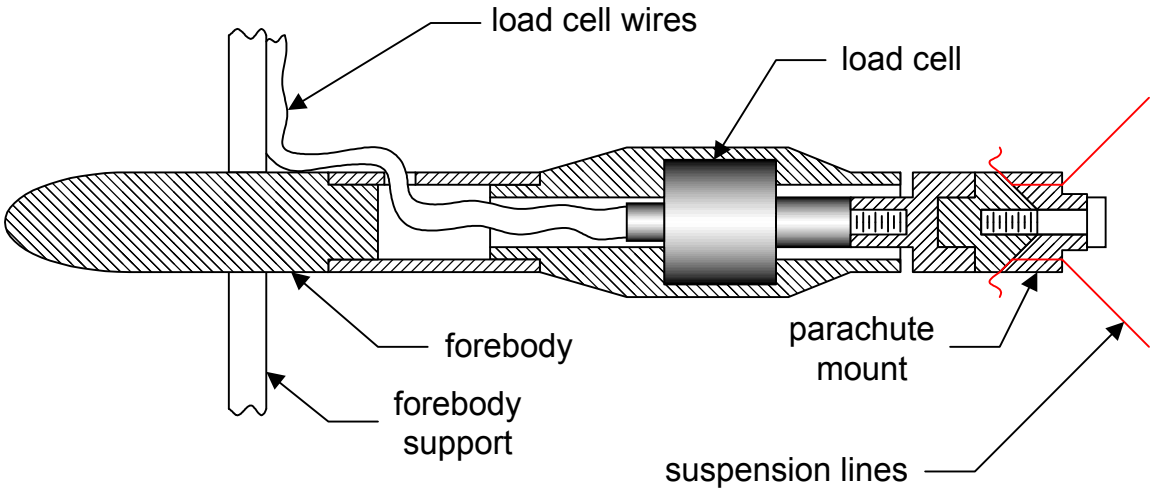

b)

Figure 2.3. Details of forebody, a) image of forebody and an inflated canopy; b) cross-sectional view of forebody, load cell, and parachute mount.

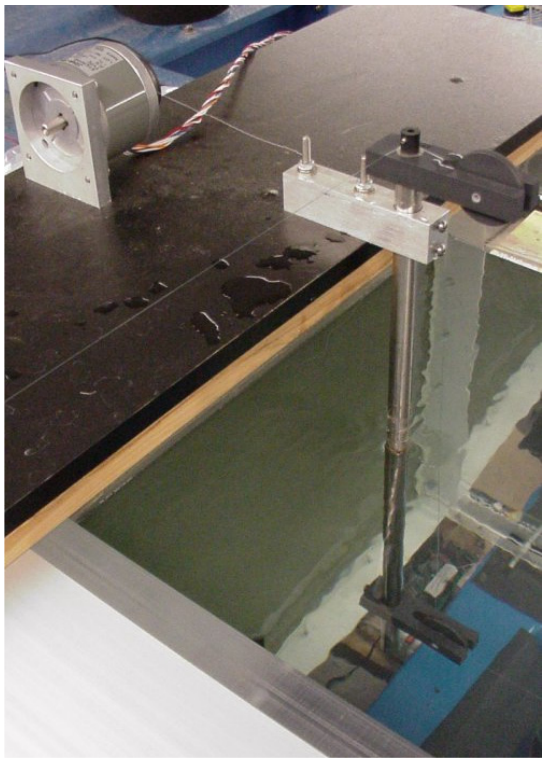

Figure 2.4. Image of deployment tube pulley system and stepper motor.

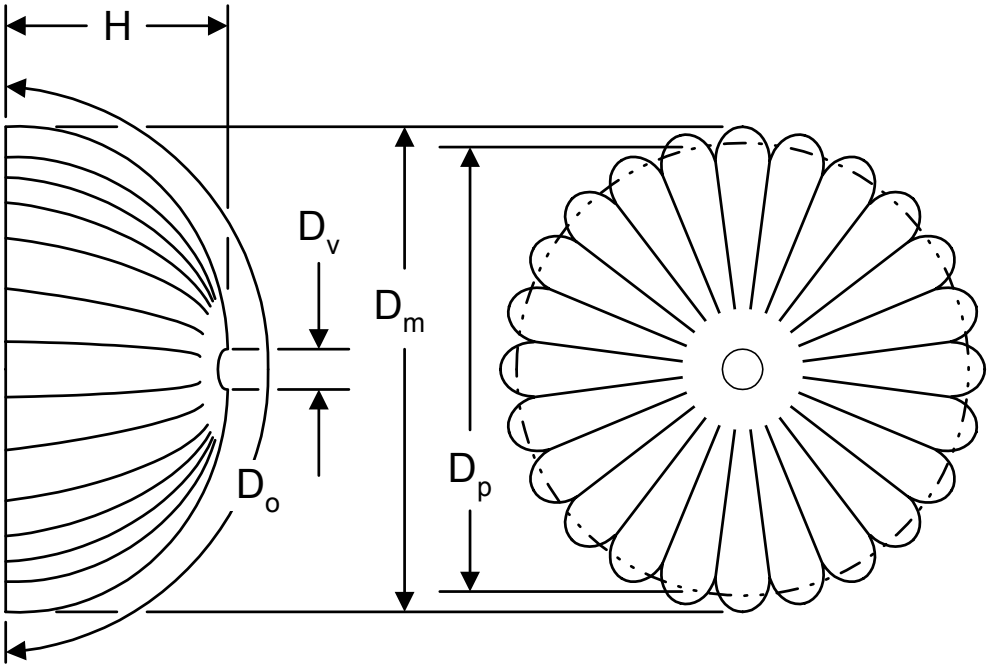

Figure 2.5. Schematic of parachute geometry and associated dimensions.

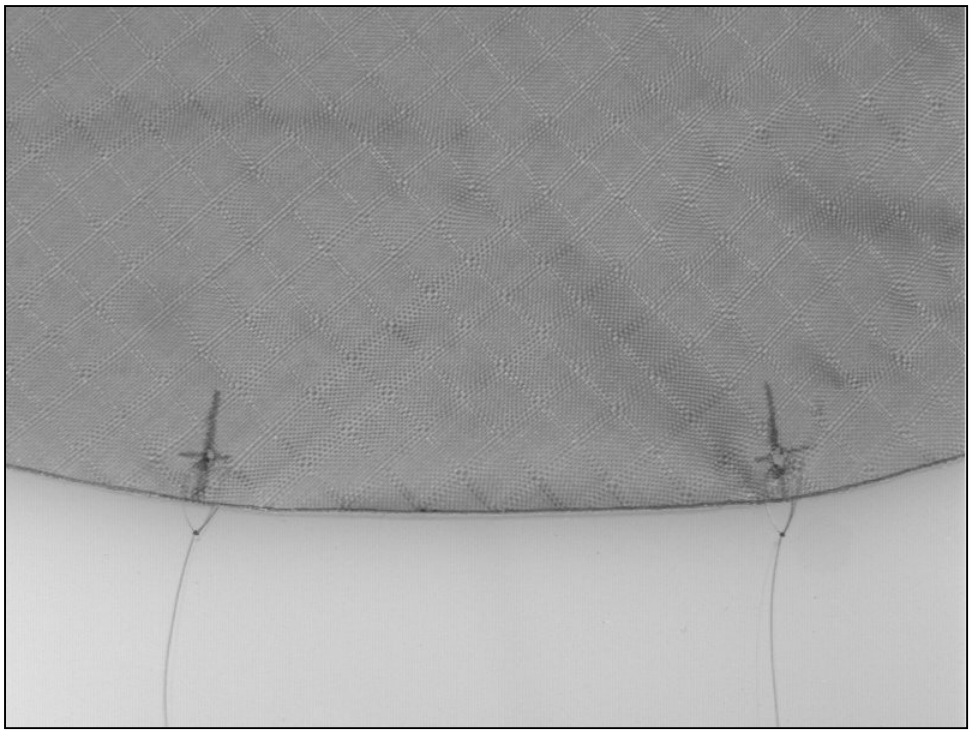

Figure 2.6. Image of the canopy edge and suspension line attachment.

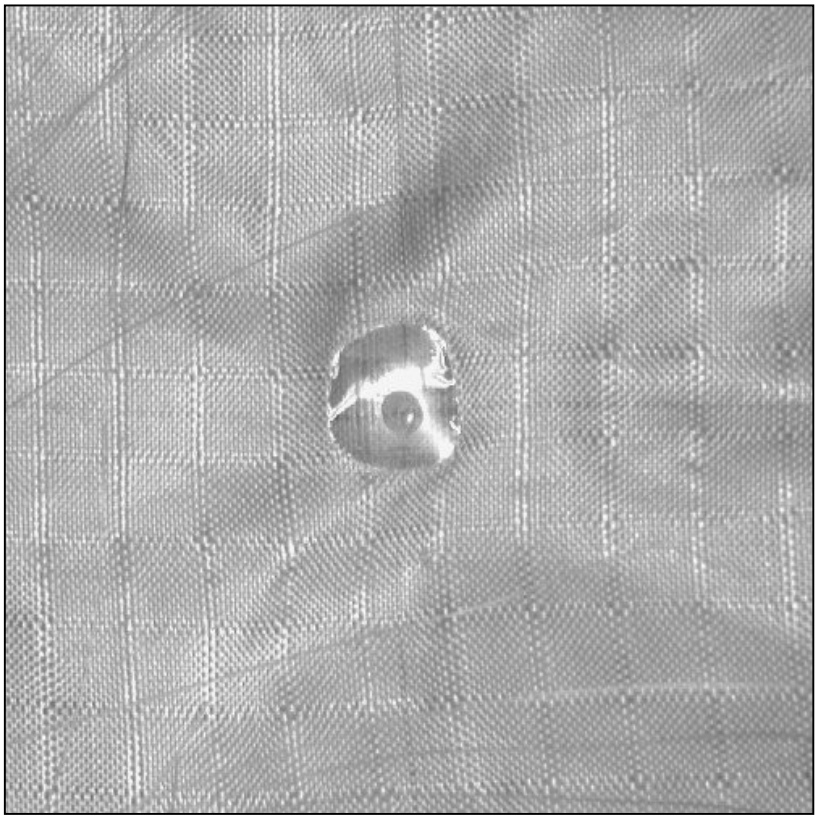

Figure 2.7. Close-up image of hard grommet at apex of canopy.

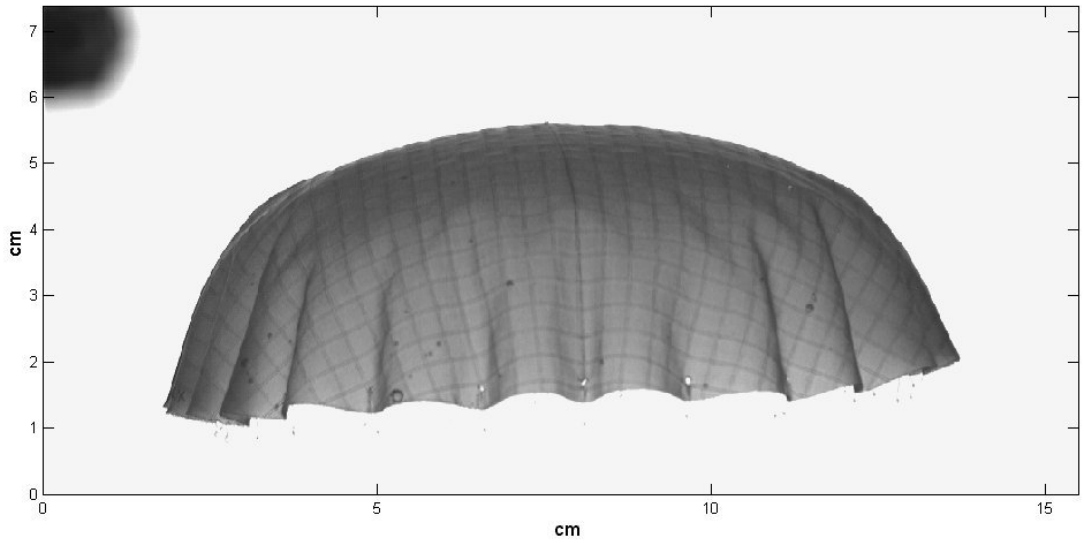

a)

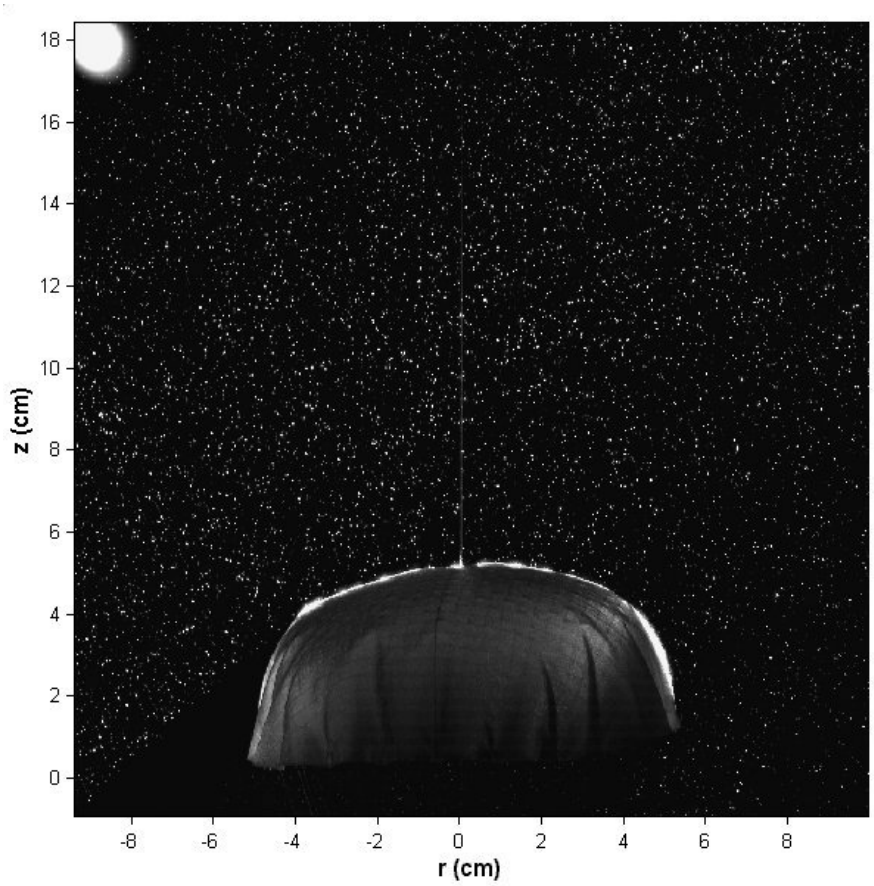

b)

Figure 2.8. Sample images from a) a geometry experiment and b) a velocity field experiment.

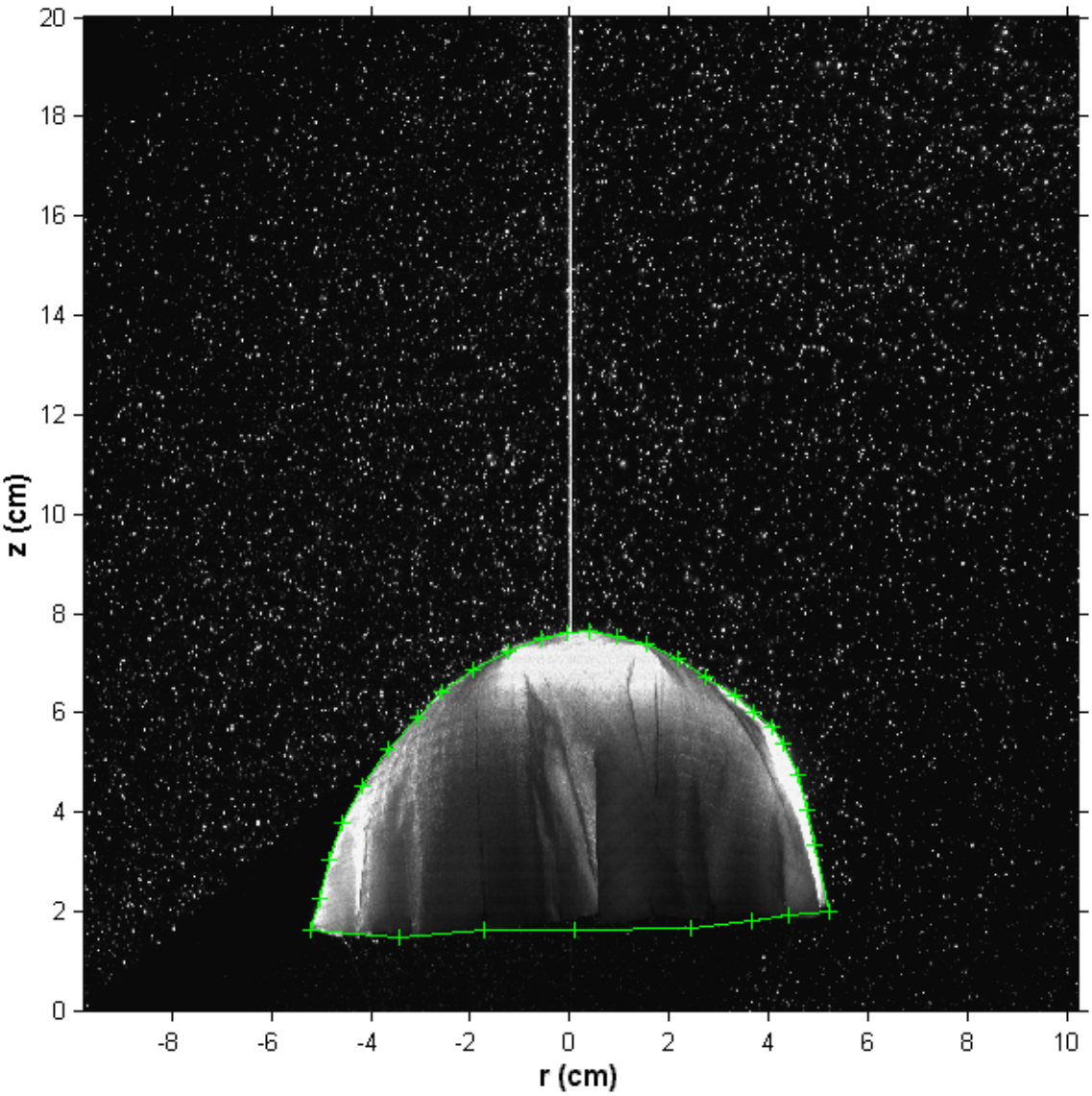

Figure 2.9. Sample image of canopy contour selected from original image.

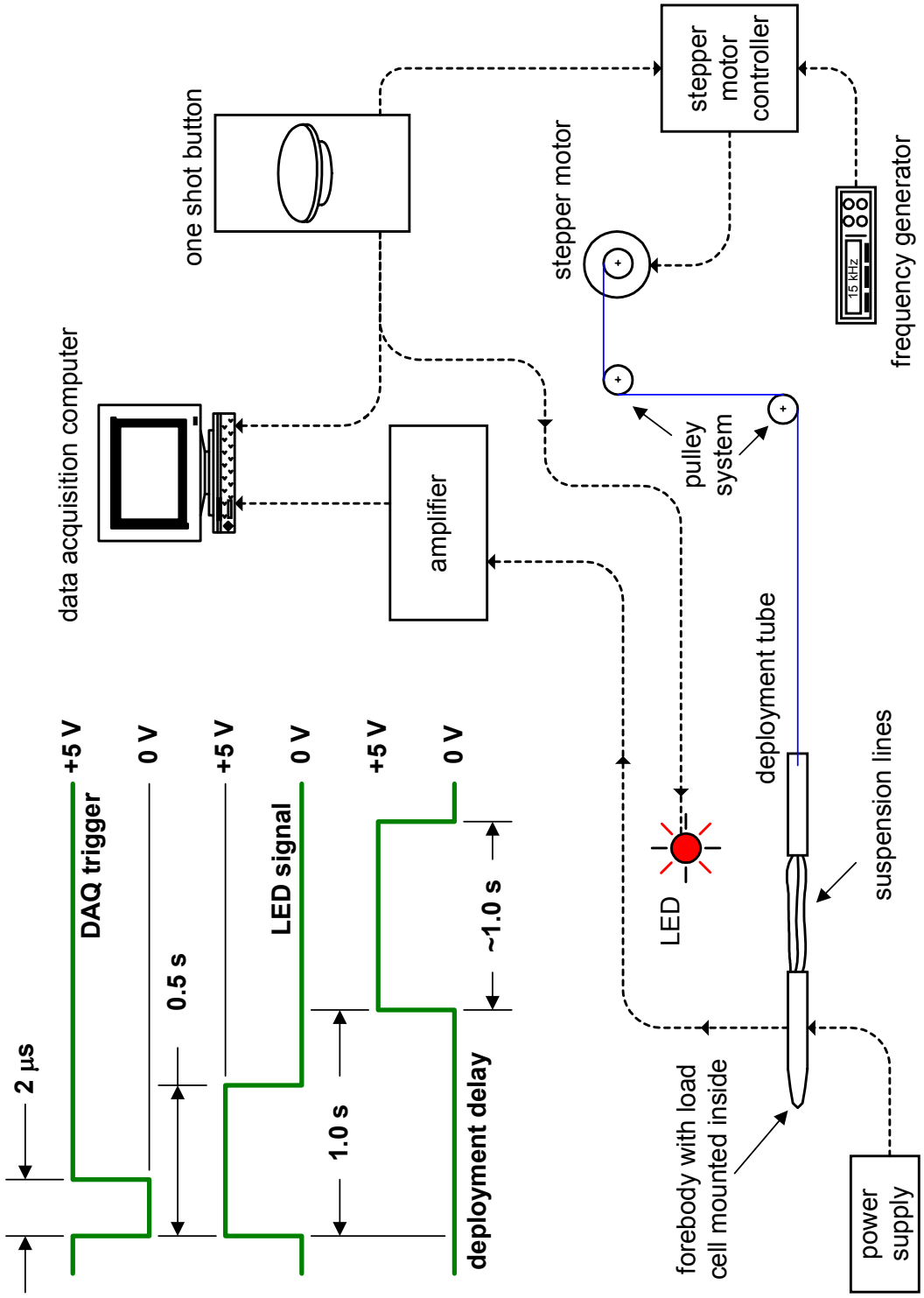

Figure 2.10. Schematic of the measurement synchronization system.

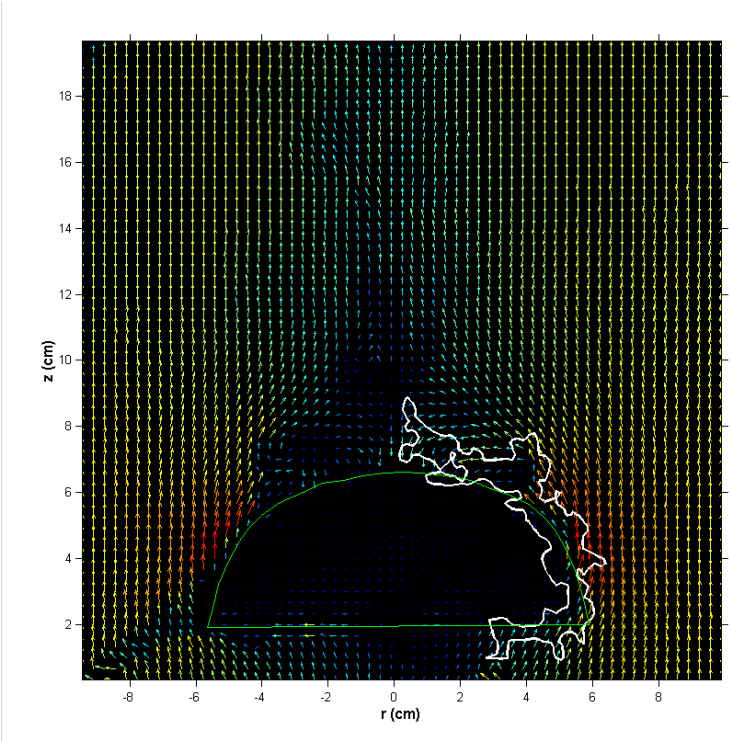

Figure 2.11. Sample contour along which circulation was calculated. The green line is a representation of the canopy edge.

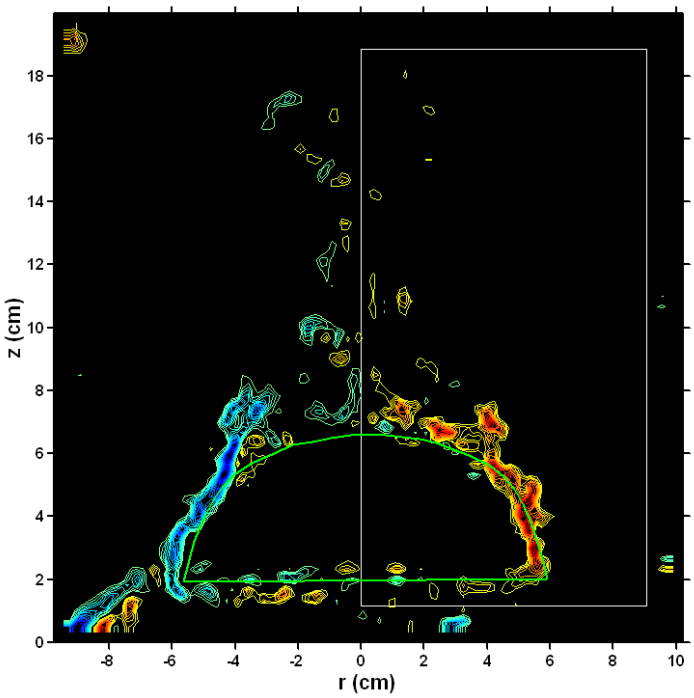

Figure 2.12. Sample region in which impulse was calculated from the vorticity field. The white line represents the enclosed region and the colored lines are vorticity contours.

3. Canopy in a Steady Flow

3.1 Mean Canopy Diameter

A canopy in steady flow (*i.e.* steady descent or steady state) exhibits a "breathing" phenomenon in which the diameter of the canopy grows and shrinks. This quasi-periodic motion of the canopy was observed for all canopy sizes examined and identified in measurements of the maximum projected diameter, D_m and the canopy force, F. This behavior is also observed in full-scale parachute canopies. A typical time history of the force and the maximum diameter from the experiments is shown in Fig. 3.1. The mean behavior of the canopy diameter and force will be examined initially.

Since the edge of the canopy is not a smooth surface but has a scalloped geometry (see Fig. 2.5), the mean projected diameter, D_p, was estimated by from the side-view of the images through

$$D_p \approx 0.935 \cdot D_m \tag{3.1}$$

at each Reynolds number. The projected diameter is the equivalent diameter of a circle with the same area. Defining the projected diameter in this manner allows for a direct comparison with fundamental wake studies of disks and spheres.

The mean projected diameter was calculated from the temporal measurements of the maximum diameter and is shown in Fig. 3.2 for the range of Reynolds numbers and canopy sizes studied. The mean projected diameter remained constant over this range of Reynolds numbers (Re_{Do} = 3.0-6.0 × 10^4) at $D_p/D_o \approx 0.71$. Full-scale, solid cloth canopies maintain mean projected diameters of $D_p/D_o \approx 0.67$-0.70 (Knacke, 1992), which shows good correspondence with our scale model results. The *rms*-value of the amplitude of the oscillation is D'_{rms}/D_p = 2.5-5.0%.

The automated image processing routines used to extract the canopy diameter also measured the mean canopy height, H. Normalizing the mean canopy height with the mean projected diameter shows that this ratio remains constant at $H / D_p \approx 0.41$ over the range of Reynolds numbers examined (see Fig. 3.2). A sense of how the height varies with the diameter can be ascertained by calculating the correlation coefficient, defined as (Taylor, 1997)

$$\rho_{x,y} \equiv \frac{\frac{1}{n}\sum_{i=1}^{n}\left(x_i - \mu_x\right)\left(y_i - \mu_y\right)}{\sigma_x \cdot \sigma_y} \qquad 3.2$$

where x and y represent the two variables to be correlated (in this case H and D_p), μ is the mean values of each variable, σ is the standard deviation of the variables, and the range of the correlation coefficient is $-1 \le \rho_{x,y} \le +1$. If $\rho_{x,y} = 0$, then the variables are uncorrelated while a correlation coefficient of +1 means they are perfectly correlated (*i.e.* when one variable increases the other variable also increases) and conversely, if $\rho_{x,y}$ = -1, the variables are perfectly anti-correlated (*i.e.* when one variable increases the other variable decreases). The correlation coefficient between the canopy diameter and height is shown in Fig. 3.3. The canopy height and diameter are negatively correlated, *i.e.* the canopy height shrinks while the diameter increases and vice versa. This behavior is expected since the stresses in the canopy fabric restrict the expansion of the canopy in each direction. The correlation of the diameter and height is reduced at higher Reynolds numbers. The correlation coefficient is reduced from –0.9 to –0.5 as the Reynolds number is increased from 3.0×10^4 to 6.0×10^4. Visual observations of the canopy indicate that an additional oscillation mode becomes apparent at the higher Reynolds

numbers. An asymmetric oscillation of the canopy fabric traverses from one side of the canopy to the other. It appears as a moving wave through the canopy fabric. This mode reduces the correlation between the diameter and height.

3.2 Mean Drag Force

The mean force experienced by the canopy model was calculated from the temporal measurements of the force provided by the load cell. A force coefficient, C_F, was defined as

$$C_F = \frac{F}{q_o S_o} \tag{3.3}$$

where q_o is the dynamic pressure (corrected for blockage effects in the water tunnel) and S_o is the constructed surface area of the canopy. The mean C_F values are plotted in Fig. 3.4 as a function of the Reynolds number. A Reynolds number dependence is clearly seen as well as a geometric dependence. The drag coefficient for full-scale canopies with similar geometries (flat circular canopies with low material permeability) is in the range of 0.75-0.8 but these canopies generally operate at Reynolds numbers two orders of magnitude larger than those seen in these experiments. The larger canopy (D_o = 30 cm) has a drag coefficient that is approximately equal to that seen in full scale canopies even at this lower value of the Reynolds number. However, the behavior of the larger canopy cannot be completely characterized based on measurements at a single Reynolds number. The discrepancy between the two canopies suggests that a transition might occur in the drag near this Reynolds number range.

Calculating the correlation coefficient between the diameter and the force shows the connection between the drag force and the reaction of the canopy geometry to it. The

correlation coefficient is plotted in Fig. 3.5. A mild anti-correlation (*i.e.* a negative correlation) exists between the force and the diameter at lower Reynolds numbers. This suggests that as the canopy diameter shrinks from its maximum value, the force is increasing. It will be shown in a later section that the periodic nature of the diameter and the force is caused by the shedding of a vortex from the canopy. Therefore, its suggested that the peak force in a single cycle may be related to the shedding of the vortex ring from the canopy. However, almost no correlation exists at the higher Reynolds number. At these higher Reynolds numbers, the shedding of the vortices becomes less organized resulting in a reduction of the correlation between the canopy diameter (which is closely related to the vortex shedding) and the force.

As discussed in Section 1.4, the force the canopy experiences from the fluid can be related to two primary sources, namely a force associated with the unsteady potential flow and a force associated with the vorticity containing portion of the wake. The unsteady potential force component will be examined first.

The unsteady potential flow comes about due to the oscillations of the canopy geometry (*i.e.* the diameter and height) and the associated changes in the enclosed fluid volume in the canopy. This is true as long as the canopy is not decelerating ($du/dt \rightarrow 0$). For the case of a fully inflated canopy, it is expected that the acceleration of the canopy would be small since the canopy is descending at a constant speed. Therefore, the potential flow force should only be a function of the enclosed volume. It was shown in Eq. 1.11 that the unsteady potential flow generates a force proportional to the rate of change of the canopy volume, *i.e.*

$$F_p = k_p \rho U_\infty \dot{V} \qquad 3.4$$

where k_p is a proportionality constant, ρ is the density of the fluid, and $\dot{V}$ is the time rate of change of the canopy volume. Since the volume of the canopy is cyclic in nature, the volume can be further decomposed into a mean volume, $\overline{V}$, and a fluctuating portion, V',

$$V = \overline{V} + V' \tag{3.5}$$

Due to the periodic nature of the geometry oscillations, the mean volume is a constant. Therefore, any force generated by this unsteady behavior comes strictly from the fluctuating portion of the volume; more specifically, the time derivative of the fluctuating volume. The time derivative of the volume fluctuations are both positive and negative in amplitude with a zero mean value. So in order to quantify the contribution that unsteady potential force has on the canopy dynamics, the *rms*-value of the time derivative of the volume fluctuations was calculated, $(\dot{V}')_{rms}$. Therefore, the force due to the unsteady potential flow was calculated as

$$(F_p)_{rms} = k_p \rho U_\infty (\dot{V}')_{rms} . \tag{3.6}$$

The volume of the canopy was estimated from the cross-sectional area and shape of the canopy in the images (see Section 2.3 and Appendix A for details of the image processing algorithm). The time derivative of the volume was calculated by using a central differencing scheme from which the *rms*-value of the fluctuations was determined. The unsteady potential force as a function of the Reynolds number is plotted in Fig. 3.6 assuming a value of unity for the proportionality constant in Eq. 3.6 (*i.e. kp* = 1). As is evident in Fig. 3.6, the unsteady potential flow amounts to only a small (~5-10%) fraction of the net mean force, $\overline{F}$. Additionally, the unsteady potential flow is responsible for a

larger portion (10-20%) of the measured force fluctuations, F'_{rms}. These results show that the majority of the force exerted on the canopy is caused by the viscous wake. The assumption generally made that the "added mass" term is the driving factor in the unsteady drag of the canopy has been shown to be inadequate. The contributions from the unsteady momentum deficit in the wake must be accounted for in any analysis.

The vortical force is produced due to the separation of the flow from the canopy and the formation of vorticity in the wake region which causes an adverse pressure gradient across the canopy. However, having no knowledge of the pressure field around the canopy, it was shown in Section 1.4 that the force associated with the wake was connected to the rate of change of the impulse of the flow. Namely, the axial force (*i.e.* the drag) can be calculated from the time derivative of azimuthal vorticity through the relationship in Eq. 1.9, which is repeated here

$$F_{\omega} = \frac{dI_z}{dt} = -\pi\rho \frac{d}{dt} \iint r^2 \omega_{\theta} dr dz \,. \qquad 3.7$$

The integration area used in these calculations was shown in Fig. 2.12. The viscous forces on the canopy, as in any bluff body, should be small in magnitude when compared to the drag forces produced by the pressure differential across the body.

A sample of the force calculated using Eq. 1.9 is shown in Fig. 3.7 where the horizontal line represents the mean vortical force. The highly fluctuating vortical force is the result of vorticity entering and leaving the control volume used in the calculation. The control volume has a finite size, namely, the region imaged in the experiments which imposes spatial limitations on the computation. Vorticity is being convected out of the control volume through its surfaces. The volume in which the vorticity integration occurs

should include all of the vorticity in the canopy wake, which suggests that the control volume would need to be nearly infinite in size. However, a finite integration area could be utilized provided that the vorticity that exits the volume has decayed to a sufficiently low level that it would be reasonable to ignore its contribution to the force. As is evident by the zero mean force in Fig. 3.7, this condition does not apply to the vorticity fields measured in the canopy wake which shows that the integration region used was too small for these calculations.

Additionally, utilization of Eq. 1.9 requires detailed knowledge of the vorticity in the integration area. The primary source of vorticity in the wake comes from the shear layers originating at the canopy skirt. However, the thickness of the shear layers is on the order of the spacing between the velocity vectors (a few millimeters) measured in the experiments which are used to calculate the vorticity. This situation would result in an under-estimation of the vorticity which in turn would tend to under-predict the axial impulse and the resulting force.

3.3 Canopy Dynamic Behavior

The mean behavior of the canopy now having been established, the unsteady characteristics (*i.e.* the breathing) of the canopy behavior will be examined. The breathing of the canopy is due to the flow field in the near wake of the canopy provided that canopy is flexible enough to respond to the flow (*i.e.* the canopy is non-rigid). The velocity and vorticity fields show that the breathing corresponds with the shedding of vortical structures from the canopy. Figure 3.8 shows the vorticity field in the canopy wake over one shedding cycle. It is clear that the flow is separated at the canopy skirt.

When the canopy reaches its minimum diameter (Fig. 3.8a), a distorted vortex ring is seen to have just shed from the canopy. This vortex is conveyed downstream into the turbulent wake. In the wake it becomes even more disorganized and distorted as the vortex decays. At the canopy skirt, a shear layer rolls-up into another vortex ring over the next few image sequences (Fig. 3.8b-d). While this vortex ring is forming, the canopy diameter also increases until the canopy reaches its maximum diameter (Fig. 3.8d). The process of forming the vortex generates a low pressure region near the canopy skirt which draws the canopy out to its maximum diameter. With the new vortex ring formed, the shear layer from the canopy skirt feeds the vortex with additional vorticity until the vortex separates from the shear layer and canopy and is convected downstream (Fig. 3.8e-f). The convection of the vortex ring also removes the low pressure region at the canopy skirt and moves it farther downstream of the canopy which results in the canopy diameter shrinking back to its minimum diameter (Fig. 3.8f).

A phased average vorticity field was calculated from the primary shedding frequency of the canopy (the shedding frequency is established in the next section). A sample of the phase averaging is shown in Fig. 3.9 for a 15 cm canopy at a freestream velocity of 20 cm/s. It is clear from these images that a vortical structure is seen to shed from the canopy and is conveyed downstream with the shedding cycle repeating at a frequency of 1 Hz. A qualitative verification of the shedding frequency can be made by observing that vortex ring is located in the same downstream position in both Figs. 3.9a and 3.9h which have a time separation of 1 s.

A parachute canopy in steady flow also exhibits behavior in some aspects analogous to those traditionally seen with rigid bluff bodies (such as disks or spheres).

The time-averaged velocity and vorticity field in the wake of the canopy, averaged over a 1000 (~67 s) instantaneous measurements of the fields (Fig. 3.10), shows a momentum deficit exists in the wake which is characteristic of turbulent three-dimensional wakes of axisymmetric bluff bodies. The profile of the axial velocity, u_z, and the radial velocity, u_r, at three different downstream locations is shown in Fig. 3.11a and the vorticity is shown in Fig. 3.11b. The variation of the time-averaged axial velocity across the wake of the canopy is clearly seen, with some back flow along the centerline of the wake. This velocity profile results in a momentum deficit in the wake which contributes to the drag of the canopy. The radial velocity indicates entrainment of the freestream velocity in the shear layers into the wake region from both sides of the canopy at the two farthest downstream locations. The majority of the vorticity is confined to the shear layers near the canopy skirt and decays rapidly at farther downstream distances. These characteristics are seen in rigid bluff bodies, however, the flexible nature of the canopy introduces some unique behavior not seen in rigid bluff bodies.

3.4 Breathing Frequency

The periodic nature of the canopy motions (see Fig. 3.1) suggests that a spectral analysis of the data would allow for the identification of the dominant breathing frequencies. The spectral content of the data was uncovered by the application of the Fast Fourier Transform (FFT). The plots in Fig. 3.12 show the maximum canopy diameter and the frequency content of the diameter measurement for a 15 cm canopy at a freestream velocity of 30 cm/s. The spectrum shows a single dominant frequency at

f = 1.5 Hz. We define a non-dimensional breathing frequency based on the mean projected diameter and the freestream velocity as

$$\frac{f \cdot D_p}{U_\infty}. \tag{3.8}$$

Observations of the spectrum for all the different canopies and range of freestream velocities, show that a single dominant frequency exists. The non-dimensional frequency remains very nearly constant at a value of 0.56 ± 0.03 across the Reynolds numbers and geometries examined (see Fig. 3.13). This is the dominant canopy breathing frequency described in section 3.3. The breathing (or the aeroelasticitic response) of the canopy is contingent upon the canopy material being flexible enough to respond to the flow field. If the canopy was rigid, then the shedding characteristics would be probably different and the canopy breathing would not occur. The canopy breathing results in the flow separation point (*i.e.* the canopy skirt) moving in the flow field.

The spectral analysis of the force measurements made with the load cell generates a complex spectrum (as shown in Fig. 3.14). However, a frequency corresponding to the dominant frequency observed in the diameter measurements was also seen in the frequency spectrum of the force (Fig. 3.15). Non-dimensionalizing this frequency also results in a 0.56 ± 0.03 value. As will be shown below, this frequency corresponds to the periodic shedding of vortices at the edge of the canopy skirt.

The DPIV measurements create an array of regularly spaced velocity vectors throughout the flow field. By extracting or "probing" these measured velocity vectors at various points in the wake, a means for relating the fluid mechanics of the canopy wake to the canopy geometry and force can be established. Table 3.1 lists the probe locations

utilized in the velocity fields. At these points, the radial velocity, u_r, was extracted. A sample of the radial velocity at points **A** for the 15.2 cm canopy is shown in Fig. 3.16.

Table 3.1. Velocity probe locations.

D_o (cm)	Location	r/D_p	z/D_p
15.2	**A**	±0.69	0.25
15.2	**B**	±0.81	1.0
15.2	**C**	0.81	1.59
30.5	**A**	0.69	0.25
30.5	**B**	0.97	0.97

The large fluctuation in the radial velocities appear to be quasi-periodic. A sample of the spectral analysis of the radial velocities is shown in Fig. 3.17. By defining a Strouhal number as,

$$St \equiv \frac{f \cdot D_p}{U_\infty} \tag{3.9}$$

a dominant frequency at $St = 0.54 \pm 0.04$ occurs across the range of Reynolds numbers examined, Fig. 3.18. However, another frequency seems to appear around a Strouhal number of 0.3 – 0.4 at points further downstream of the canopy (Figs 3.17b-c). Neither of these frequencies have been observed in the past studies of disks or spheres (Balligand & Higuchi, 1993; Berger *et al.*, 1990; Fuchs *et al.*, 1979). Three dominant frequencies are classically associated with a stationary disk. The primary frequency is associated with a helical mode for the vortex structure. This mode has a Strouhal number of 0.134 but has been observed beyond ~3-4 diameters downstream (Berger *et al.*, 1990). Our studies focused on a region 1.5 diameters downstream but we see evidence that this mode started to form in our experiments (Fig. 3.17c) at the farthest downstream locations. Another mode of the disk has a Strouhal number of 0.05 which corresponds to the axisymmetric

oscillation of the recirculation region immediately behind the disk. We see no evidence of this from our velocity probe data. And finally, a high frequency shear layer instability was also seen in the disk studies of Berger *et al.* (1990) at $St = 1.62$. Again, we did not find any evidence of these structures. This is possibly due to the spatial resolution of our velocity field being too small.

A qualitative observation of the vortex formation in the PIV data fields shows that vortex rings form symmetrically around the canopy at lower Reynolds numbers. Once the vortex is shed from the canopy and is conveyed downstream, the symmetry of the vortex begins to degrade. The vortex ring becomes twisted and disorganized in the wake of the canopy. The initial symmetry can be quantified by analyzing the radial velocity of the wake flow in the immediate vicinity of the canopy and at positions farther downstream. Calculating the correlation coefficient, between the two symmetric probe points listed in Table 3.1 quantifies the symmetry of the vortex. The results of the correlation coefficient calculations (Fig. 3.19) suggests that the vortex is initially symmetric immediately downstream of the canopy (*i.e.* points **A**) at the lower Reynolds number. As the vortex is conveyed farther downstream (*i.e.* points **B**), the correlation coefficient is reduced indicating that the vortex is becoming disorganized. This behavior confirms our qualitative observations of the wake behavior. At a Reynolds number of 6.0×10^4, the behavior of the vortex is different. Qualitative observations of the vortex shedding, shows that the vortex formation occurs symmetrically but once shed from the canopy, the vortex quickly becomes distorted. This is reflected in the fact that almost no correlation exists between the symmetric probe points at either location.

The vortex core location was measured in the vorticity field by locating the center of the vortex. The position of a series of shed vortex rings is plotted in Fig. 3.20. The position of the vortex ring was measured separately on each side of the canopy. The vortex ring is confined to a region on the outer extreme of the canopy initially at which point the vortex ring diameter slightly grows and becomes more disorganized as the vortex ring moves farther downstream. The growth is evident by the increase in the width of the mean vortex position at the locations further downstream. And the disorganization is apparent by observing the increased scatter of the vortex position again at the locations farther downstream.

A sample of the axial vortex position is shown in Fig. 3.21. The plot shows the periodic shedding of a vortex. A saw tooth pattern in the vortex downstream position is seen. This comes about since an individual vortex was only tracked until a new vortex formed near the canopy skirt at which point the new vortex was tracked. The linear portion of the saw tooth pattern shows that the vortex is conveyed downstream at a nearly constant celerity. The celerity of the vortex was calculated from the average slope of the linear portions of the position plot. The average celerity utilized the slope calculated from both sides of the canopy and from all shedding cycles. The celerity of the vortex rings (normalized by the freestream velocity) over the range of Reynolds numbers examined is plotted in Fig. 3.22 where the error bars represent the standard deviation of the measurements. The normalized celerity remains constant at a value of $u_c/U_\infty = 0.41 \pm 0.02$ across the range of geometries and Reynolds numbers studied.

A spectral analysis of the vortex downstream position was performed and a sample of that analysis is shown in Fig. 3.23. Again a dominant frequency was identified

that corresponded to the vortex shedding frequency. The Strouhal number from this analysis is plotted in Fig. 3.24 with a mean value of $St = 0.54 \pm 0.04$ which corresponds very well with our previous results. Calculating the correlation coefficient between the vortex location on the right and left sides of the canopy shows how symmetric the vortex is shed from the canopy. The correlation coefficient is plotted in Fig. 3.25. The vortex is initially shed symmetrically from the canopy at the lower Reynolds number but as the Reynolds number increases the symmetry of the shedding vortex decreases. This behavior was also seen in the velocity probe measurements shown in Fig. 3.19.

In conclusion, it has been shown that the breathing phenomena a canopy experiences while in steady descent is associated with vortex shedding. The shedding frequency corresponds to a Strouhal number of $St = 0.54 \pm 0.04$ while the non-dimensional breathing frequency of the canopy is 0.56 ± 0.03. Also, it was shown that the unsteady potential flow, as identified by the apparent mass is inadequate for predicting the fluctuating forces. The unsteady wake effects should be included in any model used to predict canopy performance and characteristics.

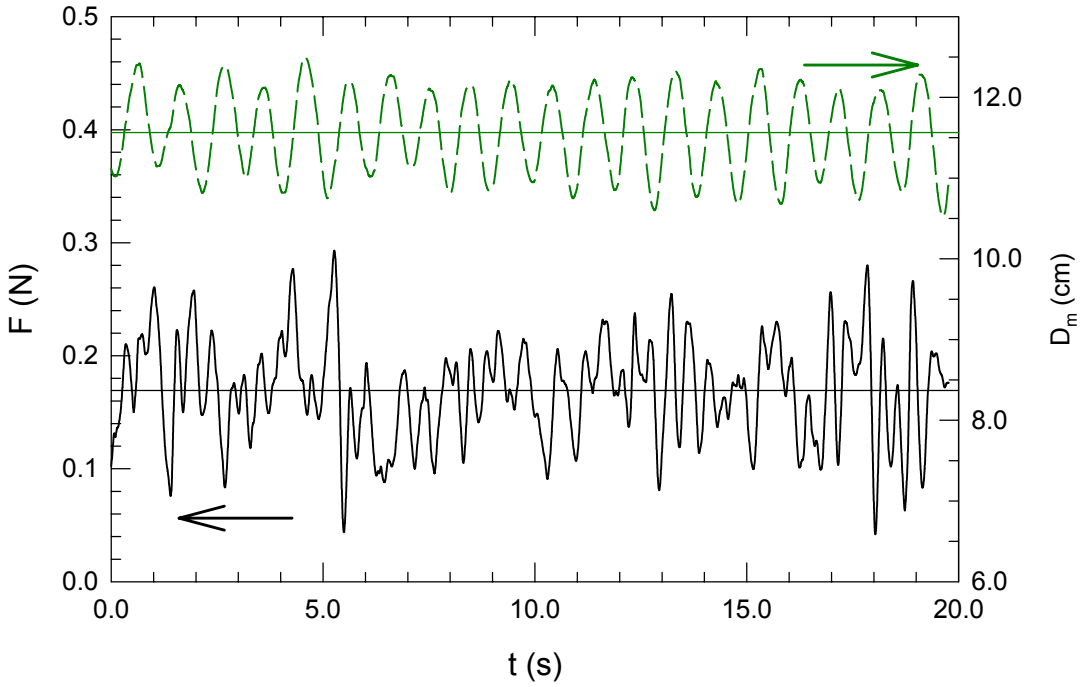

Figure 3.1. Maximum diameter and force measurements for a D_o = 15.2 cm canopy with U_∞ = 20 cm/s.

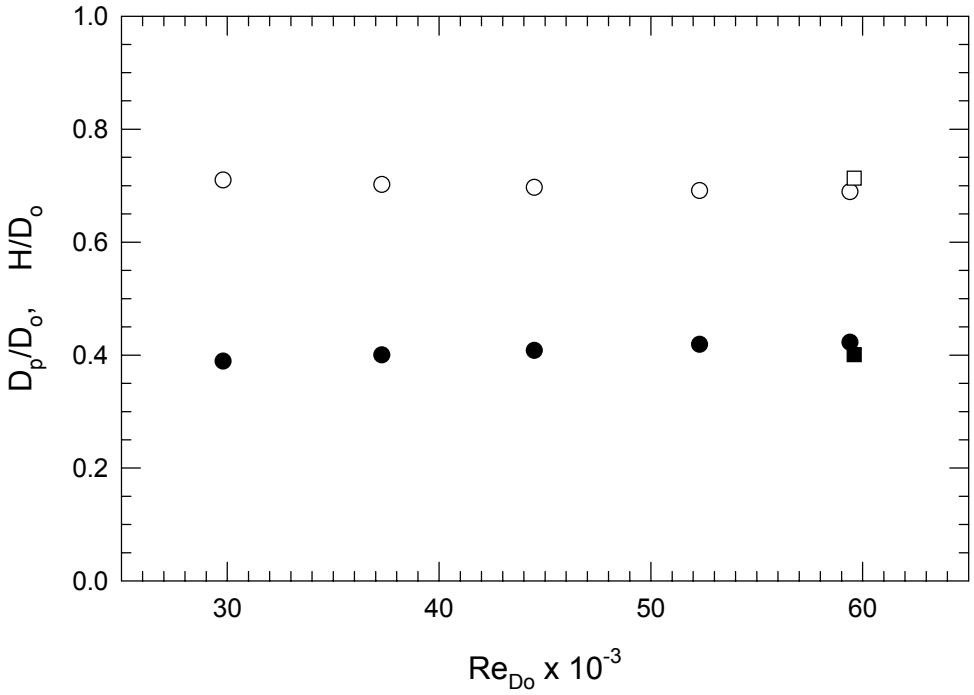

Figure 3.2. Normalized mean canopy projected diameter (hollow symbols) and mean canopy height (solid symbols). The round symbols represent the 15 cm canopy and the square symbol represents the 30 cm canopy.

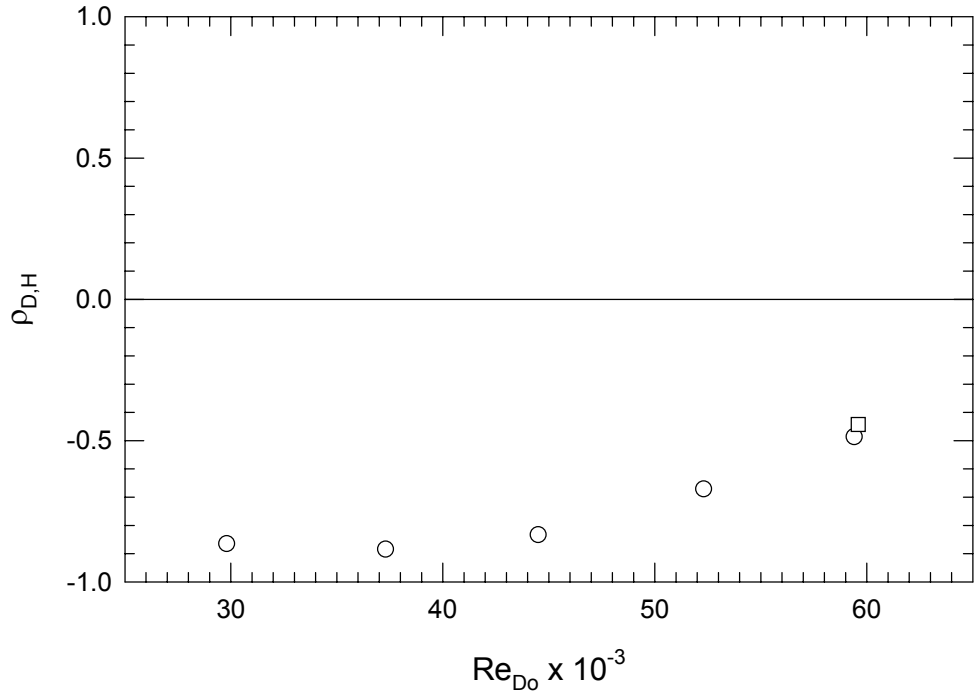

Figure 3.3. Correlation coefficient between the canopy diameter and height. The round symbols represent the 15 cm canopy and the square symbol represents the 30 cm canopy.

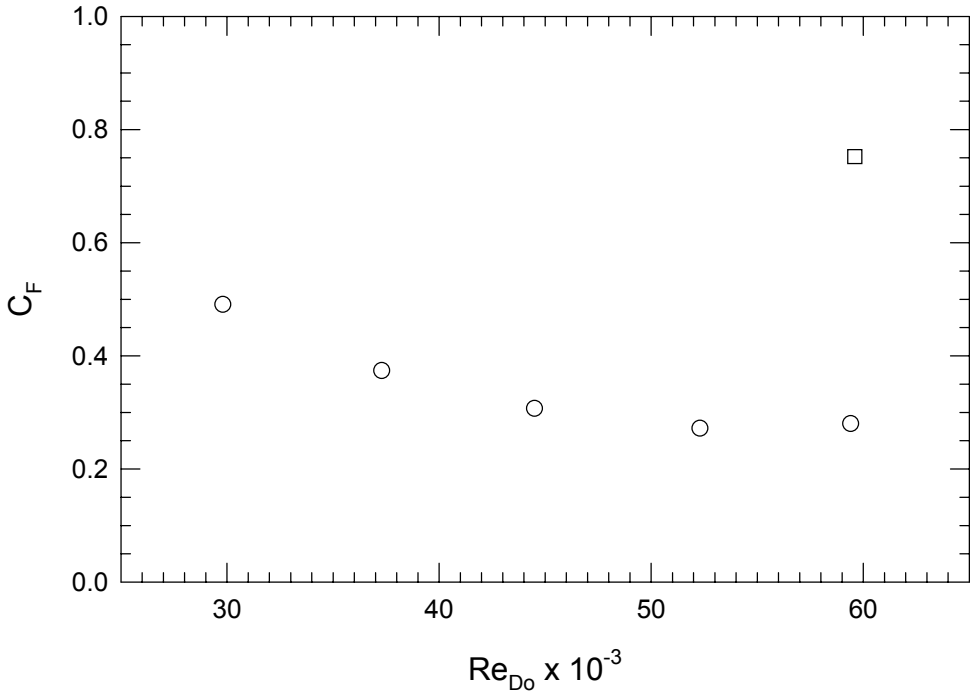

Figure 3.4. Force coefficient for canopy. The round symbols represent the 15 cm canopy and the square symbol represents the 30 cm canopy.

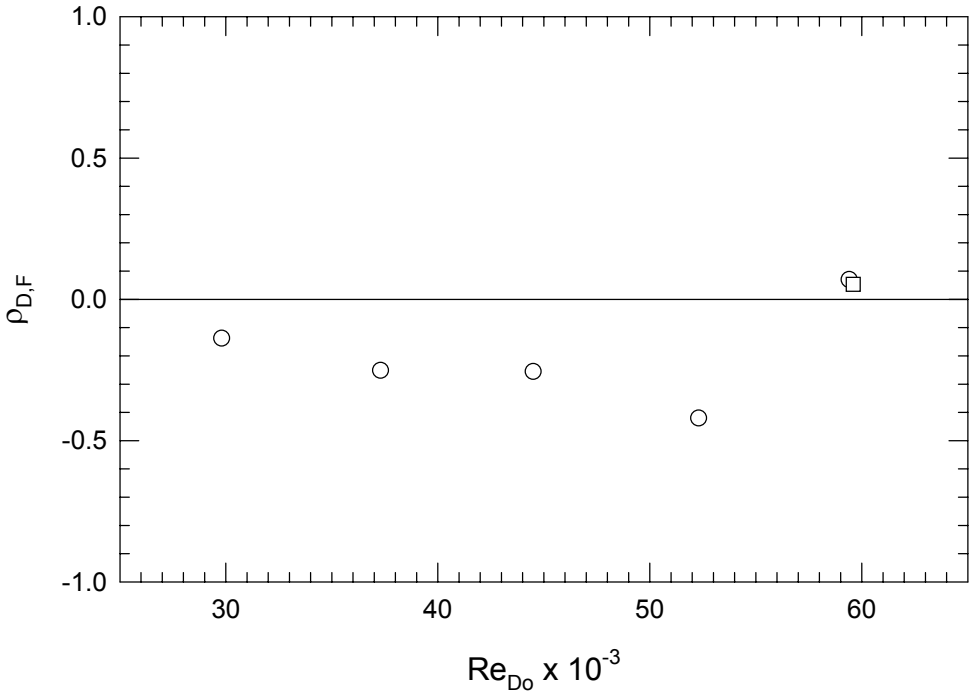

Figure 3.5. Correlation coefficient between the canopy diameter and force. The round symbols represent the 15 cm canopy and the square symbol represents the 30 cm canopy.

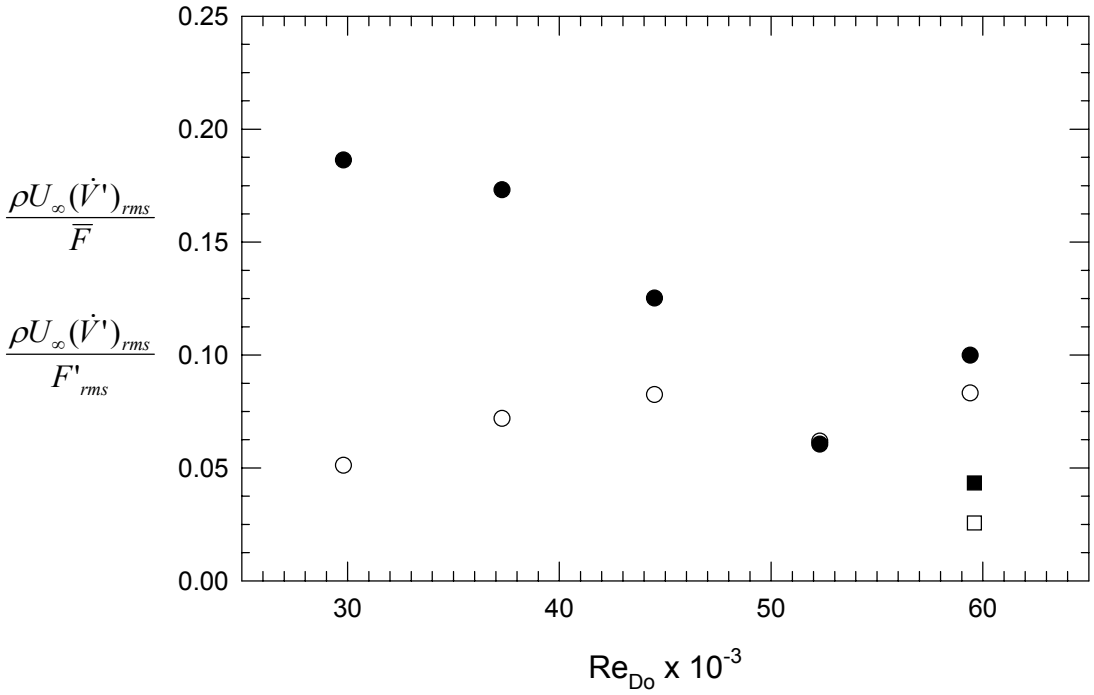

Figure 3.6. Force associated with the unsteady potential flow; $(F_p)_{rms}/\overline{F}$ (hollow symbols); $(F_p)_{rms}/F'_{rms}$ (solid symbols). The round symbols represent the 15 cm canopy and the square symbol represents the 30 cm canopy.

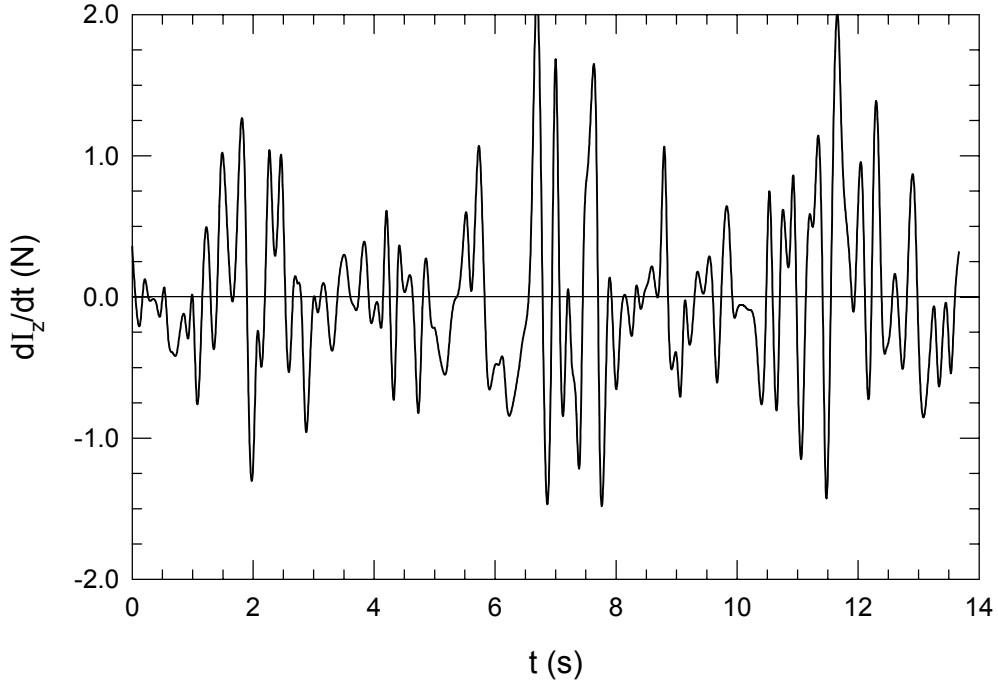

Figure 3.7. A sample of the force caused by the vorticity in the wake for a 15 cm canopy at a freestream velocity of 20 cm/s.

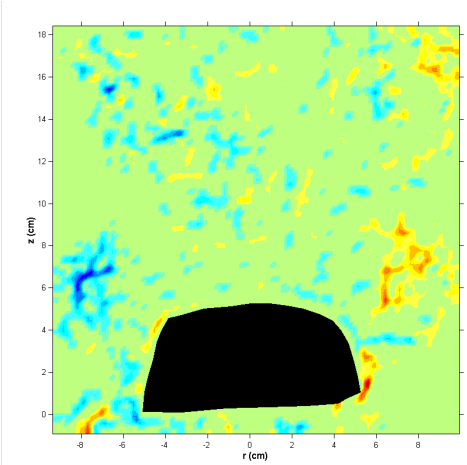

a) t = 0 ms (minimum canopy diameter)

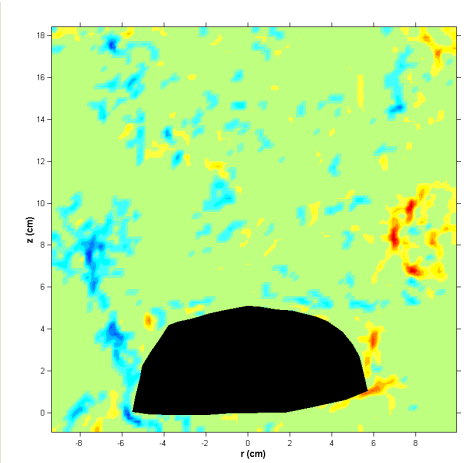

b) t = 200 ms

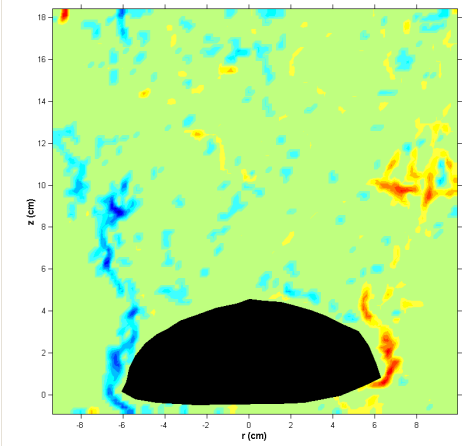

c) t = 400 ms

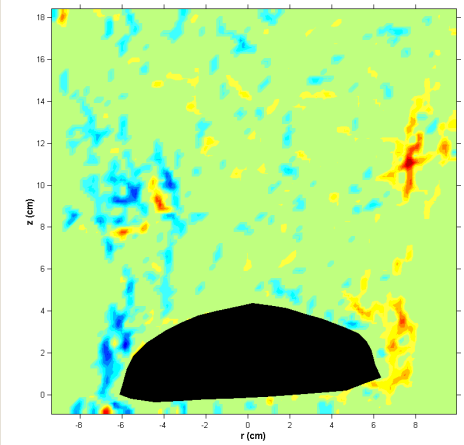

d) t = 533 ms (maximum canopy diameter)

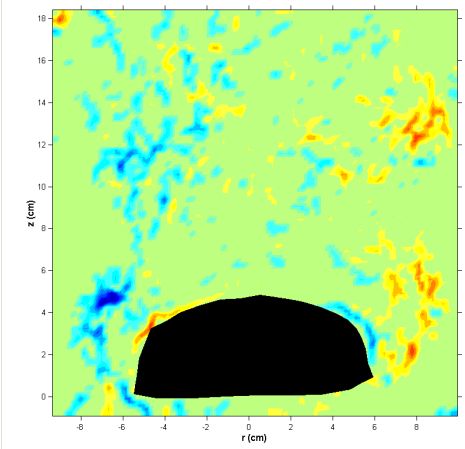

e) t = 800 ms

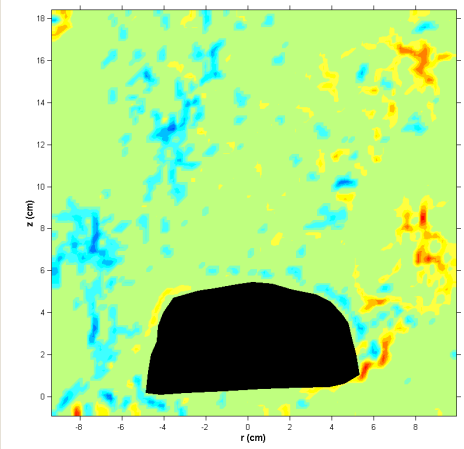

f) t = 1067 ms (minimum canopy diameter)

Figure 3.8. Vorticity field showing vortex formation during canopy breathing (image of canopy has been superimposed over the vorticity field).

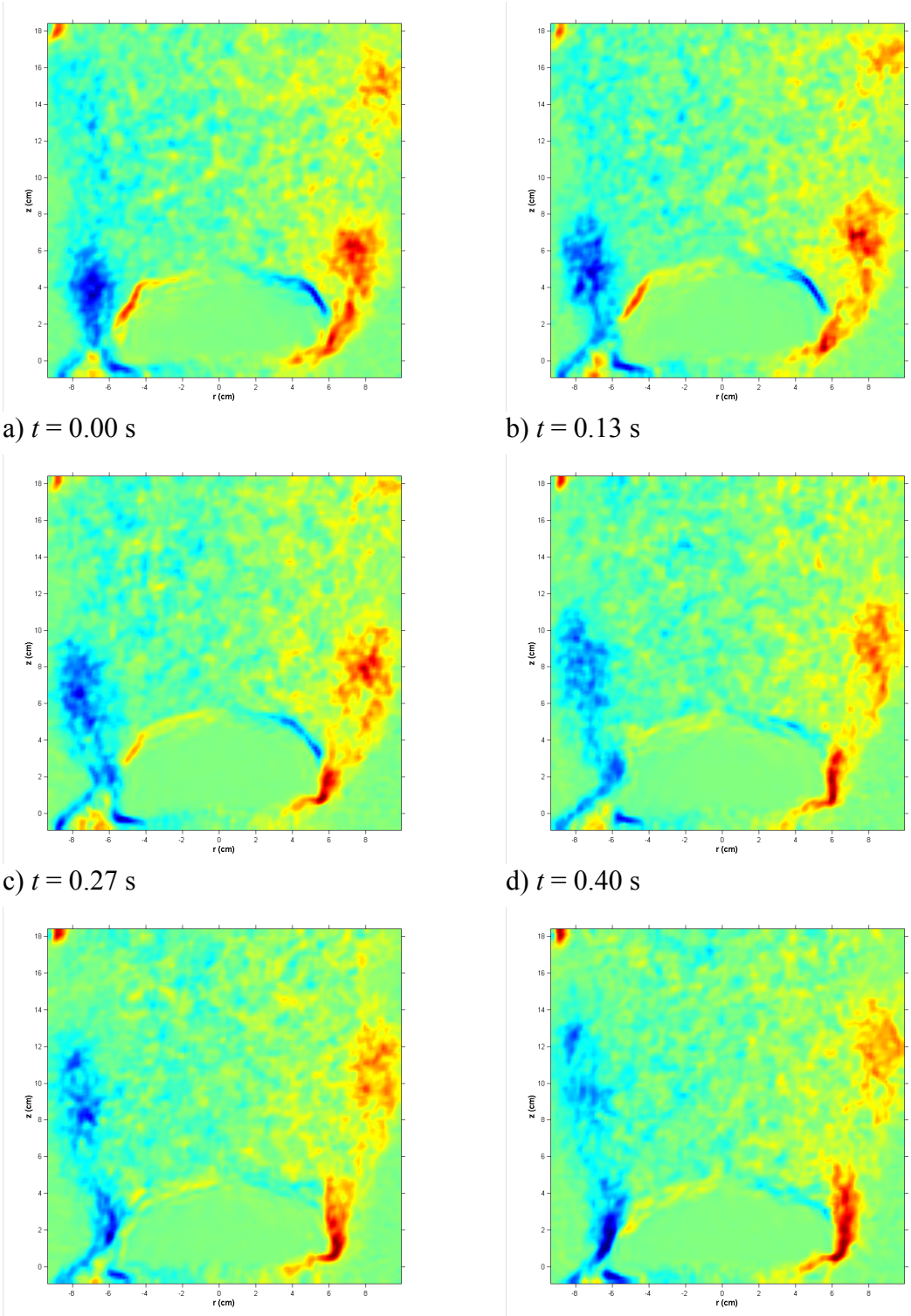

a) $t = 0.00$ s b) $t = 0.13$ s

c) $t = 0.27$ s d) $t = 0.40$ s

e) $t = 0.53$ s f) $t = 0.67$ s

Figure 3.9. Phased average vorticity field for a 15 cm canopy at a freestream velocity of 20 cm/s. The average field was calculated from 14 instantaneous field measurements.

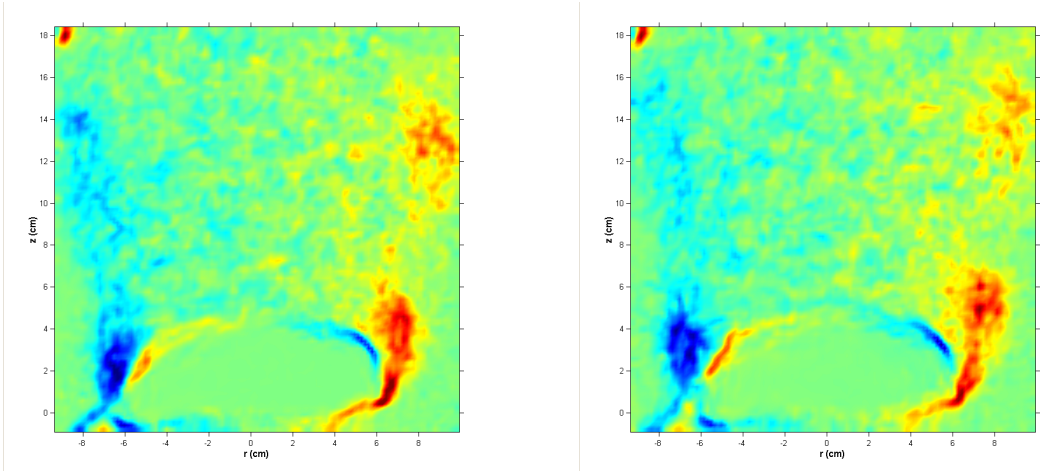

g) $t = 0.80$ s h) $t = 0.93$ s

Figure 3.9. continued.

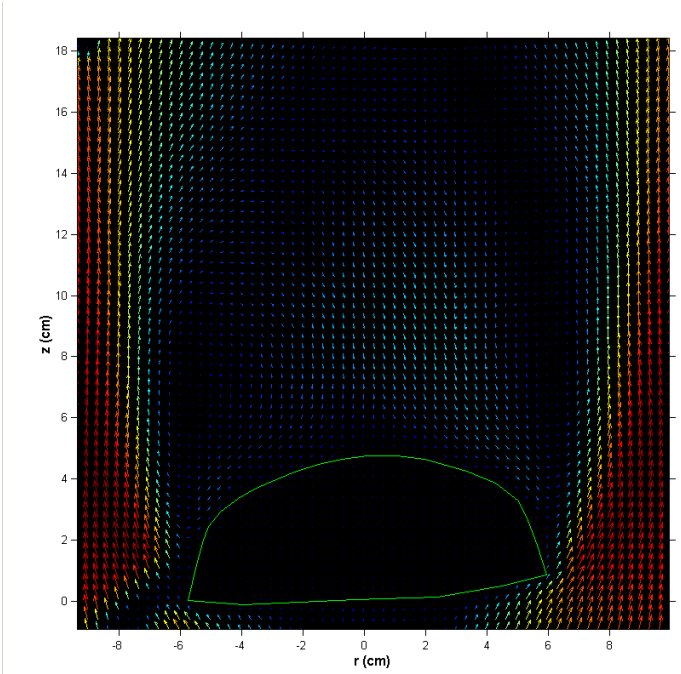

a)

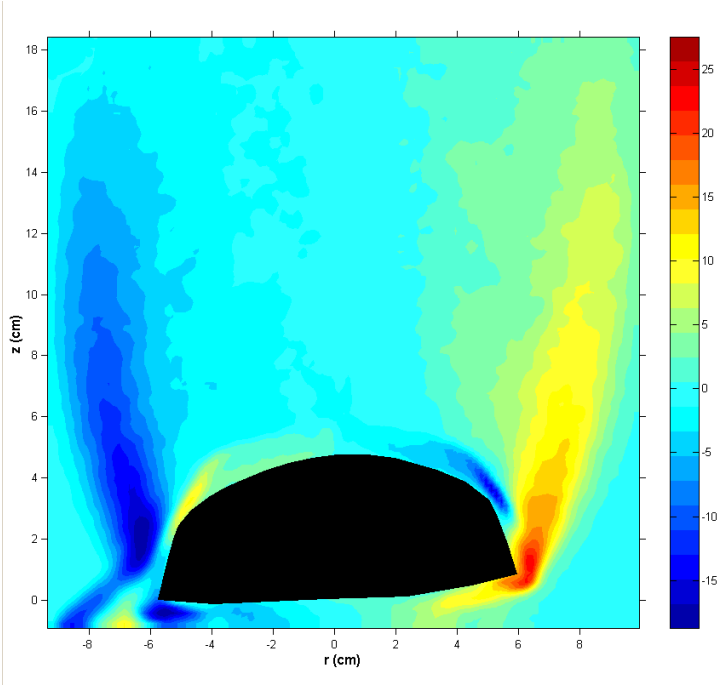

b)

Figure 3.10. a) Mean velocity field and b) mean vorticity field in the wake of a canopy in a steady flow, D_o = 15.2 cm and $Re_{Do} = 3.0 \times 10^4$. An image of the canopy at its mean diameter has been super-imposed over the velocity field.

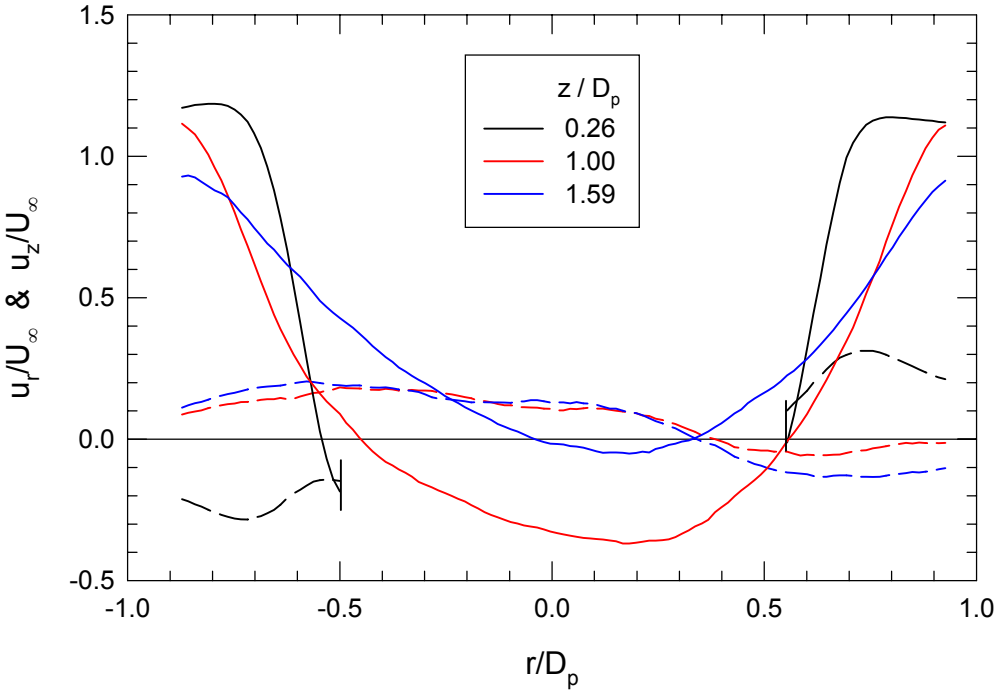

a)

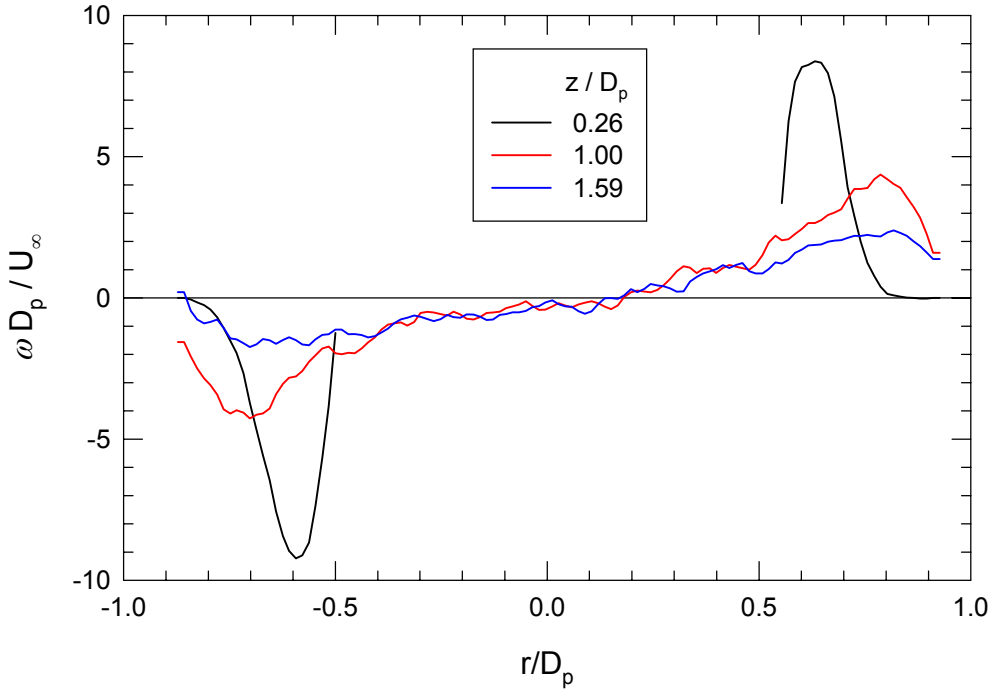

b)

Figure 3.11. a) Mean axial (solid lines) and radial (dotted lines) velocity profiles and b) mean vorticity profiles at three downstream locations.

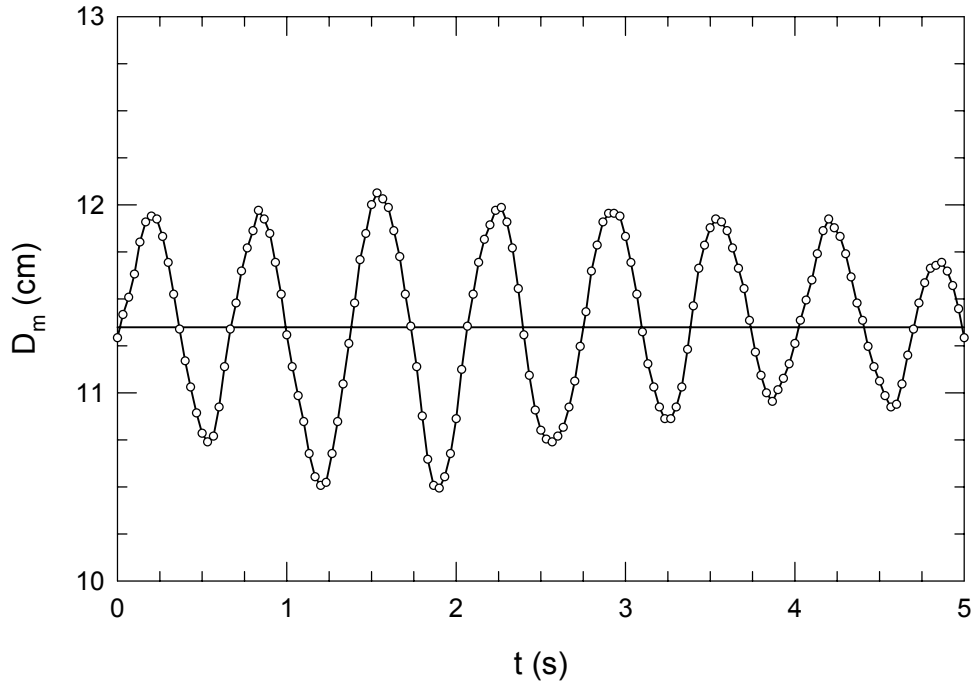

a)

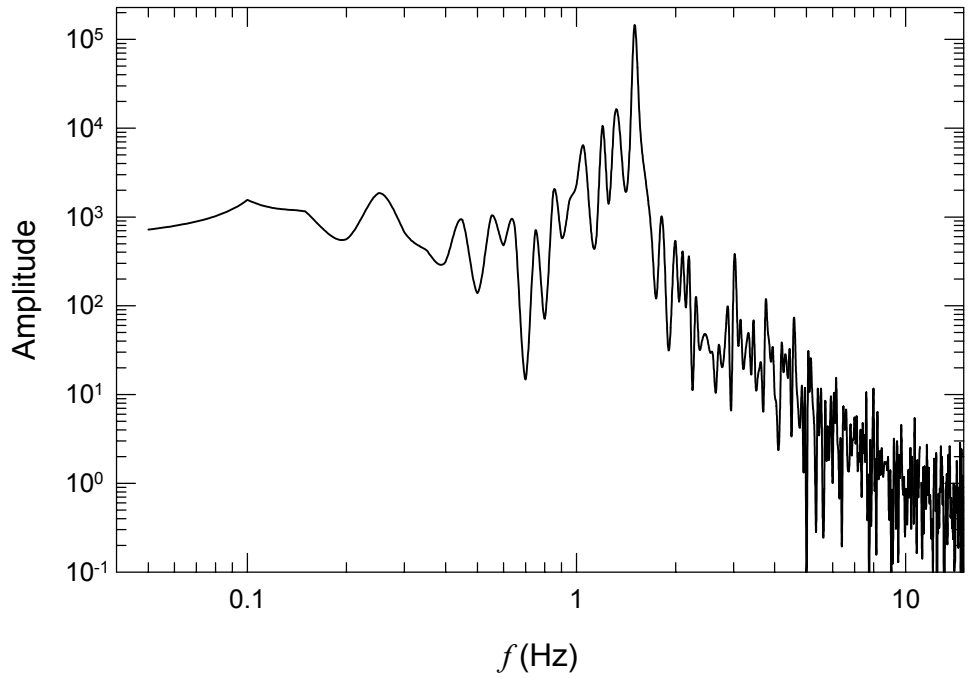

b)

Figure 3.12. a) The maximum projected canopy diameter and b) spectral content of the diameter for a 15 cm canopy at a freestream velocity of 30 cm/s.

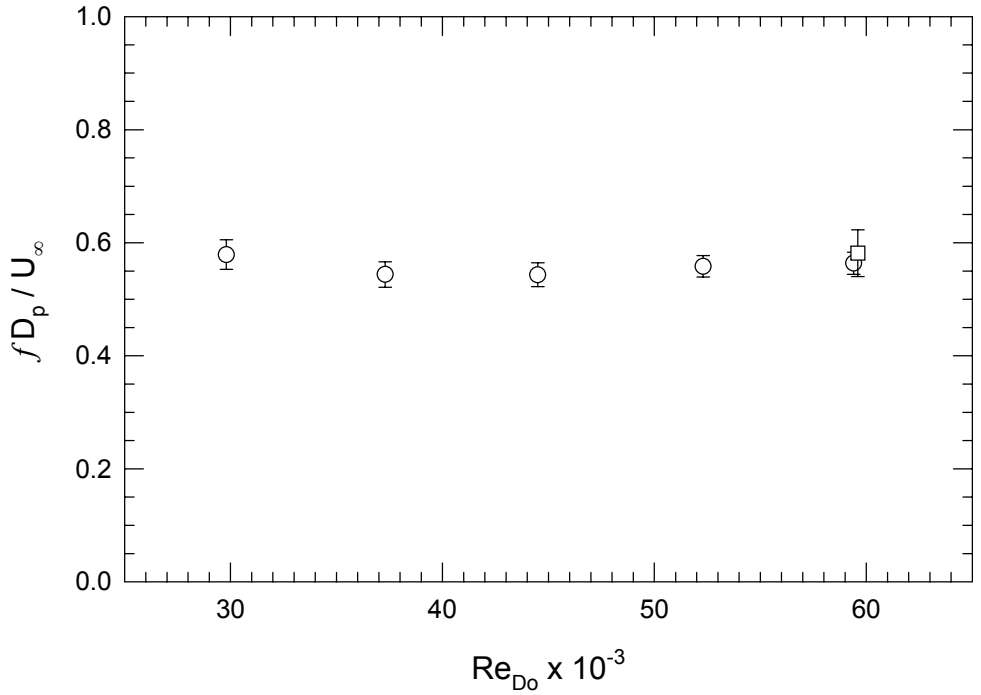

Figure 3.13. Dominant frequency of the canopy motions as a function of Reynolds number. The round symbols represent the 15 cm canopy and the square symbol represents the 30 cm canopy.

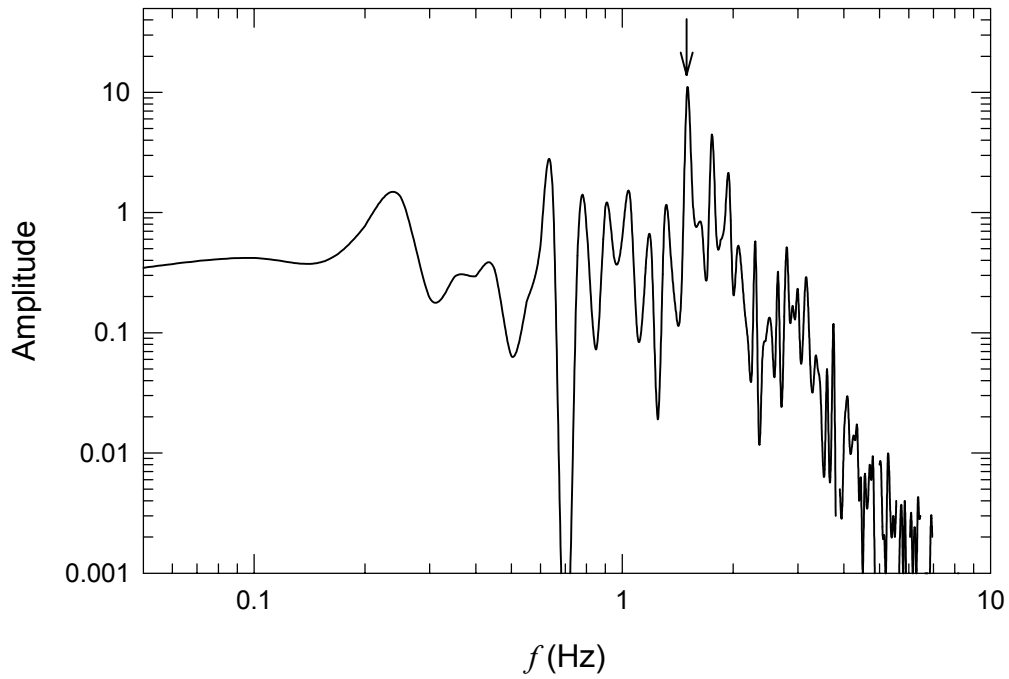

Figure 3.14. The spectral content of the force for a 15 cm canopy at a freestream velocity of 30 cm/s.

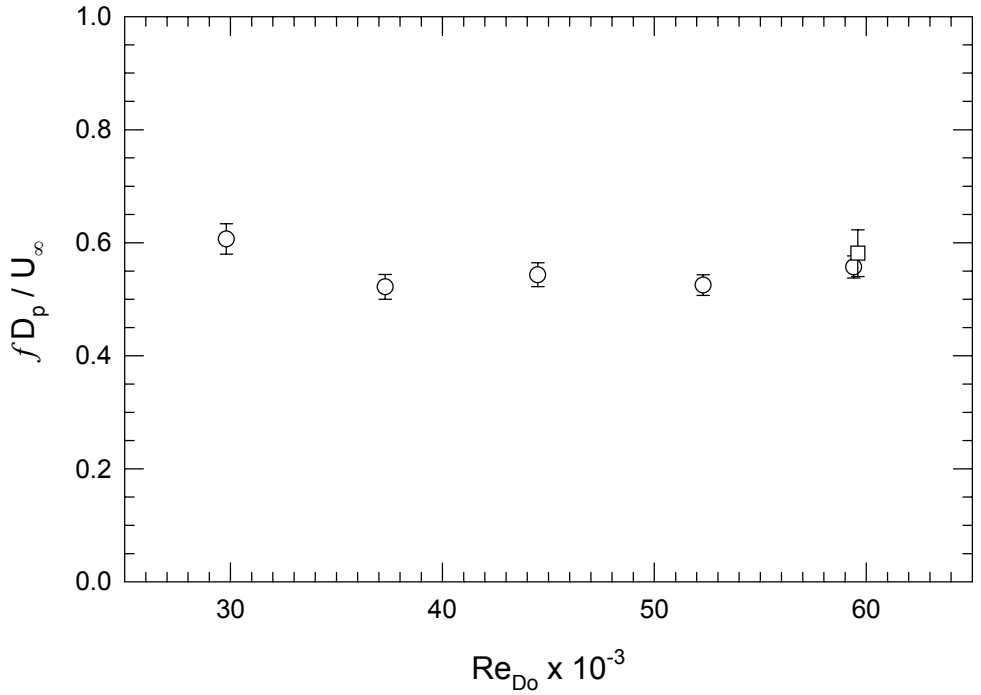

Figure 3.15. Frequency in the force measurements corresponding to the dominant frequency in the diameter measurements. The round symbols represent the 15 cm canopy and the square symbol represents the 30 cm canopy.

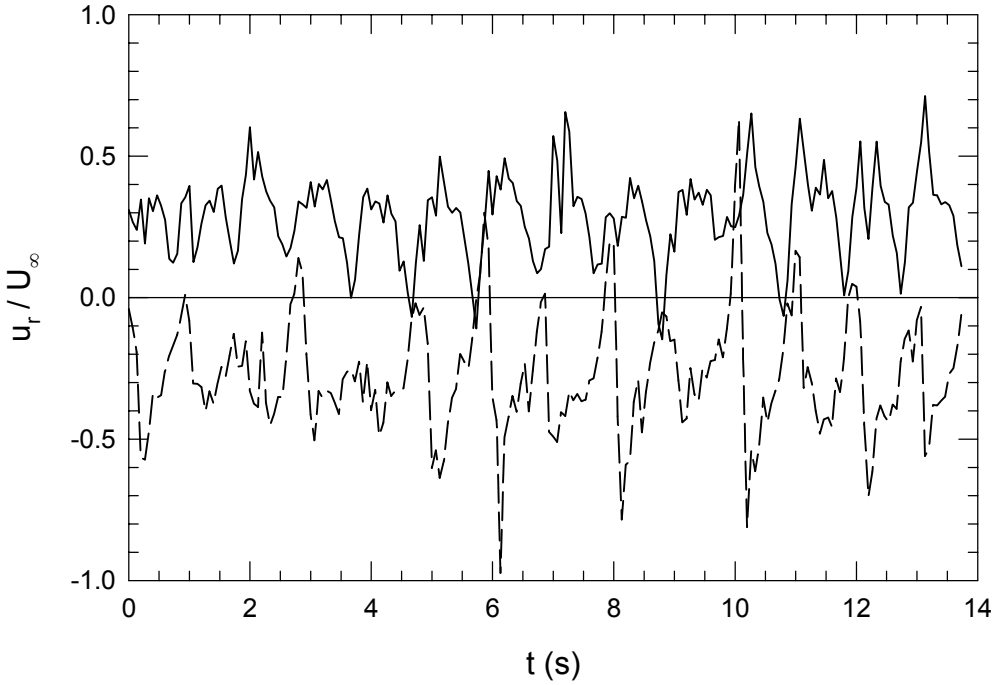

Figure 3.16. Radial velocities at points **A** (z/D_p = 0.25; r/D_p = 0.69 for the solid line and r/D_p = -0.69 for the dashed line) for the 15.2 cm canopy at $Re_{Do} = 3.0 \times 10^4$.

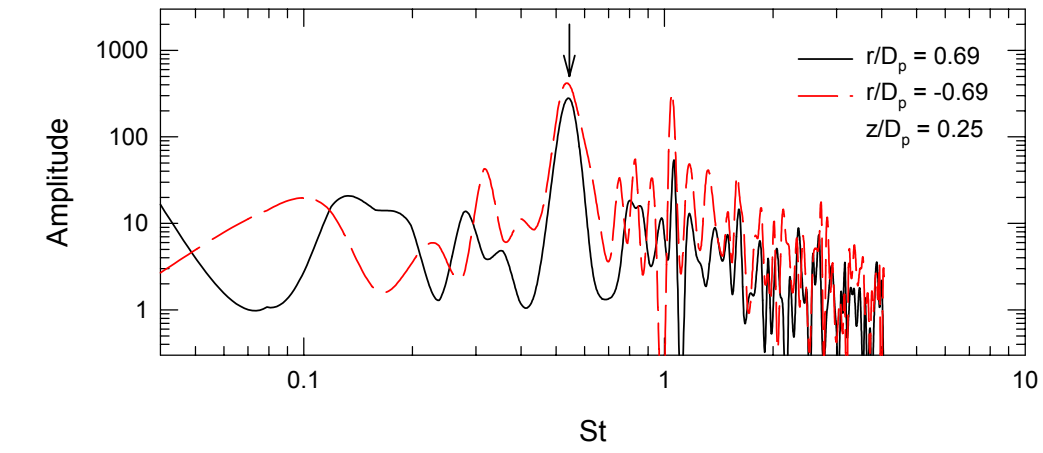

a)

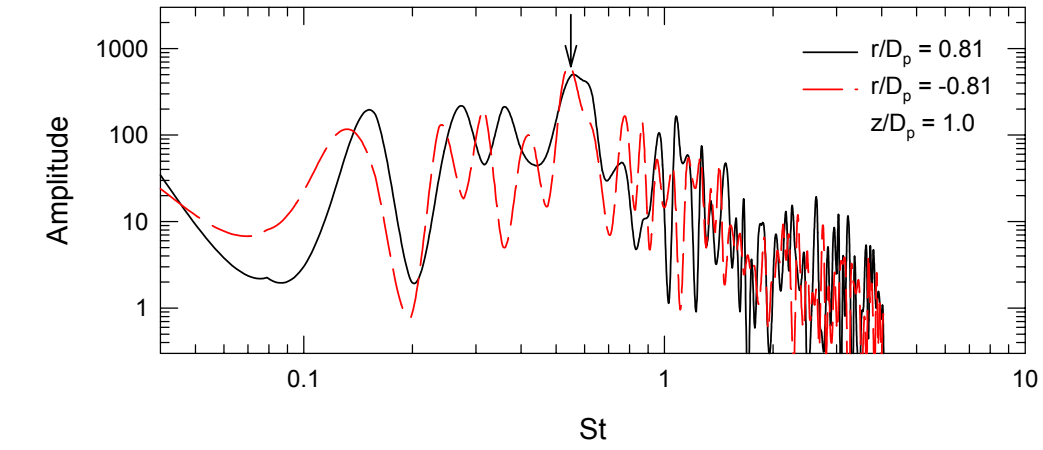

b)

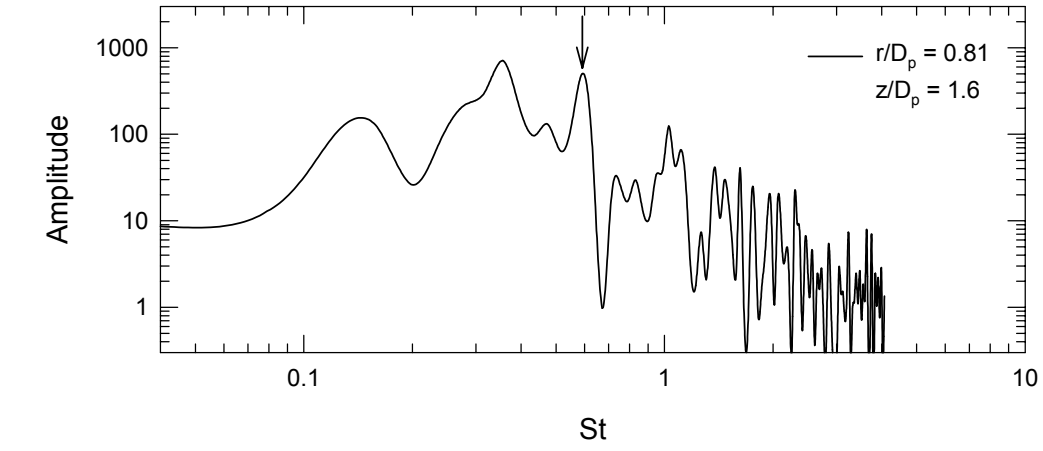

c)

Figure 3.17. Frequency spectrum of radial velocity at a) points **A**, b) points **B**, and c) point **C** for the 15 cm canopy at $Re_{Do} = 3.0 \times 10^4$.

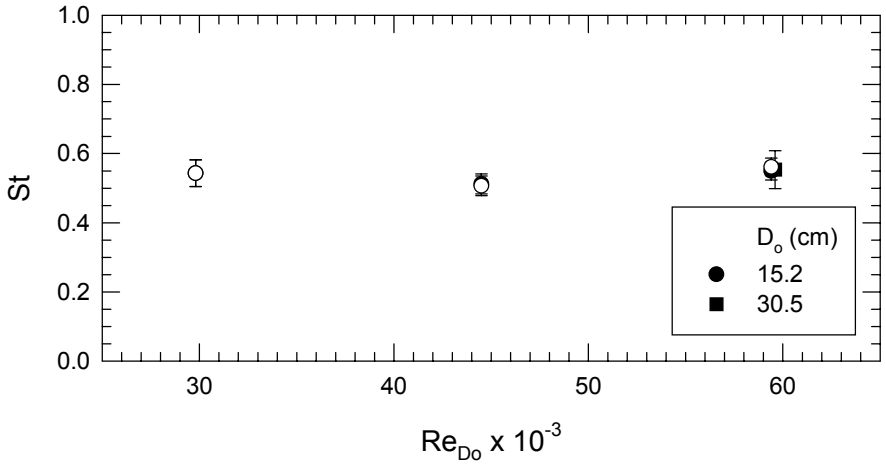

a)

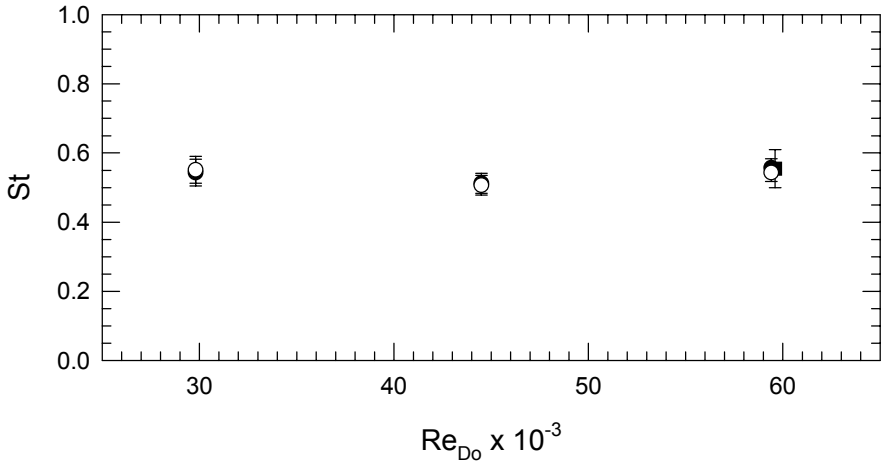

b)

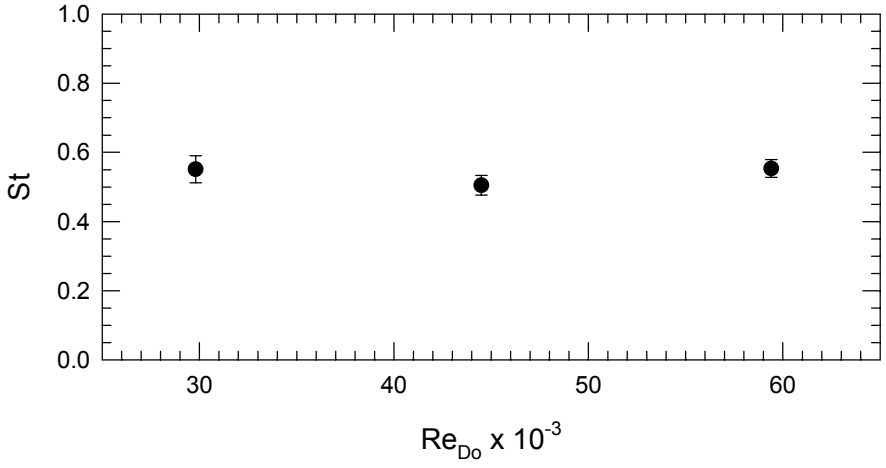

c)

Figure 3.18. Strouhal number of the radial velocity at a) points **A**, b) points **B**, c) points **C** listed in Table 3.1. The solid symbols represent the positive radial distances and the hollow symbols represent the negative radial distances.

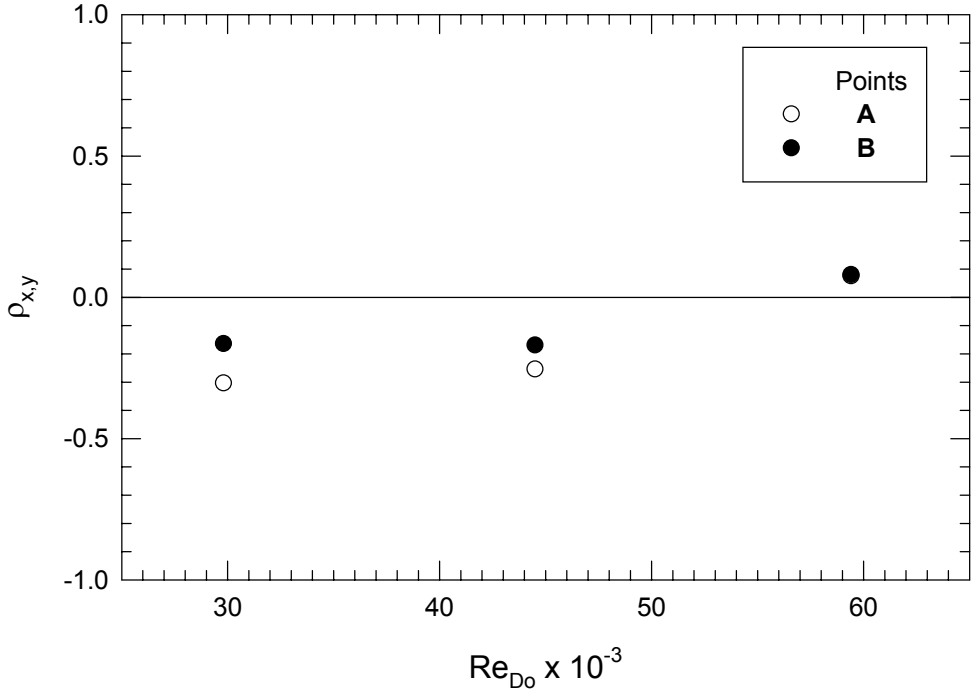

Figure 3.19. Correlation between symmetric radial velocity probe points for the 15.2 cm canopy.

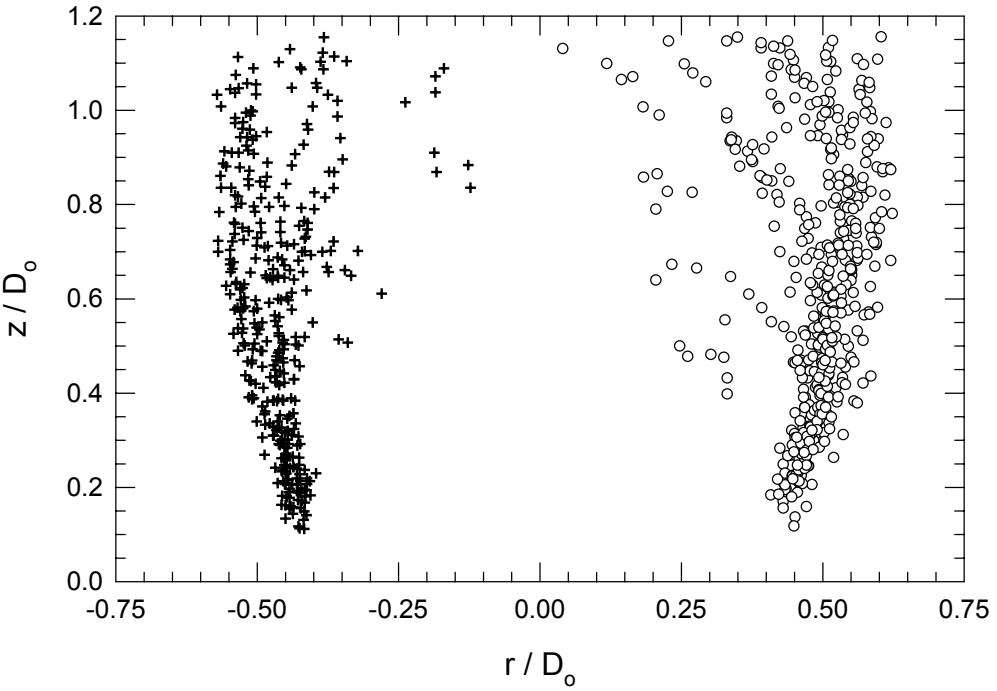

Figure 3.20. The vortex ring location over 14 shedding cycles. The round symbol is the location of the vortex on the right side of the canopy and the "+" symbol is the location on the left side of the canopy.

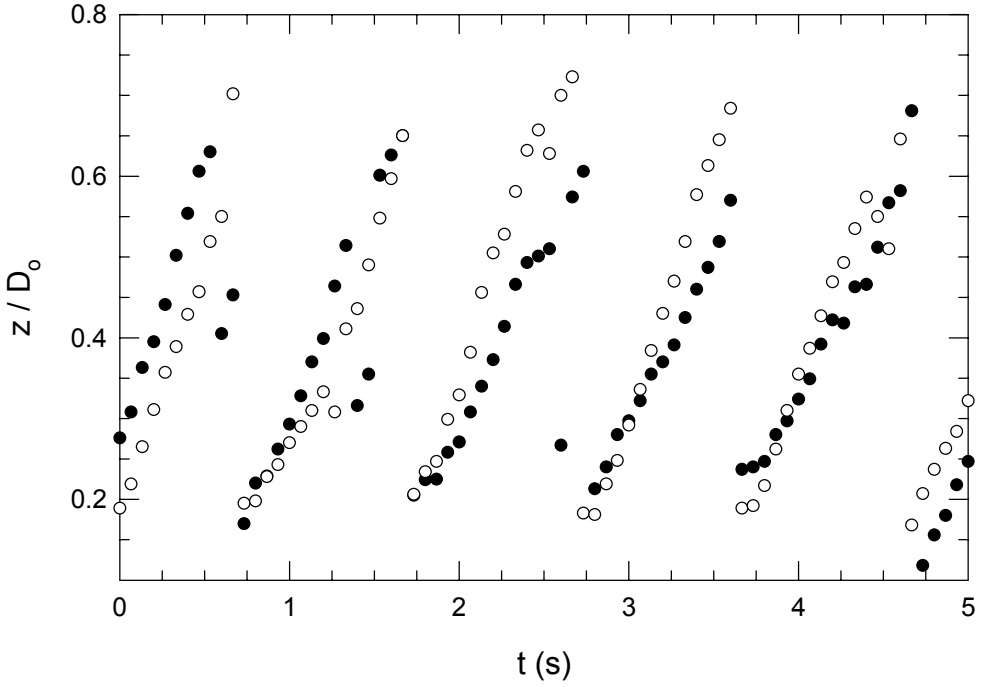

Figure 3.21. Downstream location of the vortex ring. The filled symbol represents the vortex shed from the right side of the canopy and the hollow symbol represents the vortex shed from the left side of the canopy.

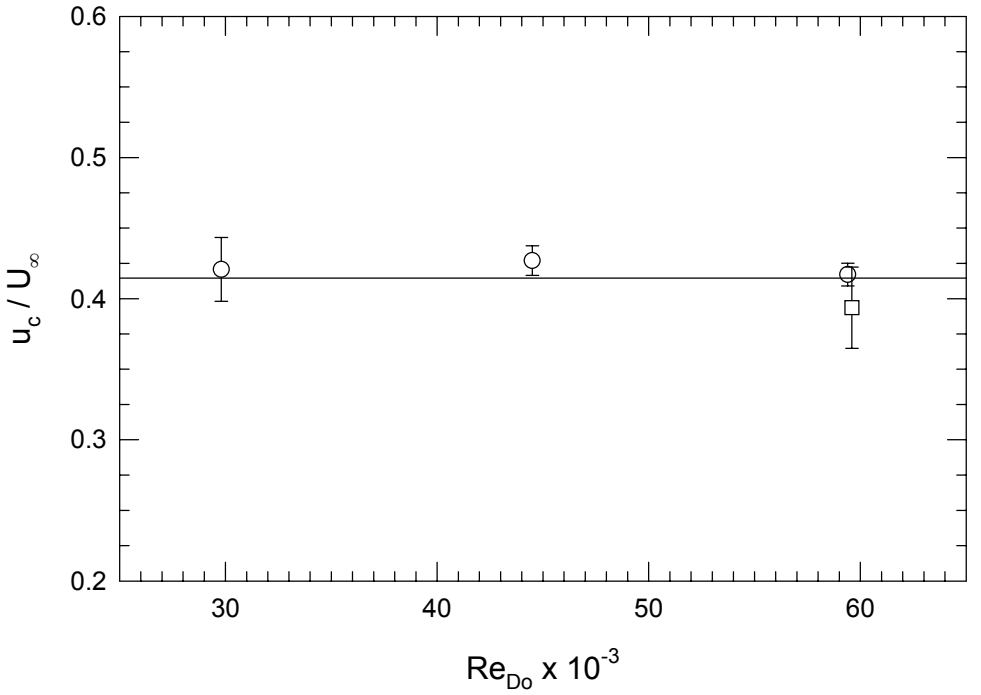

Figure 3.22. The celerity of the shed vortex over the range of Reynolds numbers examined. The round symbol represents the 15 cm canopy and the square symbol represents the 30 cm canopy.

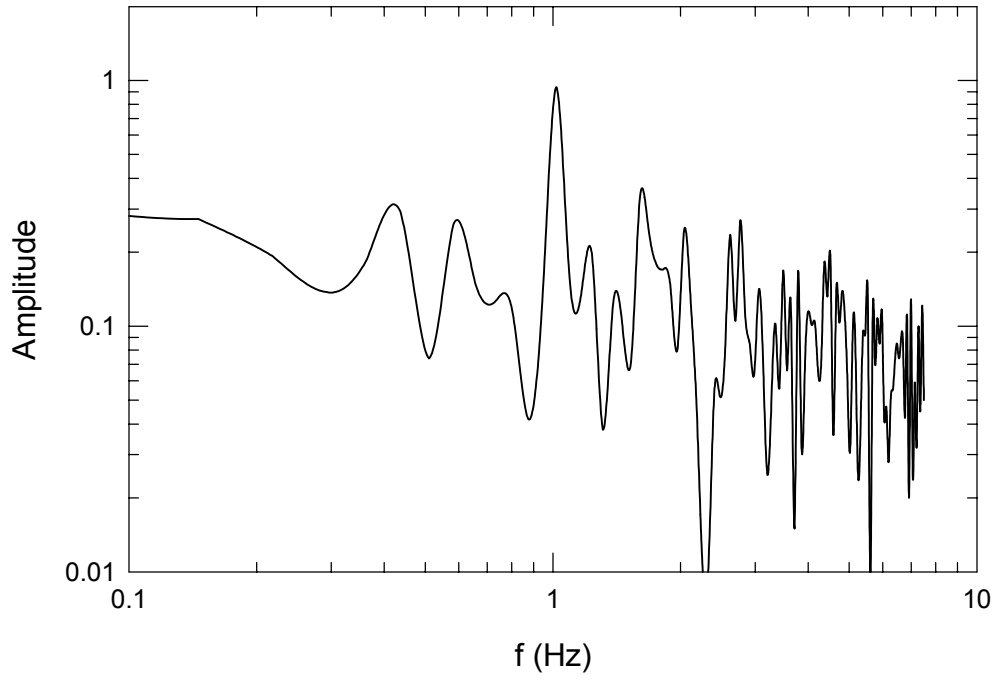

a)

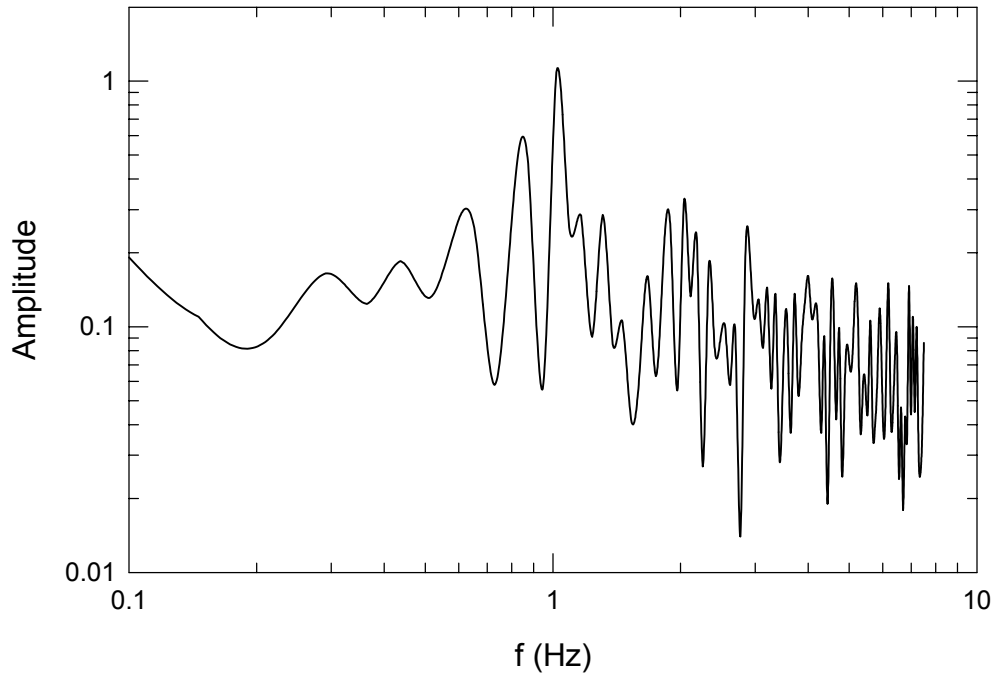

b)

Figure 3.23. The frequency spectrum of the shed vortex ring measured from the vortex tracking data; a) right side and b) left side of canopy.

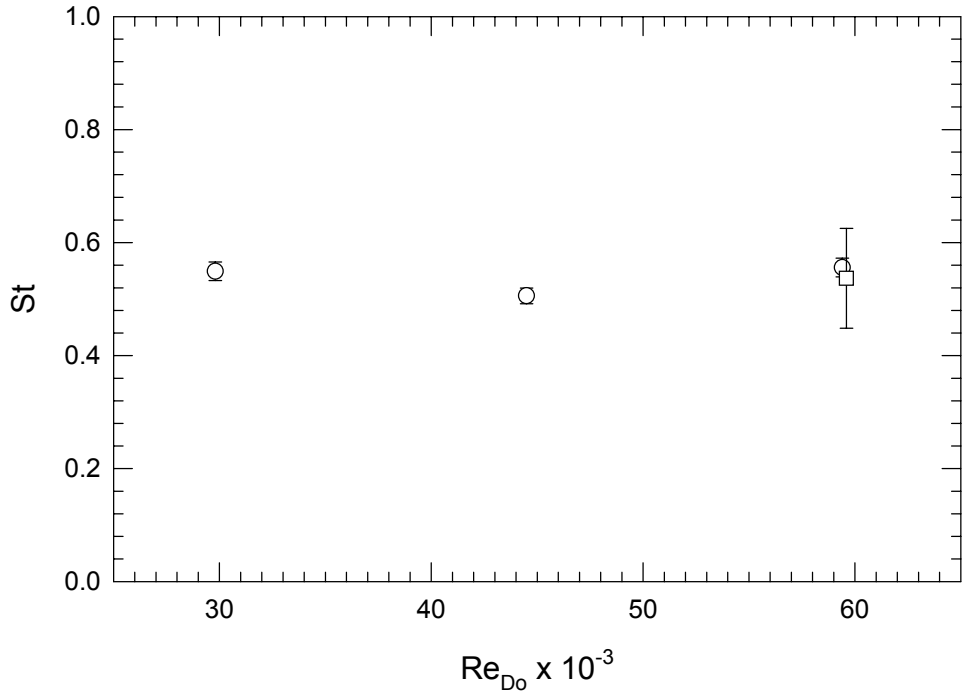

Figure 3.24. The Strouhal number of the shed vortex based on the vortex tracking measurements. The round symbols represent the 15 cm canopy and the square symbol represents the 30 cm canopy.

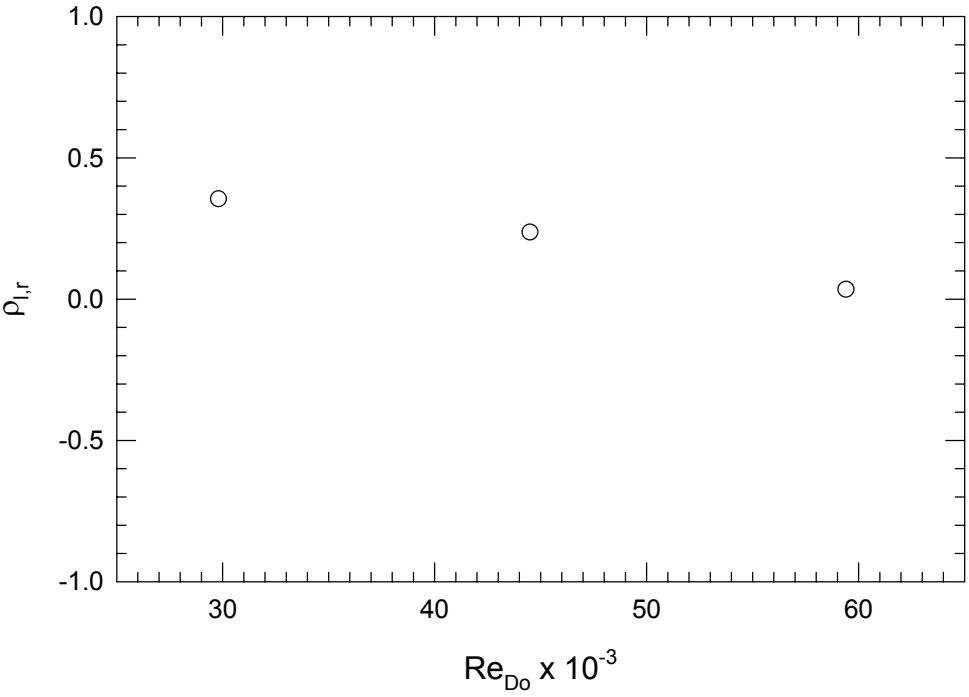

Figure 3.25. The correlation coefficient between the vortex location on the right and left side of the canopy.

4. Inflation of a Canopy

4.1 Dynamics of Canopy Evolution

The inflation of the parachute was conducted under an infinite-mass condition (*i.e.* the freestream velocity remained constant during the inflation). A typical inflation is shown in Fig. 4.1, where $D_o = 15.2$ cm and $U_\infty = 20$ cm/s which results in a Reynolds number of 3.0×10^4. The force the canopy experiences during the inflation and the diameter of the canopy are plotted in Fig. 4.2, where the labeled points correspond with the images in Fig. 4.1. Initially the canopy was packed into the deployment tube and the canopy was positioned such that the suspension lines were taut. At time $t = 0.0$ s, the deployment tube was pulled away (Fig. 4.1a) as indicated by the small bump in the force at that time. Once the deployment tube had cleared the canopy, it initially forms into a cylindrical shape (Fig. 4.1b) which then transitions into a conical or umbrella shape (Fig. 4.1c). Over this time period, the canopy diameter has grown to half its fully inflated diameter yet the force on the canopy has increased minimally. The fluid then proceeds to fill the canopy from the skirt towards the top of the canopy creating a nearly hemi-spherical canopy shape (Fig. 4.1d). At this point, the force has begun to increase towards its maximum value. With the upper regions of the canopy filled, the inflation of the canopy proceeded towards the skirt until the canopy diameter reached its steady state diameter (Fig. 4.1e). The maximum force the canopy experiences occurs after the canopy has become hemi-spherical in shape but before it achieves its maximum diameter. The peak force occurs over a small time duration in relation to the overall inflation time. The canopy then over-expands beyond its steady state diameter, achieving its maximum diameter in Fig. 4.1f. The force rapidly declines after achieving its maximum value. The

canopy diameter continues to increase towards its peak value while the force declines. The maximum diameter occurs approximately at the same time the force attains a minimum value. Afterwards, the force goes through a few oscillation in its amplitude before it approaches a mean value seen for a canopy in a steady flow. Similarly, after the maximum projected diameter was achieved, the canopy diameter shrinks and the canopy geometry begins to approach the behavior seen in a steady flow. During the inflation process, the canopy inflated nearly symmetrically and remained centered on the main axis. Only when the canopy had reached the over-expanded state did the canopy require the retention line (see Sec. 2.2) to restrain the off-axis motion.

Two characteristics of the small scale parachutes that differ from larger scale (*i.e.* quarter and half-scale models) and full scale parachutes should be noted. First, the initial conical shape that the small scale parachute exhibited is different from that of larger parachutes. Larger parachutes typically form a more cylindrical shape during this stage of inflation (see Fig. 1.1). The conical shape may be attributed to the material stiffness. At these small scales, the material stiffness becomes more apparent in terms of canopy flexibility (Heinrich & Hektner, 1971). The larger the parachute, the more flexible the canopy for a given material. Secondly, the maximum diameter of the small scale parachute typically occurred at the canopy skirt throughout the entire inflation process. While for full scale parachutes, the maximum diameter is not necessarily at the canopy skirt. During the inflation process of full scale parachutes, the canopy inflates from the top towards the skirt. During this time, the maximum diameter occurs at a point between the top and the skirt. Again, the stiffness of the small scale parachute affects the flexibility of the canopy restricting its motion more readily than a full scale parachute.

The inflation of canopies at a higher Reynolds number with two different canopy diameters was also conducted. The 15.2 cm canopy was also tested at a freestream velocity of 40 cm/s which results in a Reynolds number of 5.9×10^4 and a 30.5 cm canopy was tested at a freestream velocity of 20 cm/s ($Re_{Do} = 6.0 \times 10^4$). The tests at the larger Reynolds number showed an inflation process that more closely resembles larger canopy models or full scale canopies. The largest parachute model ($D_o = 30.5$ cm) most closely exhibited this behavior. This inflation sequence is shown in the images of Fig. 4.3 with the corresponding force and diameter traces in Fig. 4.4. The first two images (Figs. 4.3a-b) shows a canopy in a conical form, typical behavior for small scale parachutes during early inflation. The shape of the canopy then starts to transition into a more cylindrical shape (Figs. 4.3c-d). Through these phases the maximum diameter occurs at the canopy skirt. However, beginning with the fourth image (Fig. 4.3d), the canopy geometry resembles the shape of a full scale parachute where the maximum diameter occurs not at the skirt but closer to the top of the canopy while the skirt remains in a semi-collapsed state; the canopy forms a "mushroom" shape. The parachute then proceeds to fill, achieving its steady state diameter (Figs. 4.3f) and over-expanding to its maximum diameter (Figs. 4.3g). The size of the large canopy allows for greater flexibility of the canopy, and with the higher inertia of the water at the higher Reynolds number, the canopy more closely resembles the inflation of a full scale parachute.

Three specific times can be defined from the canopy force and diameter measurements to characterize the evolution of the canopy inflation. These characteristic times are the opening time, t_o, the filling time, t_f, and the maximum diameter time, t_{max}. In each of these definitions, the initial time (*i.e.* $t = 0$) is defined to be the time when the

deployment tube is first pulled away. Based on this, the *opening time*, t_o, is defined as the time at which the peak opening force is attained during the canopy inflation. The *filling time*, t_f, is the first time at which the diameter of the canopy first reaches its mean steady state diameter (Knacke, 1992). For an infinite mass inflation, experience has shown that the opening and filling times are approximately equal ($t_o \approx t_f$) while for a finite mass inflation the opening time is less than the filling time, $to < tf$ (Knacke, 1992). And the *time at maximum diameter*, t_{max}, is defined as the time when the canopy diameter achieves its maximum diameter during the inflation. The maximum diameter time occurs after the filling time, during the over-expansion of the canopy. The opening time will be used as the benchmark for comparison with other defined times due to the ease of determining its value and since the force measurements were sampled at a higher rate than the other measures. A schematic of the characteristic times is shown in Fig. 4.5. The average values for these characteristic times are listed in Table 4.1 with *rms*-values (*i.e.* the standard deviation) of the measurements.

Table 4.1. Characteristic times of canopy inflation.

D_o (cm)	Re_{Do}	t_o (s)	t_f (s)	t_{max} (s)	t_o*	t_f*	t_{max}*
15.2	3.0×10^4	1.47 ± 0.12	1.51 ± 0.19	1.78 ± 0.19	1.89	1.94	2.29
15.2	5.9×10^4	0.85 ± 0.17	0.81 ± 0.16	0.93 ± 0.15	2.18	2.07	2.40
30.5	6.0×10^4	2.71 ± 0.11	2.67 ± 0.12	3.22 ± 0.18	1.74	1.72	2.07

The uncertainty in these measures is directly related to the sampling frequency of the force and the image acquisition. The force was sampled at 150 Hz therefore the uncertainty in each opening time was ±3.3 ms (half the sampling period) while the imaging was performed at a rate of 30 Hz which results in an uncertainty of ±16.7 ms for each of the filling and maximum diameter times. Since for each condition the

experiments were performed multiple times, a variation in the measurement of the these times occurred. This results in a standard deviation of the times of 0.1-0.2 s, which is considerably higher than the uncertainty in each individual measurement. Therefore, the standard deviation was used to quantify the uncertainty of the characteristic times. The higher values for the standard deviations was a direct result of the inconsistencies in packing and folding of the canopy in the deployment tube.

It has been shown that the filling distance, the product of the freestream velocity and the filling time, should remain constant for a given parachute canopy (Knacke, 1992). This filling distance can be normalized with the constructed diameter to create a non-dimensional filling time,

$$t_f^* = \frac{t_f U_\infty}{D_o}. \tag{4.1}$$

Similar non-dimensional opening (t_o^*) and maximum diameter (t_{max}^*) times can be defined using the convective time scale of D_o/U_∞. The normalized characteristic times are plotted in Fig. 4.6 and also listed in Table 4.1. The plots show that the characteristic times remain nearly constant at least within the uncertainty of the measurements. The mean normalized filling time (over all Reynolds numbers and geometries) is 1.9 which is on the order of filling times found on full size parachutes and model tests at finite mass conditions. Heinrich & Noreen (1970) report normalized filling times on the order of 3.5 for a 3 ft. scale model with flat circular geometry. Lee (1989) states for finite mass ¼-scale flat circular canopies, the normalized filling times have a range of 2.25 – 3, and for full scale canopies the filling times are approximately 4. Additionally, Knacke (1992) reports normalized filling times of 2.9 for low porosity canopies and up to 4.7 for high

porosity canopies. The canopy in the present study would be classified as low porosity. The lower normalized filling time achieved in this study is due to the higher stiffness of the canopy (Johari & Desabrais, 2001).

An average opening force history was created by shifting each individual force measurement trial (at a given Reynolds number and scale) in time such that the peak opening forces were aligned and then an ensemble average of the force traces was performed. The resulting average force was normalized as a force coefficient, C_F, using Eq. 3.3 and the time was normalized using the opening time as,

$$\tau = \frac{t}{t_o}. \tag{4.2}$$

The normalized opening force is plotted in Fig. 4.7. All the inflations show similar trends in that during inflation the force remains quite small initially. At $\tau \sim 0.6\text{-}0.7$, the force begins to rise until at $\tau = 0.9$ it exhibits a rapid increase to its maximum value (at $\tau = 1.0$ by definition) after which the force decreases sharply where it begins to transition to a behavior seen in steady flow. The largest forces are confined to a short time duration centered around the peak value. Furthermore, the mechanisms causing this localized peak force are also confined to a small interval in time. This suggests that the dynamics of the canopy and the transient fluid mechanics are key to understanding the inflation process as whole.

The peak opening force coefficient is listed in Table 4.2. The values obtained in this study compare well to values obtained in inflation experiments conducted with similar scaled canopies (also listed in Table 4.2).

Table 4.2. Peak force and canopy diameter values.

D_o (cm)	Re_{Do}	$(C_F)_{max}$	$(D_m/D_o)_{max}$	fluid medium	reference
15.2	3.0×10^4	3.5	0.89	water	-
15.2	5.9×10^4	2.9	0.86	water	-
30.5	6.0×10^4	3.6	0.86	water	-
40	7.2×10^4	3.4	0.80	water	Lingard, 1978
80	4.8×10^5	2.0	0.75	air	Lingard, 1978

The canopy diameter measurements can also be ensemble averaged in a similar fashion as the force measurements. For comparison with the averaged force measurements, the diameter measurements were shifted in time such that the alignment point was again the time when the peak opening force occurred. The diameter measurements were sampled at a rate considerably less than the force measurements (*i.e.* 30 Hz as opposed to 150 Hz). Therefore, its was necessary to identify the image frame where that the peak force occurred in each run. These points were then used as the alignment points and an ensemble average was calculated for the three cases studied. The results of these calculations are shown in Fig. 4.8, where the diameter has been normalized with the constructed diameter, D_o, and the time has been normalized with the opening time. Heinrich (1969) and Heinrich & Noreen (1968) have experimentally shown that the normalized canopy diameter varies linearly with the normalized time initially before transitioning to a quadratic behavior. Their experiments were performed with a 91 cm parachute model tested in a wind tunnel, under both infinite and finite-mass conditions. For a normalized time greater than one, the diameter varies with the square root of the normalized time squared. Heinrich (1969) noted that the results obtained for the finite mass case could be applied to the infinite mass case at least over the range $0 \leq \tau \leq 1.0$ excluding the amplitude of the peak maximum projected diameter. Since all

the canopies examined in this study are geometrically similar and the averaged diameter data seems to collapses on to a single curve (see Fig. 4.8), a function of the form suggested by Heinrich and Noreen (1968) was fitted to the averaged canopy data. The results of the least-squares curve fitting is shown in Fig. 4.8 and Eq. 4.3.

$$\frac{D_m}{D_o} = \begin{cases} 0.032 + 0.626\tau & \text{for } 0.2 < \tau < 0.8 \\ 1.96 - 4.21\tau + 3.04\tau^2 & \text{for } 0.8 \le \tau \le 1.0 \\ 0.541 + \sqrt{0.100 - (\tau - 1.197)^2} & \text{for } 1.0 < \tau \le 1.3 \end{cases} \qquad 4.3$$

The Heinrich & Noreen (1968) relation is also plotted in Fig. 4.8. The numerical coefficients in Eq. 4.3 are different than those given by Heinrich & Noreen; however, the functional form of the relations are validated by the quality of the curve fit to the data. Berndt & DeWeese (1966) imaged the inflation of full-scale canopies and derived an empirical relationship for the canopy diameter. This relationship is also plotted in Fig. 4.8. It is evident that there are deviations between full-scale and small-scale models. Heinrich & Noreen (1968) also observed this and stated,

> "It is possible that the relatively higher stiffness of the parachute model causes this deviation during the early phase and it would probably be necessary to investigate this region in more detail when an attempt is made to utilize the results of the model experiments for calculation of filling processes of large parachutes."

It should be noted that in the Berndt & DeWeese (1966) and the Heinrich & Noreen (1968) studies, the time was normalized with the filling time instead of the opening time. Since the opening time is approximately equal to the filling time for an infinite mass inflation, this would at most cause a change in the coefficients.

The results obtained in the current study achieved a higher normalized diameter than that obtained by Heinrich & Noreen (1968). This behavior is exhibited by larger slopes of the curves and the higher peak projected diameters achieved. The peak maximum normalized projected diameters, $(D_m/D_o)_{max}$, achieved are shown in Table 4.2. Heinrich (1969) reports a maximum projected diameter ratio of $(D_m/D_o)_{max} \approx 0.7$ for an infinite mass inflation of a 91 cm model in a wind tunnel at $Re \sim 10^6$ and Lingard (1978) reports values of $(D_m/D_o)_{max} \approx 0.75$-$0.80$ for a constant velocity inflation in air and water (see Table 4.2). It is expected that the higher stiffness of the small canopy models resulted in the higher values of the maximum projected diameters.

The volume that the canopy enclosed, V, was estimated from the images of the canopy inflation assuming that the canopy was axisymmetric during the inflation. The details of the volume estimation method are given in Section 2.3. A sample of the transient enclosed volume for a 15 cm canopy at $Re_{Do} = 3.0 \times 10^4$ is shown in Fig. 4.9. An average enclosed volume was calculated by alignment of the peak force, using the same method explained in the averaging of the canopy diameter. The average enclosed canopy volume is shown in Fig. 4.10, where the enclosed volume was normalized by the mean enclosed volume, V_{steady}, when the canopy is under steady flow conditions. All the inflations show a continual increase in the volume enclosed by the canopy until just after the time that the peak opening force occurs ($\tau = 1.0$). The canopy then over-expands and rapidly approaches the steady state volume. From the enclosed canopy volume, estimates of the unsteady potential flow are possible using the expressions employed in Section 3.2. Details of these calculations are presented in Section 4.4.

4.2 Flow Field Evolution

The canopy geometry and the forces that the canopy experiences during inflation are directly related to the evolution of the flow field surrounding the canopy. The velocity field in a plane was measured in the near wake of the canopy and the azimuthal vorticity field in that plane was calculated. From observations of these fields during the inflation process, it was possible to characterize the inflation process into three distinct stages, with each stage defined by the state of the boundary layer around the canopy. The stages are as follows: I. the initial canopy inflation where the boundary layer stays completely attached to the canopy; II. the point at which boundary layer separates from the canopy surface near the apex and the separation point moves upstream along the canopy surface; and III. the point where the boundary layer completely separates from the canopy at its skirt and transitions to a fully inflated canopy in steady flow. It should be noted that these results can only be drawn for an infinite mass case at this time since no data was collected for finite mass inflations.

A sample of the evolution of the vorticity field around a 15 cm canopy with a freestream velocity of 20 cm/s is shown in Fig. 4.11. The thick green line in each of the plots is an approximation of the canopy outline in the measurement plane. The measured force and diameter for this specific inflation is plotted in Fig. 4.12 with the labeled points corresponding to the images in Fig. 4.11.

Initially the canopy was packed into the deployment tube and the canopy was positioned such that the suspension lines were taut. At time $t = 0$ s, the deployment tube is pulled away. Once the deployment tube clears the canopy, the canopy begins inflating immediately into a conical, umbrella shape, (Figs. 4.11a-b) with the projected frontal area

increasing. During this initial inflation stage, the force has remained essentially constant (Fig. 4.12). The vorticity fields show that the boundary layer along the canopy surface is fully attached to the canopy with the possible exception of the area very near the canopy apex where minor vortex shedding is occurring. At this point in time (Fig. 4.12, points c-d), the force starts to increase in value even while the canopy geometry has retained a shape similar to its previous form. Over this same interval (points c-d), the canopy diameter has grown by approximately 50%, yet the general characteristics of the vorticity field have remained unchanged. The boundary layer was still attached to the canopy surface (Figs. 4.11c-d). This sequence represents stage I of the inflation process.

The essence of the canopy behavior and the surrounding flow field begins to transition into another stage from this point forward. The general shape of the canopy has begun to transform from a conical shape to a more hemi-spherical shape (Figs. 4.11d-e). The boundary layer also changes its behavior at this point. The end of the boundary layer starts to separate from the surface of the canopy near the apex (Figs. 4.11e-f). This initiates the beginning of stage II of the inflation process. The separated region of the boundary layer becomes highly disorganized while the rest of the boundary layer remains attached to the canopy surface farther upstream (*i.e.* the region closer to the canopy skirt). The point where the vorticity contours separate from the canopy surface (Figs. 4.11f-i) begins to travel upstream towards the canopy skirt while the canopy diameter progresses through its steady state shape (*i.e.* the filling time, Figs. 4.11g-h) and then to an over-expanded condition. With the upstream movement of the separation point, the force passes through its maximum value (Fig. 4.12, point h) and then falls off sharply. Following the time when the maximum force occurs, the boundary

layer separates completely from the canopy lip (Fig. 4.11i) and rolls-up into a vortex ring near the skirt. This initiates stage III of the inflation process. The separated flow can be confirmed by the existence of opposite signed vorticity between the canopy surface and the boundary layer (Figs. 4.11i-j). The vortex ring formed from the roll-up of the boundary layer has been dubbed the unloading vortex since it occurs during the rapid reduction of the force or the "unloading" of the canopy. Subsequent to the separation of the boundary layer from the canopy skirt, the maximum diameter was achieved (Figs. 4.11j).

The separated boundary layer becomes similar to a conventional shear layer attached at the canopy skirt. The shear layer remains separated at the canopy edge and eventually the formation of the vortex is completed (Figs. 4.11k-n). This vortex ring eventually separates from the feeding shear layer and is conveyed downstream, initiating the process of wake formation behind the canopy as seen in canopies exposed to a steady flow. The canopy diameter and force also begin to change to the behavior seen with a canopy in steady flow (Figs. 4.12k-n).

Similar flow field characteristics were observed at the other two conditions examined in the study. An inflation of a 30 cm canopy at $Re_{Do} = 6.0 \times 10^4$ is shown in Fig. 4.13, with the corresponding force and diameter measurements in Fig. 4.14. The same trends can be identified in the inflation where the force only rises minimally during stage I of the inflation (*i.e.* the boundary layer remains attached to the canopy surface, Figs. 4.13a-d). Then, the boundary layer separates (the beginning of stage II) from the surface (Fig. 4.13d) near the apex region while the remainder of the boundary layer stays attached to the canopy. The separated portion of the boundary layer became highly

disorganized and the separation point traversed towards the canopy skirt (Figs. 4.13d-k) during which time the peak opening force occurred (Fig. 4.13i-j). The separation point reached the canopy skirt (stage III, Fig. 4.13k) and the unloading vortex began to form. The maximum diameter was achieved (Fig. 4.13l) shortly after the time the peak opening force occurs. The unloading vortex was fed vorticity from the separated boundary layer until it separates from the canopy and was conveyed downstream (Figs 4.13l-n).

The general characteristics of each stage of the inflation process can be summarized as follows. During stage I of the inflation, the boundary layer remains attached to the canopy surface as the volume enclosed by the canopy increases as a result of the increase in the diameter of the canopy. The shape of the canopy during this stage of inflation is a conical shape, at least on the small scale model canopies studied. The boundary layer sheds only small weak vortices near the apex, forming a narrow wake region confined to an area directly behind the canopy. However, over the majority of the canopy surface, the boundary layer remains attached. A rigid, static bluff body with a similar shape in a constant freestream would not be able to sustain this attached boundary layer. The flow would separate from the rigid body at the leading edge. The motion of the canopy surface, due to its flexible nature, allows for the boundary layer to remain attached to the canopy. While the boundary layer remains attached to the canopy, the drag of the canopy rises minutely even as the canopy diameter substantially grows at a steady rate.

The stage II initiates with the local separation of the boundary layer from the apex region of the canopy surface. This stage sees the most drastic changes in the flow field and the canopy behavior. The separated ends of the boundary layer become disorganized

and cause the wake of the canopy to grow in a significant manner. The separation location along the canopy surface moves from the apex region towards the canopy skirt. This causes the size of the wake to increase to the order of the canopy diameter. During this stage, the force rapidly rises to its peak value with an almost equally sever decline in the force afterward. The shape of the canopy also transforms from its conical shape to the hemi-spherical cross-section seen previously in Section 4.1. However, the canopy diameter continues to grow during this stage.

The final inflation stage begins with the separation of the boundary layer from the canopy skirt. A large unloading vortex ring is formed at the outer edges of the canopy from the fully separated boundary layer. The canopy diameter is drawn out to its maximum value during this formation process. The vortex formation creates a low pressure region at the canopy edge, causing the canopy diameter to increase to its maximum diameter. The separated boundary layer should be more properly called a shear layer at this point since it is now similar to the shear layers seen in typical bluff body flows. The complete shedding of the unloading vortex ring initiates the development of the wake typically seen in a fully inflated canopy in a steady freestream. The shear layer continually sheds vortices in a periodic manner from this point forward. The canopy begins the cyclic breathing phenomena described in Chapter 3.

The beginning of each inflation stage can be defined with a time, for example stage II inflation starts at $t \equiv t_2$ and similarly stage III begins at $t \equiv t_3$. The separation times are listed in Table 4.3 for each condition studied.

Table 4.3. Boundary layer separation times.

D_o (cm)	Re_{Do}	t_2 (s)	t_3 (s)	τ_2	τ_3
15.2	3.0×10^4	1.08 ± 0.19	1.52 ± 0.21	0.79	1.10
15.2	5.9×10^4	0.59 ± 0.11	0.88 ± 0.17	0.71	1.05
30.5	6.0×10^4	2.33 ± 0.43	3.63 ± 0.54	0.66	1.02

The uncertainty in these times is ±0.033 s for 15 cm canopy and ±0.067 s for the 30 cm canopy which is half the sampling period of the velocity field measurements for the 15 cm canopy and a full period for the 30 cm canopy. However, these values are significantly less than the standard deviations of the measurements so the standard deviations were used as an estimate for the uncertainty in the separation times. The selection of the separation times is a somewhat arbitrary process since in the strictest sense the point of separation is defined as the point where the wall shear stress becomes zero. However due to the spatial as well as the temporal resolution of the velocity field measurements made in these experiments, it was not possible to apply this criteria for selecting the point in time when the boundary layer separated from the canopy surface. It is quite clear though that a dramatic change occurs in the behavior of the vorticity fields at the time the flow separates. It is from these observations that the separation times are estimated.

Normalizing the separation times with the opening time shows the relationship between the opening shock and the flow field behavior. The normalized separation times, $\tau_2 \equiv t_2/t_o$ and $\tau_3 \equiv t_3/t_o$, are plotted in Fig. 4.15 and listed in Table 4.3. A small Reynolds number dependence is apparent from the data. But it is quite clear that the onset of the boundary layer separation happens prior to the opening shock. The formation of the unloading vortex begins after the boundary layer has completely

separated from the canopy skirt. Therefore, since this separation begins after the opening shock has already occurred, the unloading vortex is not the cause of the opening shock. The opening shock takes place between these two points. It is clear that the boundary layer separation process is responsible for the opening shock. A detailed analysis of the canopy kinetics is presented in Section 4.4 below.

The diameter of the canopy, D_{t2} and D_{t3}, at the two separation times are listed in Table 4.4. The mean steady state diameter, D_p, was used to normalize the separation diameters. The uncertainty values listed is based on the standard deviation of the measurements which was higher than any uncertainty in the measurement of the canopy diameter or the vorticity field timing. The boundary layer first separates once the canopy reaches approximately two-thirds of its mean steady state diameter. It should be reminded that this separation point is not at the leading edge of the body (*i.e.* the canopy skirt) but near the apex region of the canopy. For a rigid and static bluff body with a shape similar to the canopy at the first separation time, the flow would separate at the leading edge. The boundary layer only separates from the canopy skirt when the canopy diameter has over-expanded to ~10% of its steady state value. This shows that the dynamic nature of the flexible canopy material is an important characteristic of the overall flow field behavior.

Table 4.4. Boundary layer separation diameters.

D_o (cm)	Re_{Do}	D_{t2} (cm)	D_{t3} (cm)	D_{t2} / D_p	D_{t3} / D_p
15.2	3.0×10^4	8.3 ± 1.9	13.1 ± 0.5	0.71	1.14
15.2	5.9×10^4	7.3 ± 0.9	12.6 ± 0.7	0.65	1.12
30.5	6.0×10^4	15.8 ± 2.7	25.1 ± 1.1	0.68	1.08

4.3 Integral Measures of the Wake

The circulation, Γ, of the boundary/shear layer was calculated from the velocity field using the definition of the circulation, namely,

$$\Gamma \equiv \oint_s \vec{u} \cdot d\vec{s} \qquad 4.4$$

where $\vec{u}$ is the velocity along the path s. The path of integration selected was one along a constant value of positive vorticity that surrounded the maximum value of vorticity in the neighborhood of the canopy. The value of the vorticity contour used in the calculation is listed in Table 4.5.

Table 4.5. Vorticity level of integration path.

D_o (cm)	U_∞ (cm/s)	Re_{Do}	$\vec{\omega}$ contour-level (s^{-1})
15.2	20	3.0×10^4	5.0
15.2	40	5.9×10^4	15.0
30.5	20	6.0×10^4	5.0

An example of the temporal evolution of the circulation for a 15 cm canopy at $Re_{Do} = 3.0 \times 10^4$ is shown in Fig. 4.16. An ensemble average of the circulation was calculated by time shifting the individual temporal circulation plots such that the time the peak force occurred were aligned (the same method described in Section 4.1). The average temporal evolution of the circulation for each condition tested is plotted in Fig. 4.17. The solid line in the plots is a 5-point moving window average of the data and the vertical dotted lines represent the separation and opening times as labeled.

The evolution of the circulation behaves much as expected. Initially the circulation is at a minimum, nearly constant level up until the boundary layer starts to separate at $t = t_2$. The circulation then begins to increase in value as the boundary layer separation point moves along the canopy surface, increasing the amount of vorticity in

the flow field. The separated boundary layer produces large amounts of vorticity. Once the boundary layer completely separates from the canopy at the skirt ($t = t_3$), the quantity of vorticity begins to level out. This is the point where the unloading vortex is taking shape. The amount of vorticity contained in the unloading vortex will continue to increase as long as it remains attached to the shear layer. However once it separates from the shear layer, the vorticity contained will remain constant and therefore its circulation will also remain constant until it begins to decay or the vorticity is canceled by opposite signed vorticity. The method used to calculate the circulation only examines a single signed vorticity above the values listed in Table 4.5 so the plots in Fig. 4.17 will level out to a constant value after $t \sim t_3$. Only the unloading vortex was tracked for its circulation and not the shear layer that occurs after the unloading vortex is shed from the canopy. So even though additional vorticity is being introduced into the flow field from the shear layer, the circulation values plotted in Fig. 4.17 only reflects the circulation of the unloading vortex.

Normalizing the circulation with the freestream velocity and the constructed diameter (*i.e.* $\Gamma/(U_\infty D_o)$) shows that, during the inflation of the canopy (when $t_2 \le t \le t_3$), the time history of the circulation in the separating boundary layer remains the same across the range of Reynolds numbers and geometry studied. The normalized circulation is plotted in Fig. 4.18. The normalized circulation of the unloading vortex levels out to a value of approximately unity after the canopy inflation is complete (*i.e.* $t \ge t_3$). The time it takes for the vortex circulation to approach this value is $t \cdot U_\infty / D_p \approx 3\text{-}4$. This normalized vortex formation time is on the same order as that seen for the formation of

impulsively started vortex ring. Gharib *et al.* (1998) showed that the vortex ring formation time of an impulsively started jet was in the range 3.6-4.5.

The fluid impulse of the wake region is a measure of the momentum contained in the wake. In Section 1.4, it was shown that the rate of change of the fluid impulse provides an estimate of the amount of force the fluid imposed on the canopy due to the vorticity contained in the wake. During the inflation of the canopy, the vorticity is primarily confined to the boundary layer on the canopy surface and the unloading vortex that results from the separation of the flow. The impulse for each inflation was calculated using Eq. 1.8 where the area of integration used was a rectangular region which enclosed the vorticity from the centerline of the canopy radially outward and axially from the canopy skirt in a downstream direction (see Section 2.5 for a more complete description). In order to minimize the noise introduced to the impulse calculations from the background vorticity, any vorticity values less than those listed in Table 4.5 were set to zero during the calculation. An example of the result of the impulse calculation is shown in Fig. 4.19.

An ensemble average of the impulse was performed at each test condition, using the method of time shifting described earlier. The results of this analysis is shown in Fig. 4.20 where the solid line is a 5-point moving window average of the data and the vertical dotted lines represent the separation and opening times as labeled. The averaged data show that initially the flow impulse has a minimum value with only a small increase during the stage I inflation phase. Once the flow begins to separate (at the onset of stage II inflation), the impulse starts to rapidly increase, suggesting that the amount of momentum contained in the wake has also increased. To accommodate this change in

momentum, a larger force is need to restrain the canopy in the fluid (*i.e.* the fluid exerts a larger force on the canopy). After the flow has completely separated at $t = t_3$, the rate of the impulse increase appears to approaches a constant value (*i.e.* the impulse becomes linear). The impulse can be normalized as

$$\frac{I_z}{q_o S_o t_o}. \tag{4.5}$$

The normalized average impulse is shown in Fig. 4.21. This normalization shows that under each inflation condition, similar amounts of fluid impulse are generated. From the impulse calculation, estimates of the vortical force are made.

4.4 Composition of Fluid Dynamic Forces on the Canopy

A relationship for calculating the force that the canopy experiences based only on measurements of the flow field was derived in Section 1.4. The force the canopy experiences from the flow field is attributable to two primary sources; the unsteady potential flow associated with the change in the volume of the canopy (*i.e.* the apparent mass of the flow) and that associated with the production of vorticity in the wake (*i.e.* the rate of impulse production).

The unsteady potential flow around the canopy produces a force which is related to the enclosed volume of the canopy. It was shown in Eq. 1.11, (and repeated here for clarity)

$$F_p = k_p \rho U_\infty \dot{V}, \tag{4.6}$$

that the potential force is proportional to the time rate of change of the enclosed volume. This is true as long as the canopy is not decelerating. For the cases examined in this

study, the freestream velocity was maintained at a constant value (*i.e.* the infinite mass condition). The enclosed volume of the canopy was estimated from the images of the canopy as described in Section 4.1. From these measurements, the derivative of the volume was estimated using a central differencing scheme and assuming the proportionality constant k_p as unity. The potential flow force history plotted against the ensemble-averaged force peak is shown in Fig. 4.22. The potential force grows in a nearly linear fashion from an initially zero value until just prior to the opening time when the potential force reaches its maximum value. After achieving its peak value, the potential force drops precipitously to values that oscillate around a zero mean value. The peak value of the potential force is small in relation to the total peak force during the inflation. Typically, the peak potential force achieved during the inflation was 7-9% of the peak opening force under the assumption that $kp = 1$.

The potential force was normalized to a potential force coefficient as

$$C_{F_p} = \frac{F_p}{q_o S_o} \tag{4.7}$$

which is plotted in Fig. 4.23. The data collapses to a single curve with some scatter around $\tau \sim 0.7$. The solid line in Fig. 4.23 is the average of all three conditions. The peak value occurs at $\tau \sim 0.95$, nearly aligned with the opening shock at $\tau = 1$.

The forces associated with the vorticity containing regions of the flow (*i.e.* the vortical force) are calculated from the time derivative of the flow impulse. The relation for this calculation was given in Eq. 1.9 as

$$F_\omega = \frac{dI_z}{dt} = -\pi\rho \frac{d}{dt} \iint r^2 \omega_\theta dr dz \,. \tag{4.8}$$

The axial impulse was calculated for each test condition and then an ensemble average of the data was generated with the results presented in Section 4.2. The impulse was smoothed using a 5-point moving window average then the time derivative of the smoothed data was taken using a central differencing scheme. The results of the differentiation for each test condition is shown in Fig. 4.24. These plots show that before the flow separation (at $t = t_2$), the vortical force rises slowly from a near zero value. Upon approaching the first separation point, the vortical force rapidly rises before reaching a maximum value at or near the opening time ($t = t_o$). Afterward, the vortical force declines from the maximum to a lower value. The peak vortical forces was 50-60% of the total peak opening force. This clearly demonstrates that a large portion of the total opening force is directly attributable to the production of vorticity along the canopy surface and the radial expansion of the canopy wake. As was discussed in section 1.4, the vortical force can be increased by moving the vorticity radially outward with time. Therefore, the force the canopy experiences is caused by the rapid movement of vorticity away from the centerline of the canopy while the separation point of the boundary layer moves upstream along the canopy surface. The amount of vorticity in the boundary layer does continue to increase as seen in the increase of the circulation during the inflation. However, the bulk motion of the vorticity away from the canopy centerline is expected to be the primary factor in the increase of the force. Once the boundary is separated from the canopy at the skirt, the vorticity no longer moves rapidly outward from the canopy centerline, so the force decreases as the bulk of the vorticity stabilize at a particular location. The value of the vorticity still might change and its general location might also

move but only in a relatively small sense when compared to the bulk motion of it during the inflation process.

It is expected that this estimate of the vortical force inadequately predicts the actual value. The reason for this is two fold, *i*) it was assumed that the flow was strictly axisymmetric which ignores any three-dimensional effects, and *ii*) the PIV measurements of the velocity fields (and therefore the vorticity fields) was done on a fixed grid resolution which would under-resolve the boundary layer vorticity at the canopy surface. By assuming an axisymmetric flow, any azimuthal variations in the flow around the canopy caused by the three-dimensional effects are disregarded. The axisymmetric assumption is not entirely deficient given that observations of the canopy inflations shows that the flow appears reasonably symmetric across the centerline of the canopy in the measurement plane. The boundary layer of the canopy is confined to a very small region along the canopy surface. In order to properly resolve the boundary layer, it would require the measurements to focus in on a very small portion of the canopy surface which would preclude measuring the near wake region of the canopy and estimating the fluid impulse. However, it is felt that the measurements of the canopy wake performed are a reasonable estimate for the over all behavior of the inflating canopy. If the boundary layer vorticity is under-resolved, this would tend to under predict the fluid impulse and therefore the vortical force as well. The velocity field resolution becomes less problematic with the larger canopy (the 30 cm canopy) since the boundary layer itself is larger. The flow must move along a longer distance across the canopy surface which in turn results in the boundary layer being thicker. The thicker boundary layer is

easier to measure which will result in a better estimate of all flow quantities including the fluid impulse.

The vortical force was normalized to a vortical force coefficient using

$$C_{F_\omega} = \frac{F_\omega}{q_o S_o} \tag{4.9}$$

which is plotted in Fig. 4.25. The solid line in the figure represents the average of all three test conditions. It is clear that under each condition the inflation process follows similar trends. However, there does seem to be considerable scatter between the three conditions for $\tau \geq 1.0$.

The potential force and the vortical force were combined to obtain an estimate of the total aerodynamic force the canopy experiences during the inflation. The combined force estimate is plotted in Figs. 4.26- 4.28 for each test condition. Also plotted in the figures is the individual potential and vortical forces with the total measured force. The combined force estimate exhibits a similar trend to that seen in the measured force. The force gradually rises during the early inflation stage and then transitions into a sharp rise near the opening time. After which the force declines rapidly until it approaches a steady state value. In each case, the combined force estimate predicts approximately 50-60% of the peak opening force. The combined force calculation over-estimates the opening force prior to the opening shock. The combined force estimates made with the smaller canopy tend to over-estimate the breadth of the opening shock as well. While the estimates for the larger canopy match the measured force well in terms of the breadth of the estimate of the opening shock. This is a result of the better resolution of the velocity field measurements for the larger canopy. The other prediction deficiencies are attributable to

the three-dimensional effects and vorticity resolution issues as well as neglecting the other terms in Eq. 1.5 developed in section 1.4 especially the term associated with the internal flow of the canopy.

As seen in the combined force figures, the potential force only plays an important role during the early stages of inflation (up to $\tau \sim 0.5$) when the boundary layer remains attached to the canopy surface. This is not surprising since the wake of the canopy is small at this stage so no large pressure gradient would exist across the canopy to create a larger drag force. Once the boundary layer begins to separate, the wake region directly behind the canopy grows and significantly more vorticity is introduced into the wake near the canopy surface. This would cause the pressure drop across the canopy to increase and therefore increase the drag the canopy experiences. The maximum rate of momentum transfer between the flow and the canopy occurs during the opening shock of the canopy. The flow then separates from the canopy skirt just after the peak opening force and the momentum transfer declines. From this point onward, the canopy approaches the behavior seen for a canopy in a steady flow.

In conclusion, it was shown that the opening force an inflating canopy experiences is primarily caused by the formation of a wake behind the canopy. Traditional methods of modeling the opening force using a combination of an added mass term (*i.e.* the unsteady potential force) and a constant drag coefficient term, to account for the wake effects, are inadequate. The added mass accounts for less than 10% of the peak opening force and only during the early inflation phase, before the opening shock force occurs, does the added mass contribute in a significant amount. Afterwards, the primary force the canopy experiences comes from the formation of the wake. The behavior of the

boundary layer during the inflation is the driving factor in the wake formation. During the early inflation stage, the boundary layer remains attached to the canopy surface resulting in a very small wake. As the canopy grows in size, the boundary layer separates from the canopy with a corresponding growth in the wake. It is during this wake growth interval that the opening shock force occurs. After the opening shock, the boundary layer separates from the canopy skirt and the size of the wake stabilizes resulting in a drag force that settles into values seen for a canopy in steady descent.

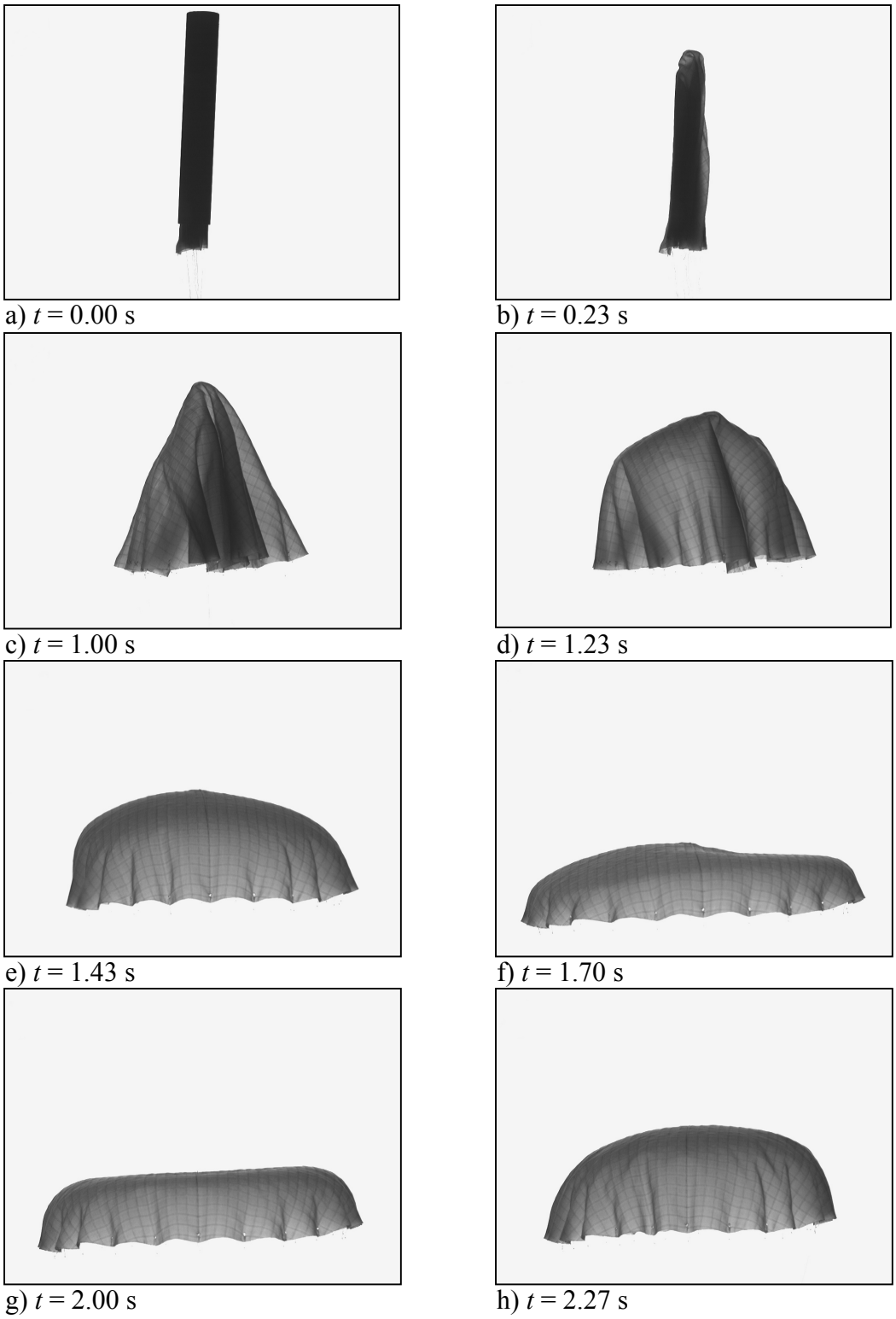

a) t = 0.00 s b) t = 0.23 s

c) t = 1.00 s d) t = 1.23 s

e) t = 1.43 s f) t = 1.70 s

g) t = 2.00 s h) t = 2.27 s

Figure 4.1. Images of a canopy inflation for a 15 cm canopy at a freestream velocity of 20 cm/s. Images correspond with labeled points in Fig. 4.2.

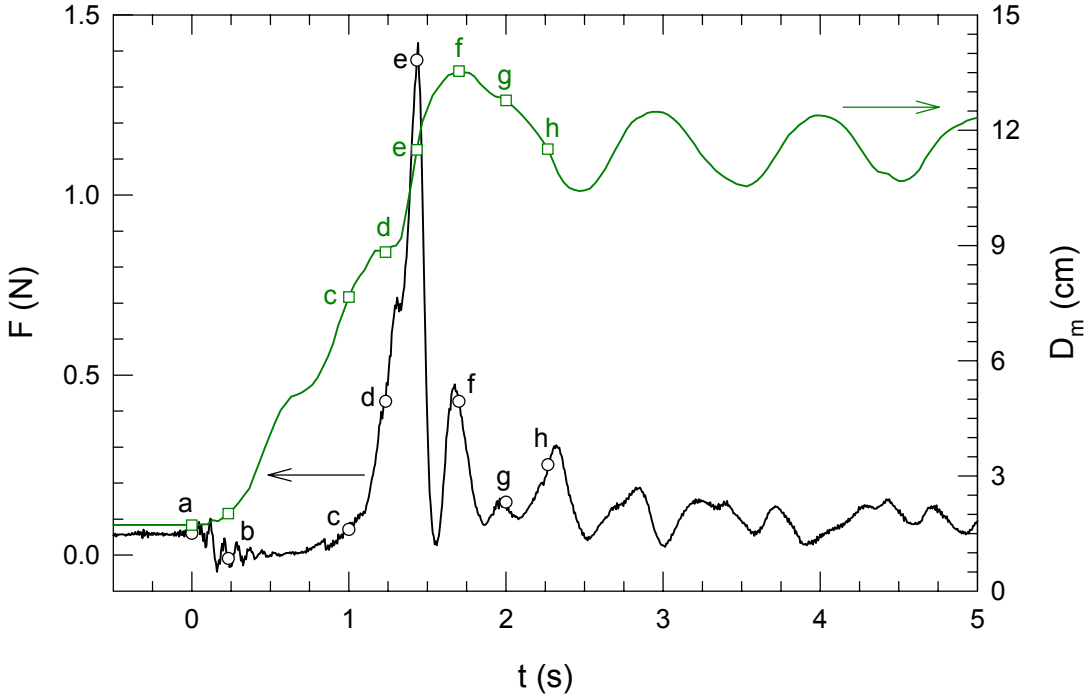

Figure 4.2. The opening force and diameter for a 15 cm canopy at a freestream velocity of 20 cm/s. Labeled points correspond with the images in Fig. 4.1.

a) $t = 0.50$ s
b) $t = 1.50$ s
c) $t = 1.70$ s
d) $t = 2.10$ s
e) $t = 2.40$ s
f) $t = 2.63$ s
g) $t = 3.10$ s
h) $t = 4.10$ s

Figure 4.3. Images of a canopy inflation for a 30 cm canopy at a freestream velocity of 20 cm/s. Images correspond with labeled points in Fig. 4.4.

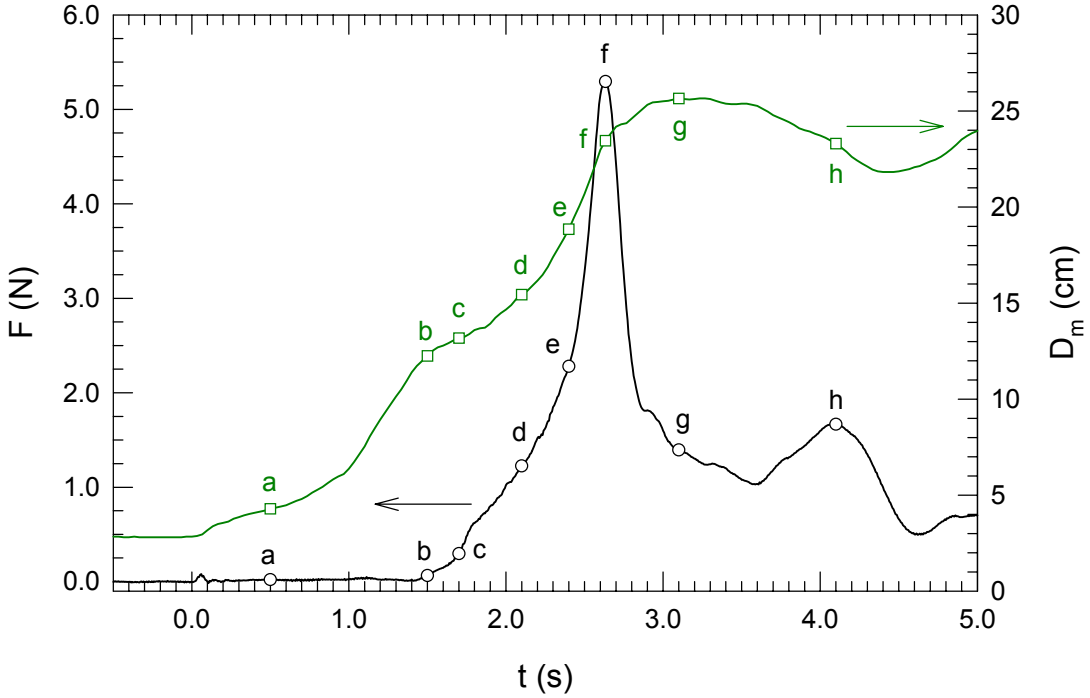

Figure 4.4. The opening force and diameter for a 30 cm canopy at a freestream velocity of 20 cm/s. Labeled points correspond with the images in Fig. 4.3.

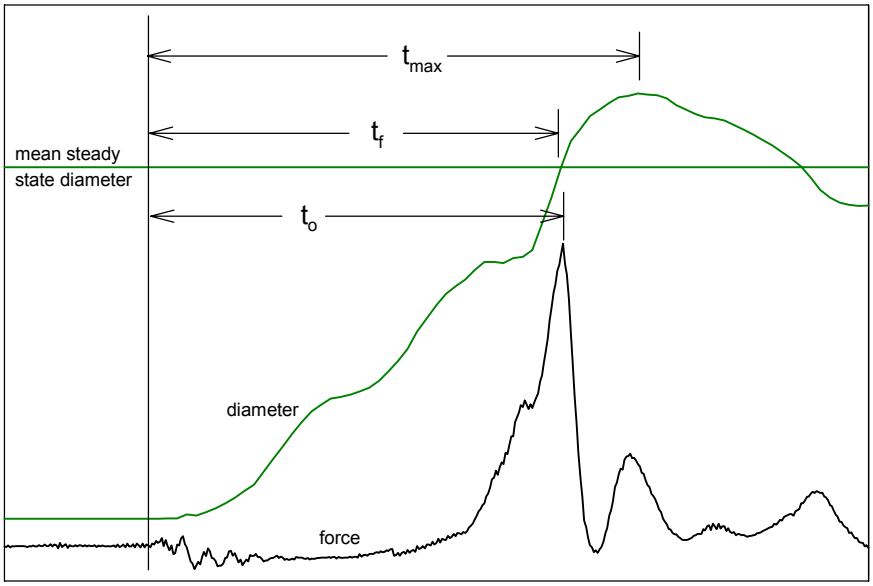

Figure 4.5. Definitions of characteristic times during canopy inflation.

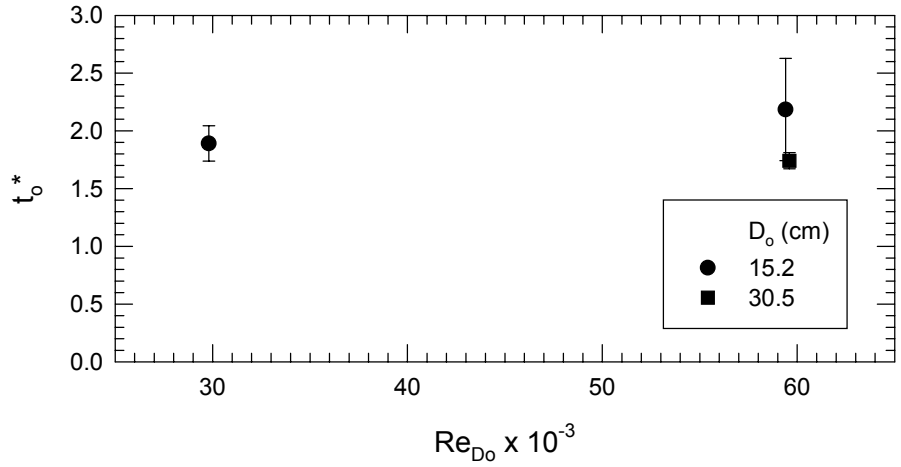

a)

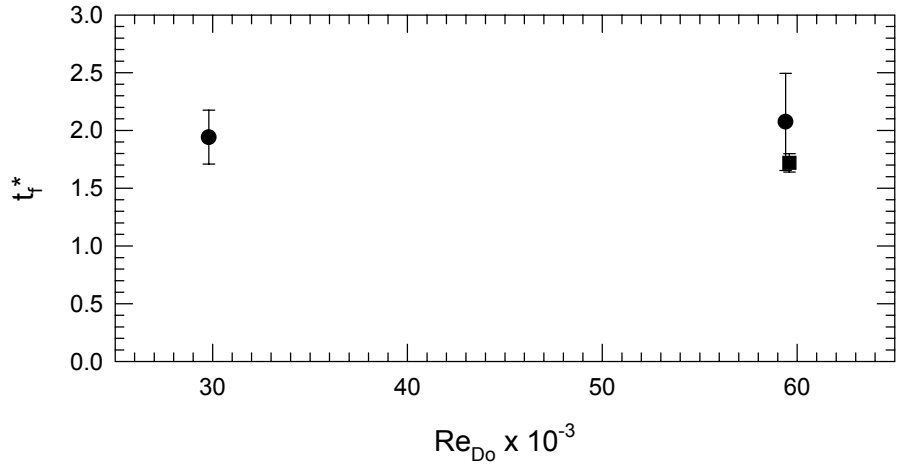

b)

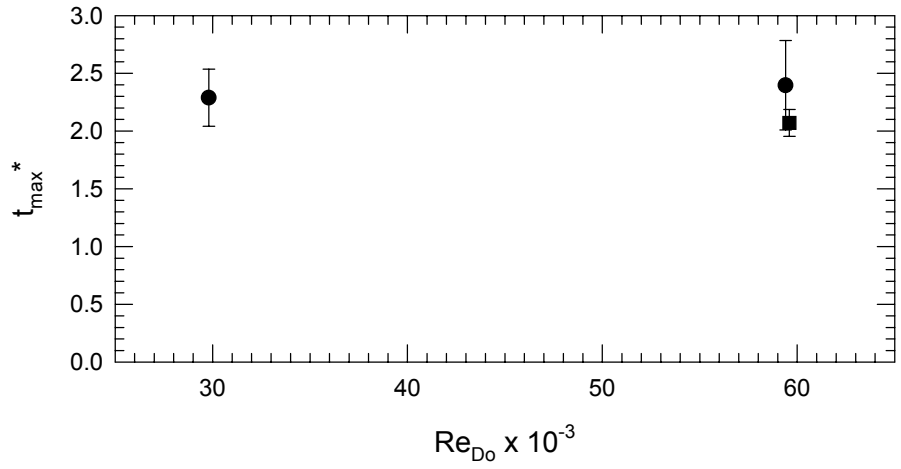

c)

Figure 4.6. Normalized characteristic times; a) opening time, b) filling time, c) maximum diameter time.

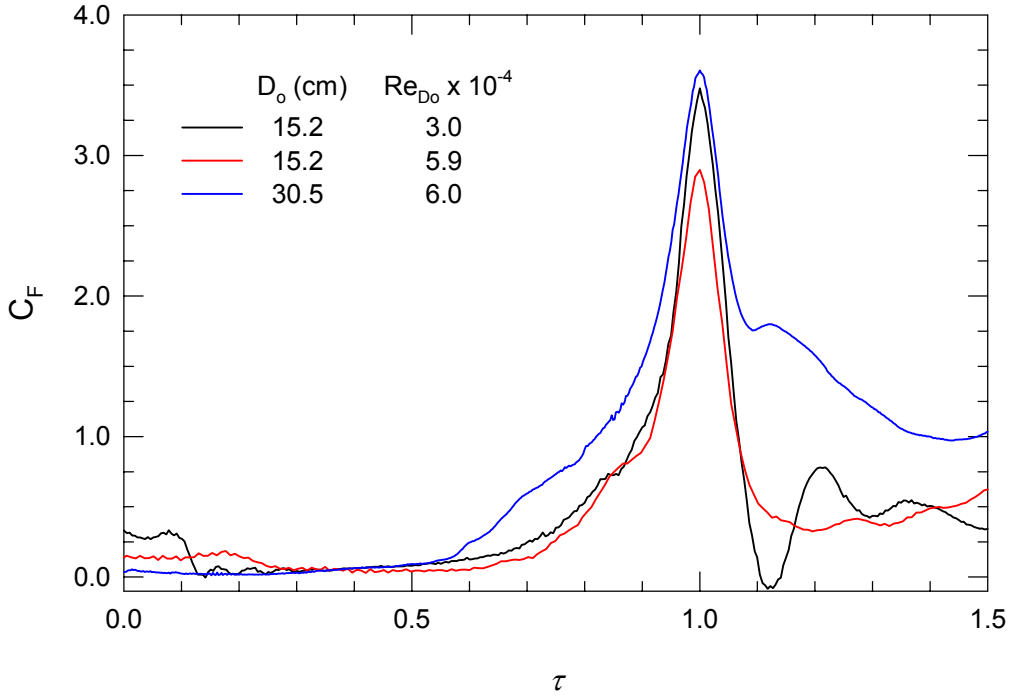

Figure 4.7. Ensemble-averaged force coefficient during canopy inflation of the three cases studied.

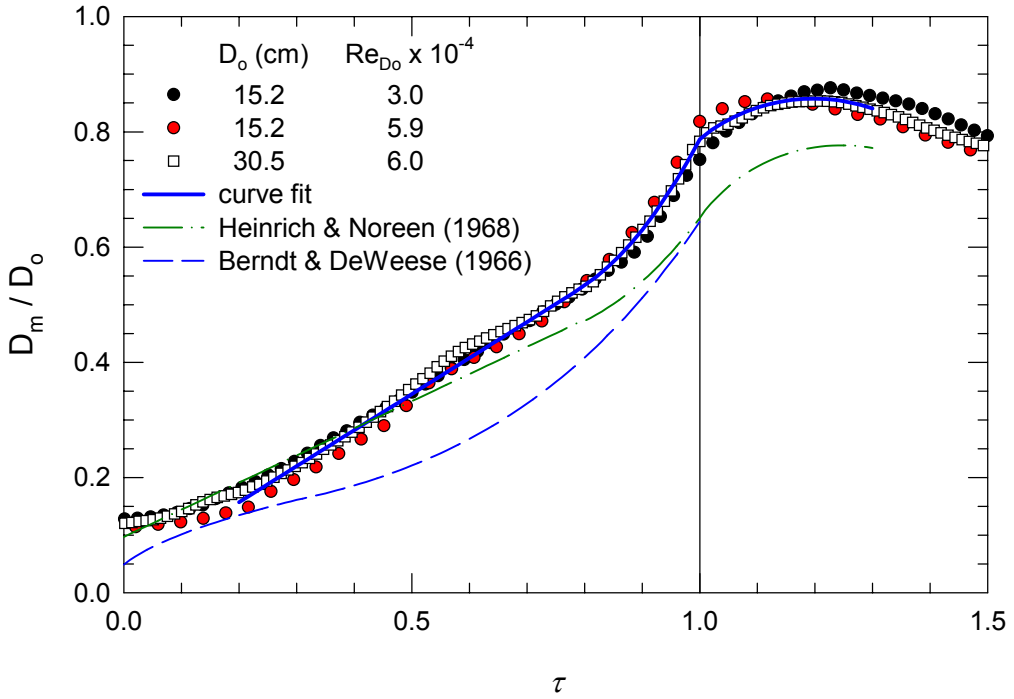

Figure 4.8. Normalized canopy diameter for the three cases studied and several empirical curve fits.

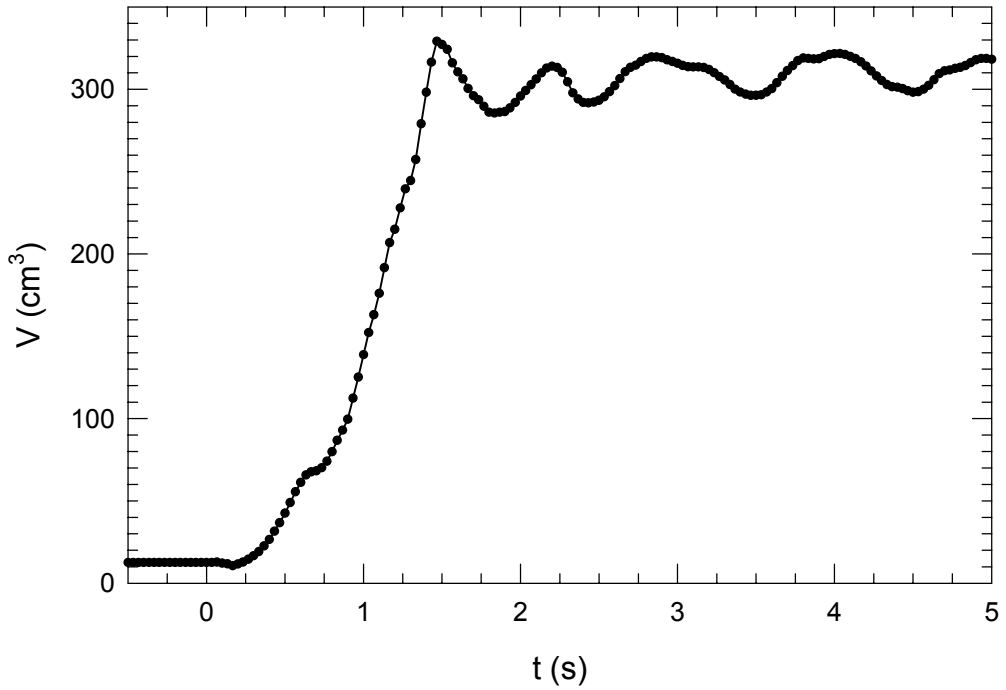

Figure 4.9. A sample of the volume enclosed by an inflating canopy with D_o = 15.2 cm and $Re_{Do} = 3.0 \times 10^4$.

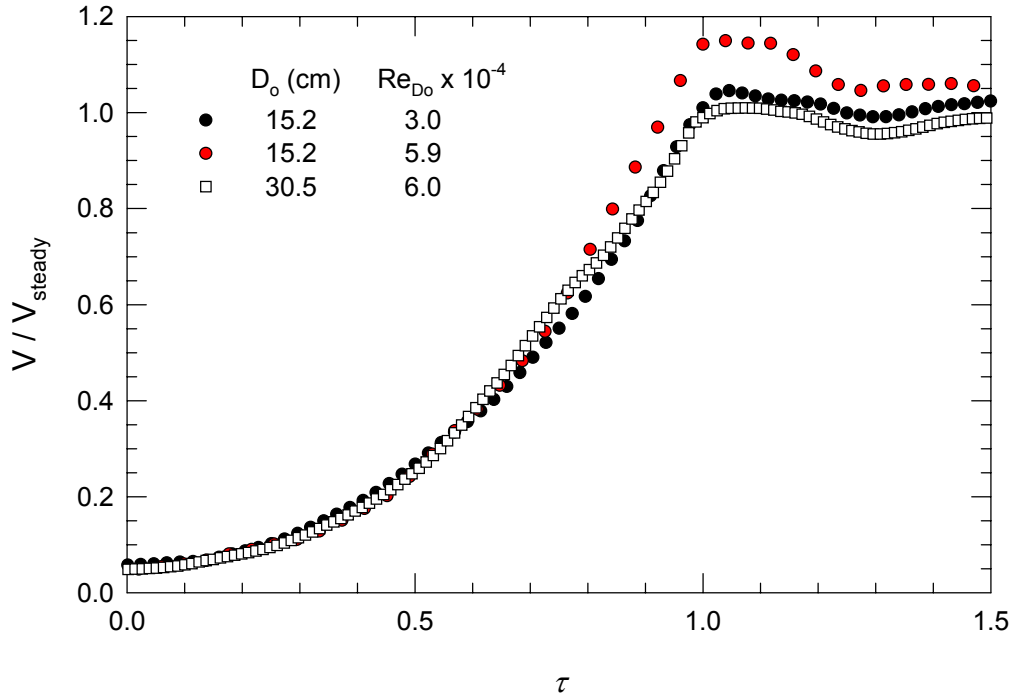

Figure 4.10. Ensemble-averaged enclosed canopy volume for the three cases studied.

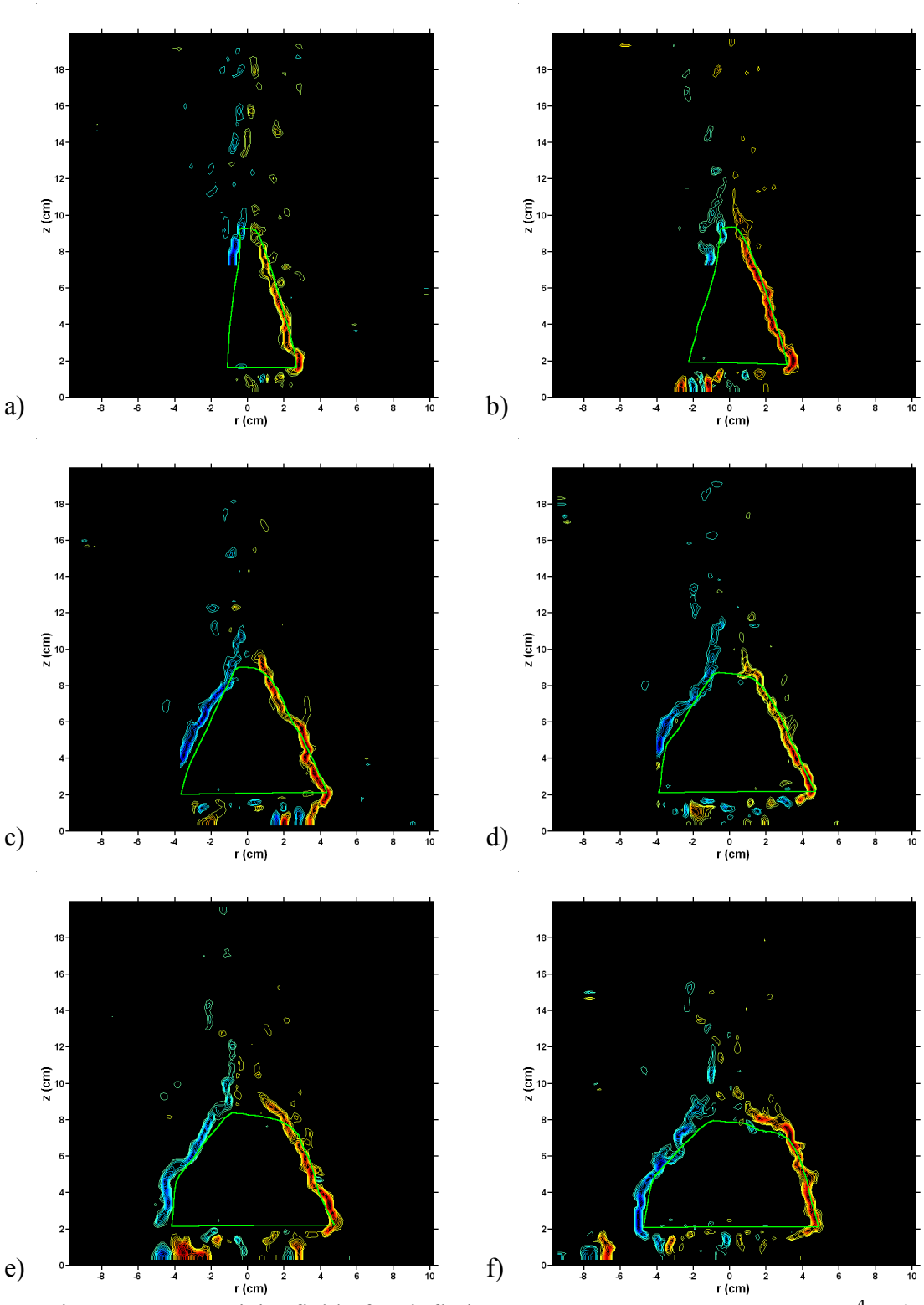

Figure 4.11. Vorticity field of an inflating 15 cm canopy at $Re_{Do} = 3.0 \times 10^4$. The positive vorticity levels are at $\vec{\omega} = 10 - 125$ s^{-1} with steps of 5 s^{-1}. The time for each image is a) $t = 0.40$ s, b) $t = 0.73$ s, c) $t = 0.93$ s, d) $t = 1.00$ s, e) $t = 1.07$ s, and f) $t = 1.13$ s. Stage II inflation ($t_2 = 1.10$ s) begins between images e and f.

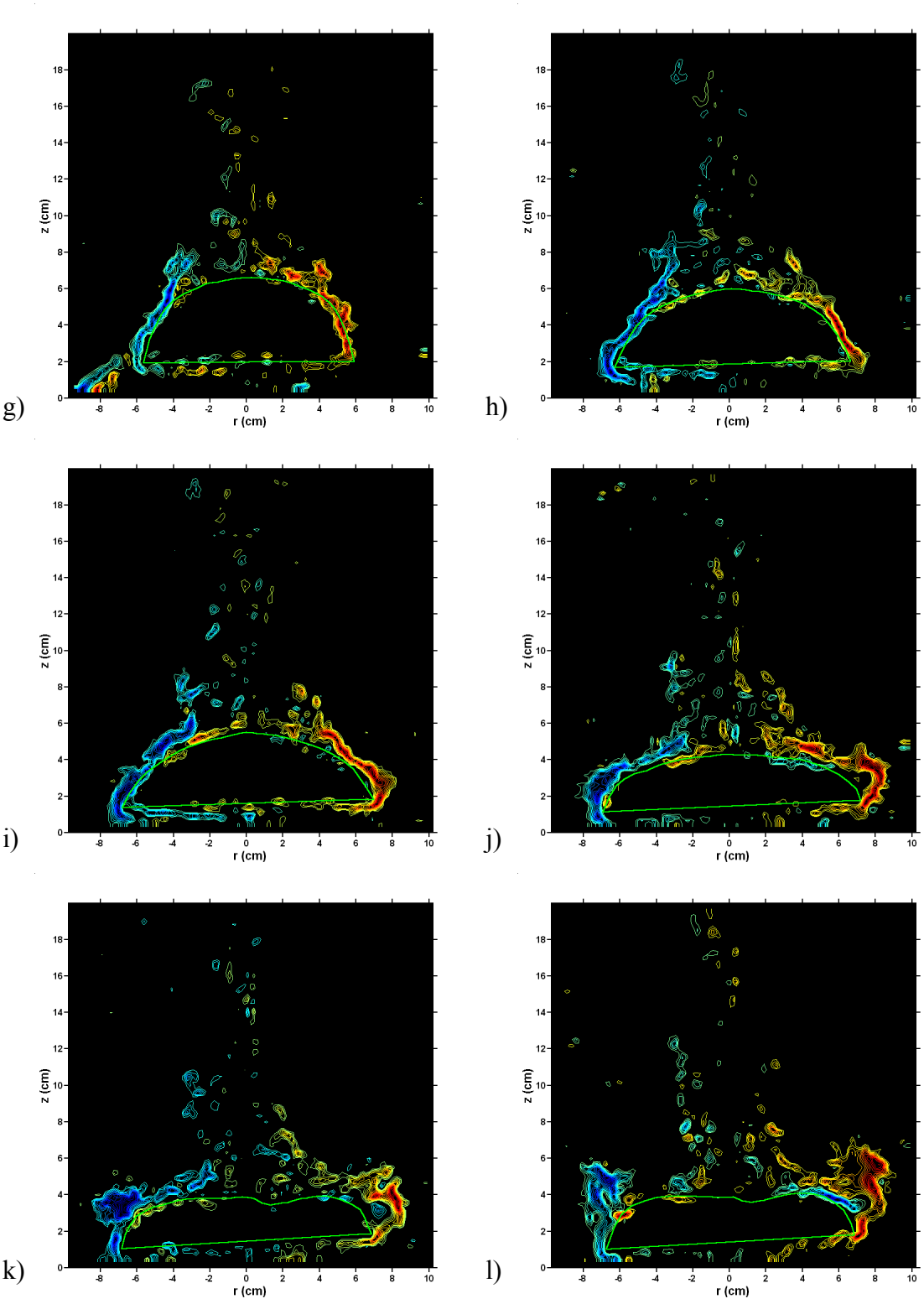

Figure 4.11, continued. The time for each image is g) $t = t_f = 1.27$ s, h) $t = t_o = 1.33$ s, i) $t = t_3 = 1.40$ s, j) $t = t_{max} = 1.53$ s, k) $t = 1.67$ s, and l) $t = 1.80$ s.

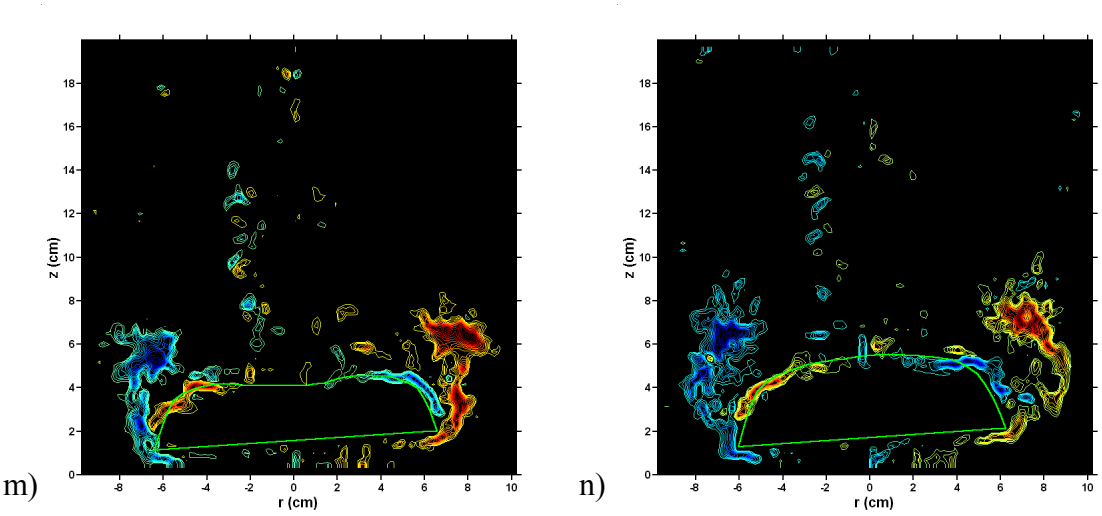

Figure 4.11, continued. The time for each image is m) t = 1.93 s and n) t = 2.07 s.

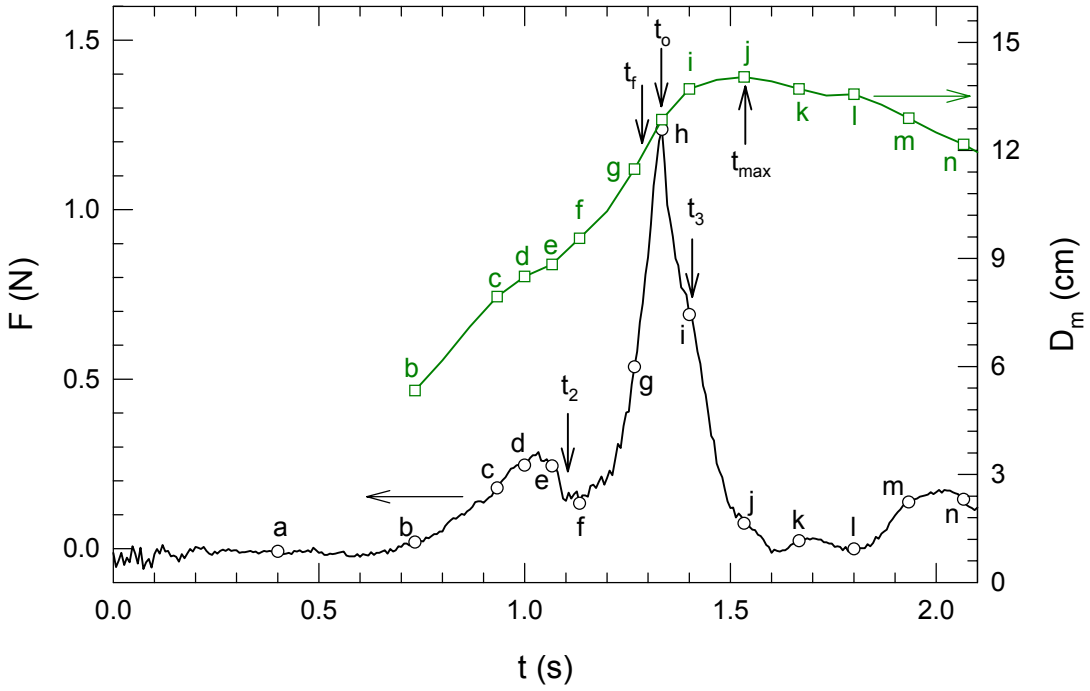

Figure 4.12. Force and diameter of canopy shown in Fig. 4.11. The letters correspond to the individual images in Fig. 4.11.

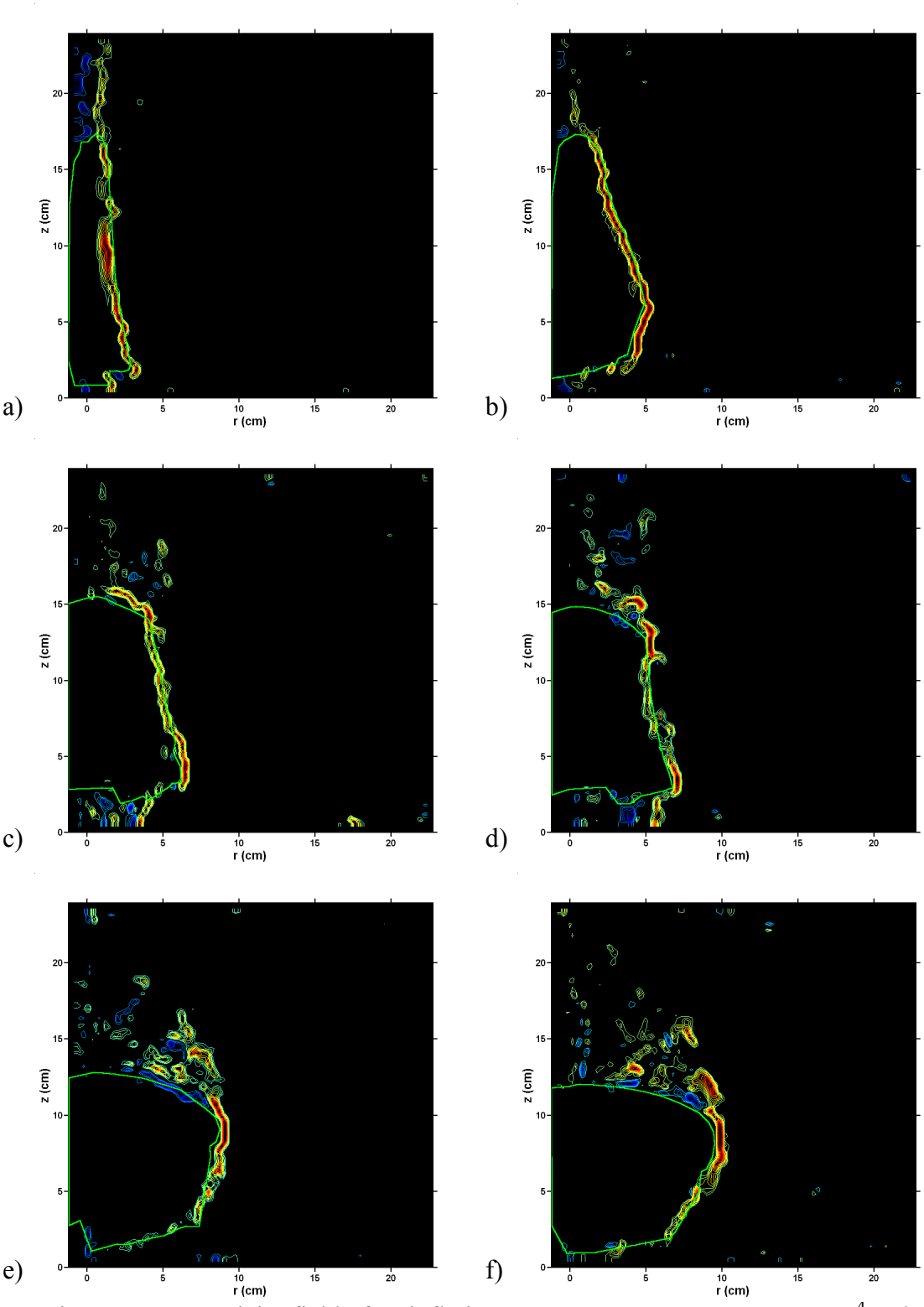

Figure 4.13. Vorticity field of an inflating 30 cm canopy at $Re_{Do} = 6.0 \times 10^4$. The positive vorticity levels are at $\vec{\omega} = 10 - 125$ s^{-1} with steps of 5 s^{-1}. The time for each image is a) $t = 0.40$ s, b) $t = 1.40$ s, c) $t = 2.13$ s, d) $t = t_2 = 2.27$ s, e) $t = 2.80$ s, and f) $t = 3.00$ s.

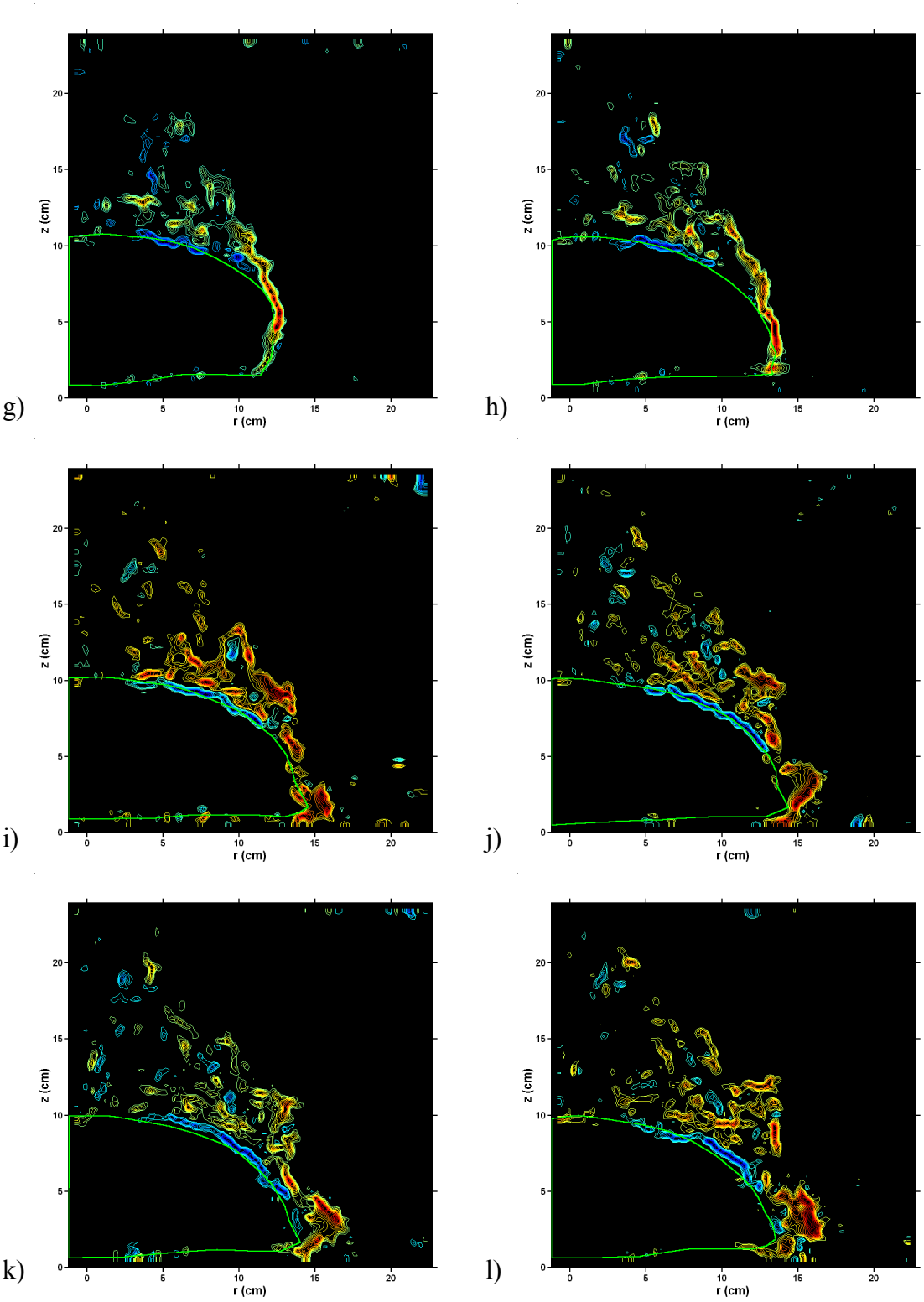

Figure 4.13, continued. The time for each image is g) $t = 3.33$ s, h) $t = 3.40$ s, i) $t = 3.53$ s, j) $t = 3.60$ s, k) $t = t_3 = 3.67$ s, and l) $t = t_{max} = 3.73$ s. The filling time ($t_f = 3.36$ s) occurs between images g and h. The opening time ($t_o = 3.55$ s) occurs between images i and j.

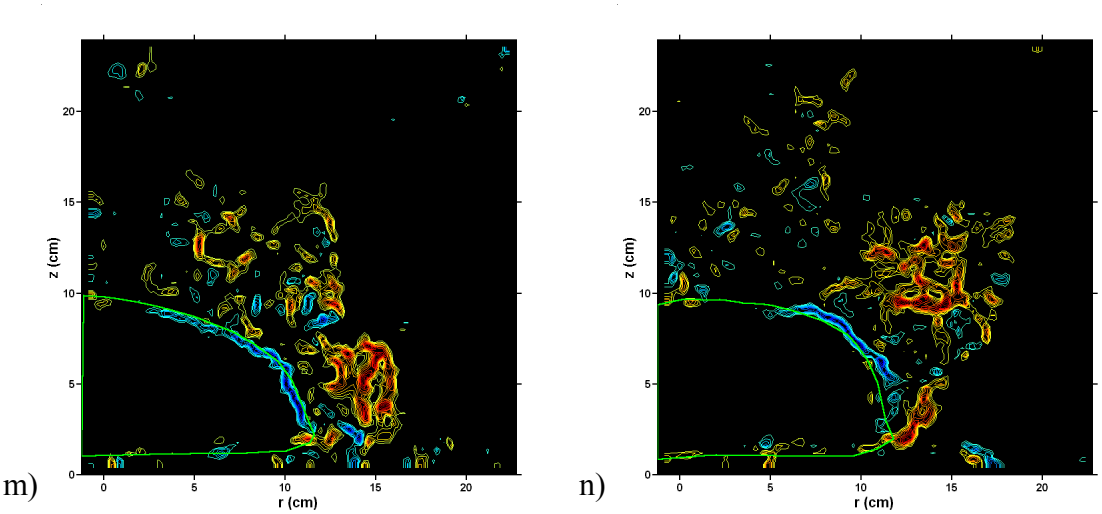

Figure 4.13, continued. The time for each image is m) $t = 4.00$ s and n) $t = 4.60$ s.

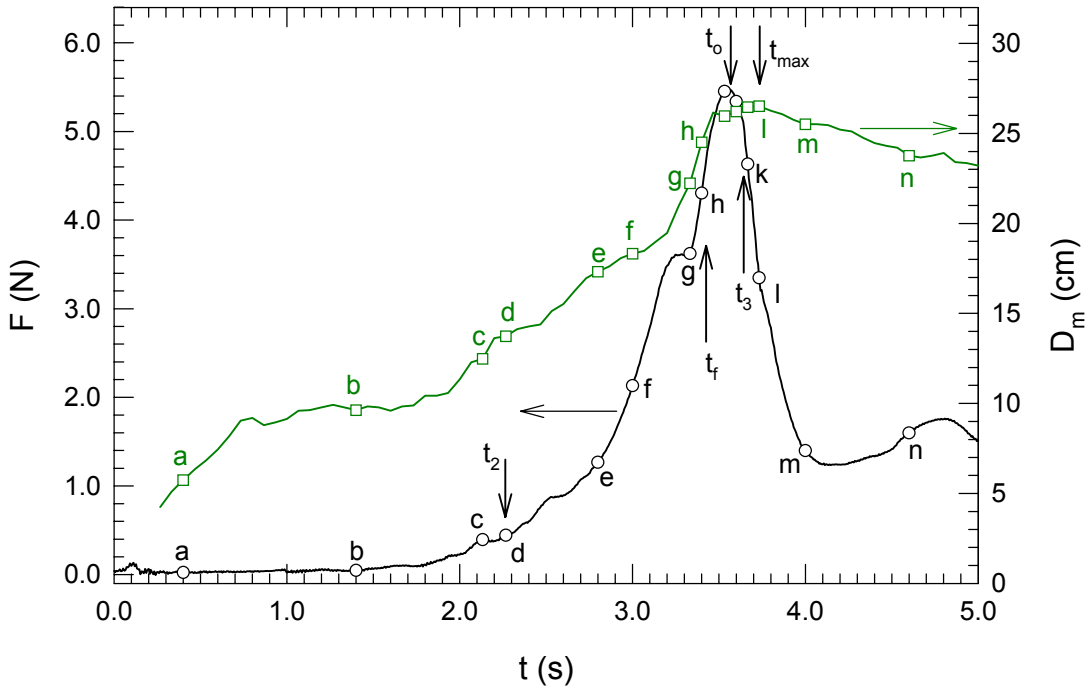

Figure 4.14. Force and diameter of canopy shown in Fig. 4.13. The letters correspond to the individual images in Fig. 4.13.

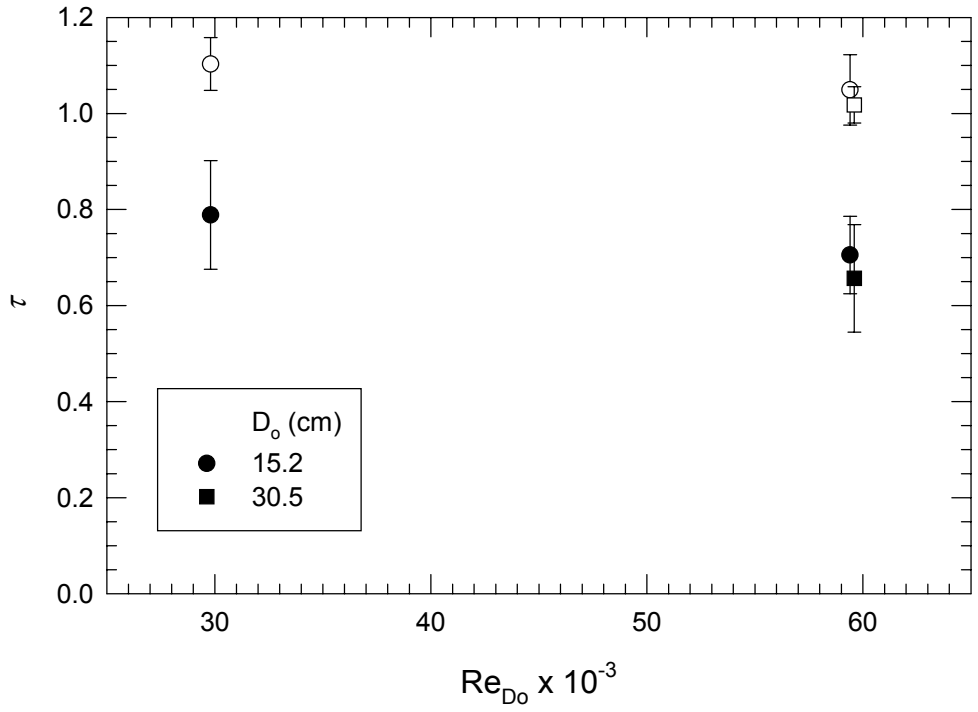

Figure 4.15. Normalized separation times. The solid symbols represent the stage II inflation time, τ_2, and the open symbols represent the stage III inflation time, τ_3.

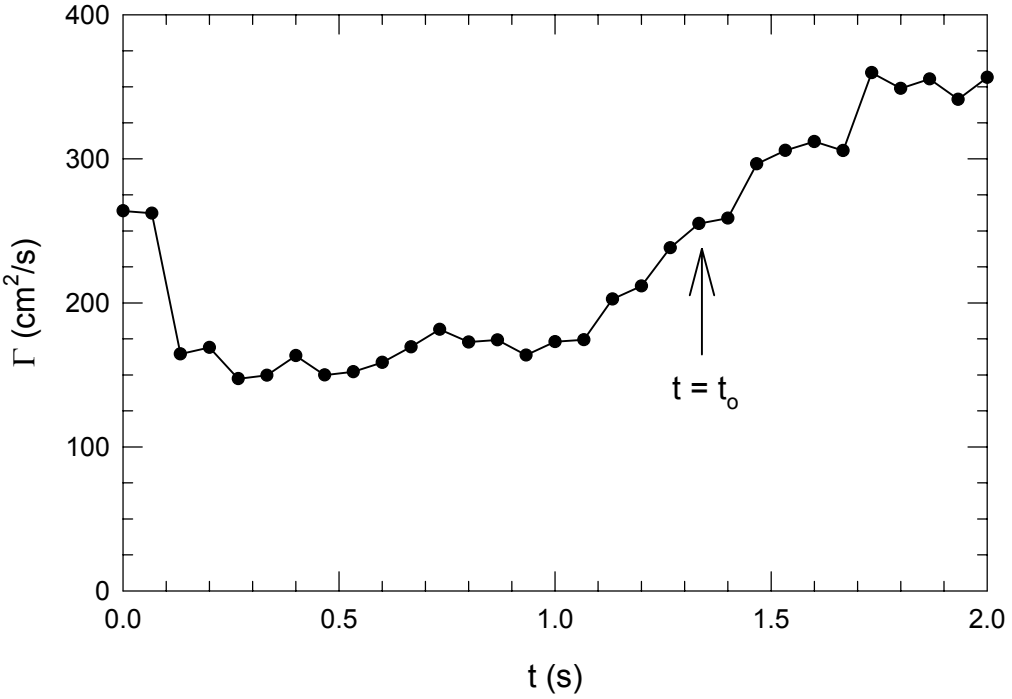

Figure 4.16. A sample of the circulation 15 cm canopy at $Re_{Do} = 3.0 \times 10^4$.

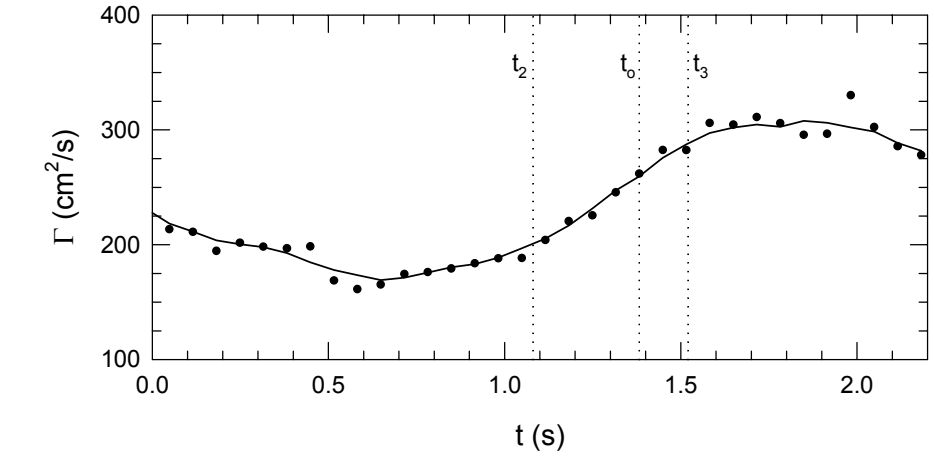

a)

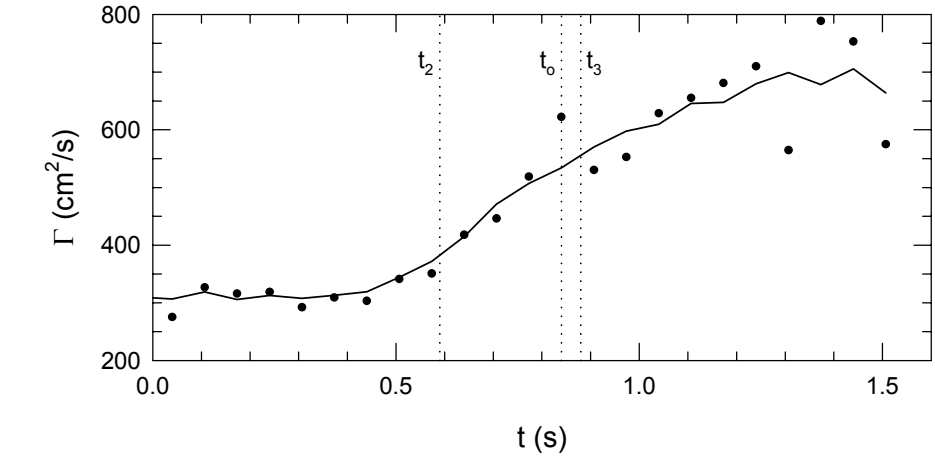

b)

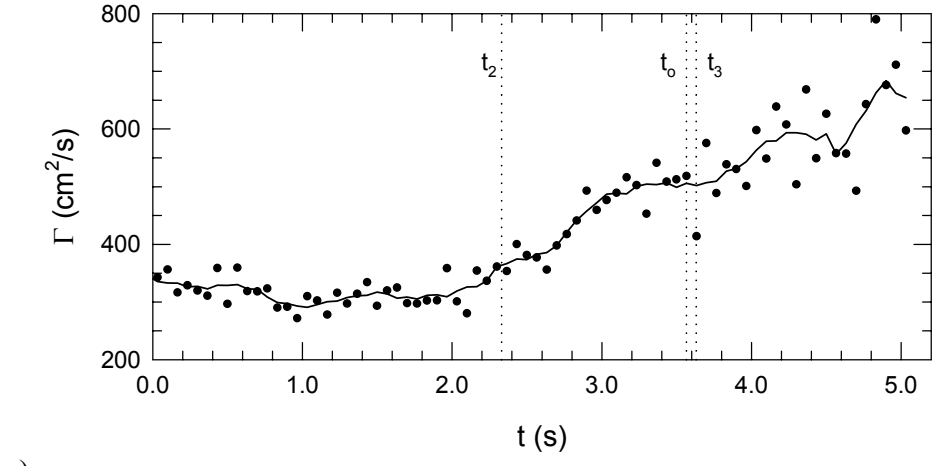

c)

Figure 4.17. Average circulation of the canopy wake, a) 15 cm canopy at $Re_{Do} = 3.0 \times 10^4$; b) 15 cm canopy at $Re_{Do} = 5.9 \times 10^4$; c) 30 cm canopy at $Re_{Do} = 6.0 \times 10^4$. The solid line is a 5-point moving window average of the data and the vertical dotted lines are the noted times.

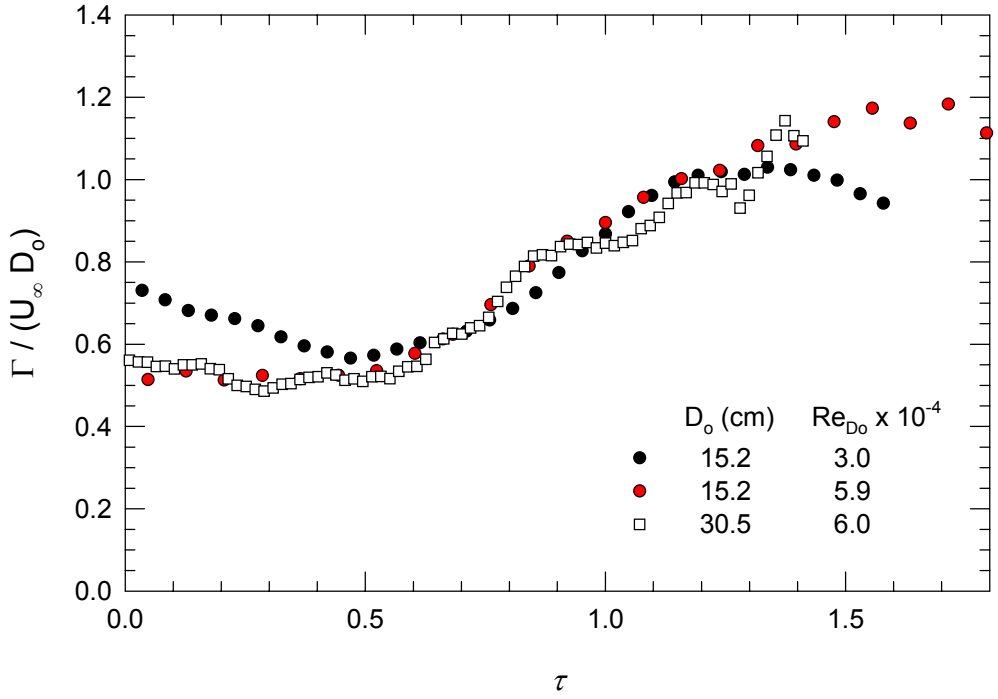

Figure 4.18. Normalized average circulation.

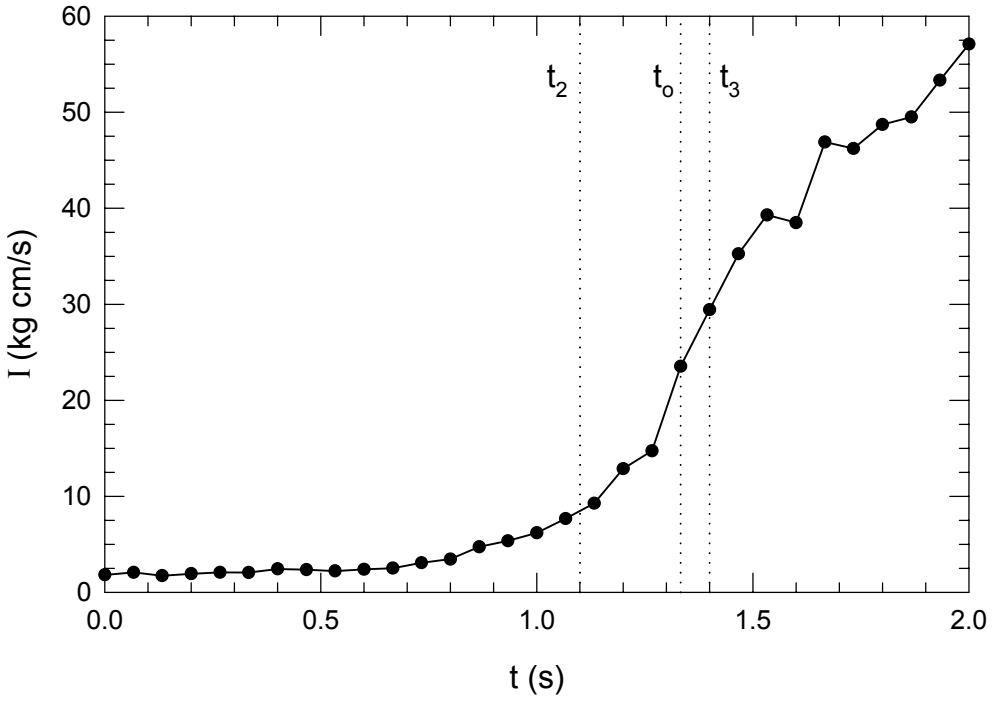

Figure 4.19. A sample of the impulse for a 15 cm canopy at $Re_{Do} = 3.0 \times 10^4$.

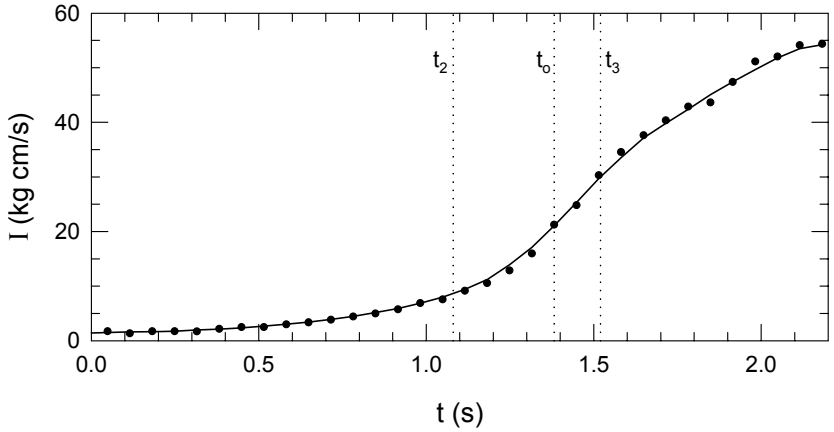

a)

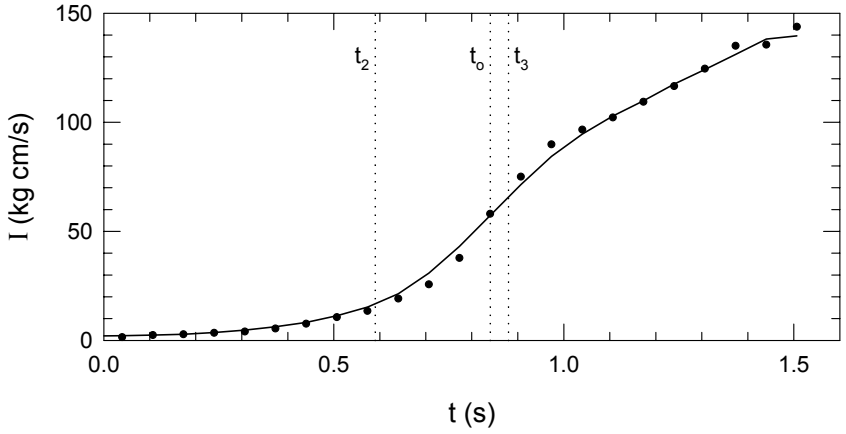

b)

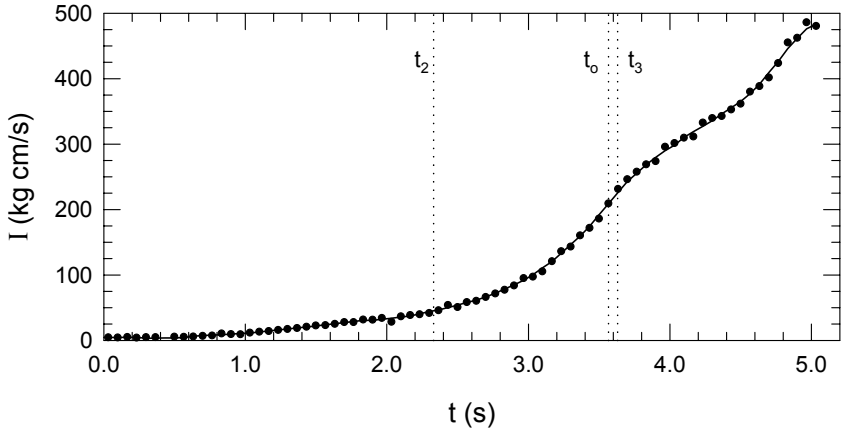

c)

Figure 4.20. Average impulse of the canopy wake, a) 15 cm canopy at $Re_{Do} = 3.0 \times 10^4$; b) 15 cm canopy at $Re_{Do} = 5.9 \times 10^4$; c) 30 cm canopy at $Re_{Do} = 6.0 \times 10^4$. The solid line is a 5-point moving window average of the data and the vertical dotted lines are the noted times.

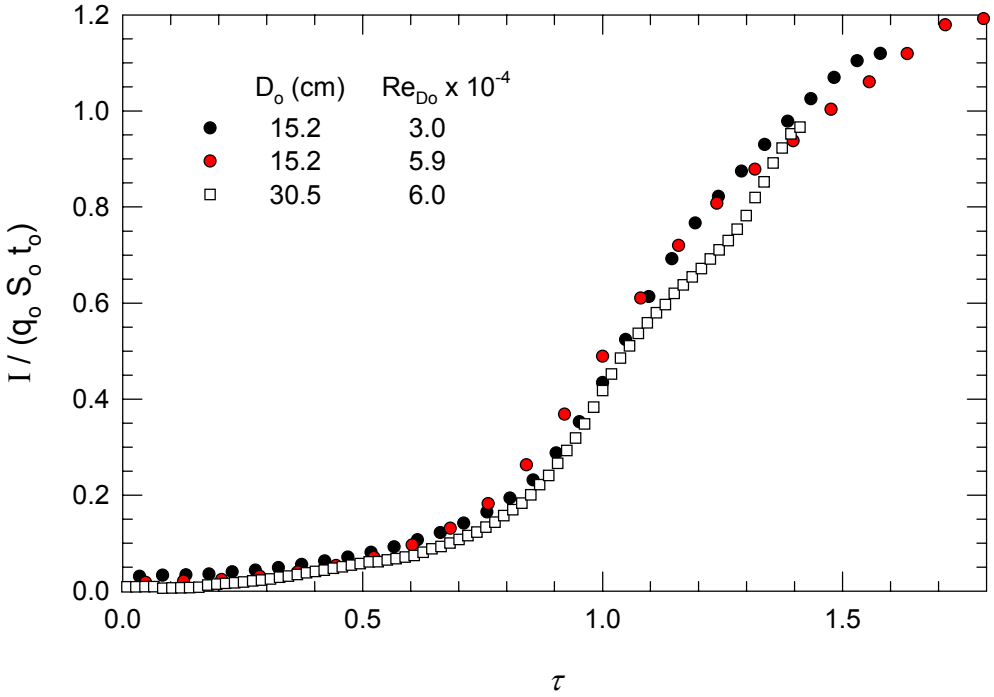

Figure 4.21. Normalized average impulse.

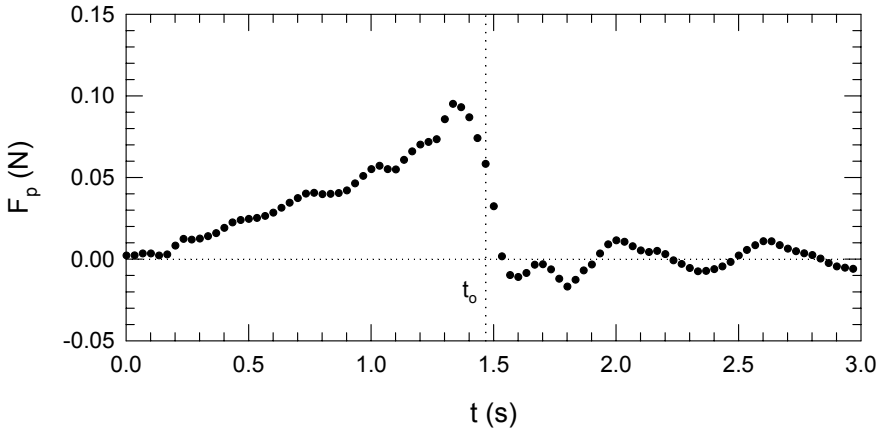

a)

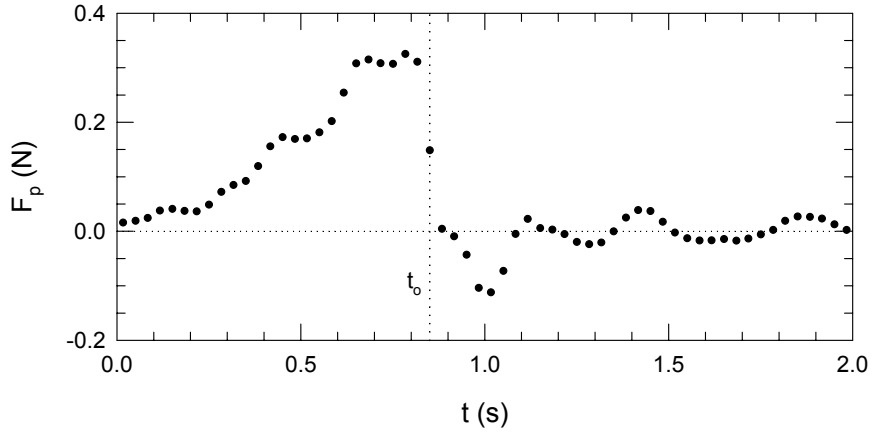

b)

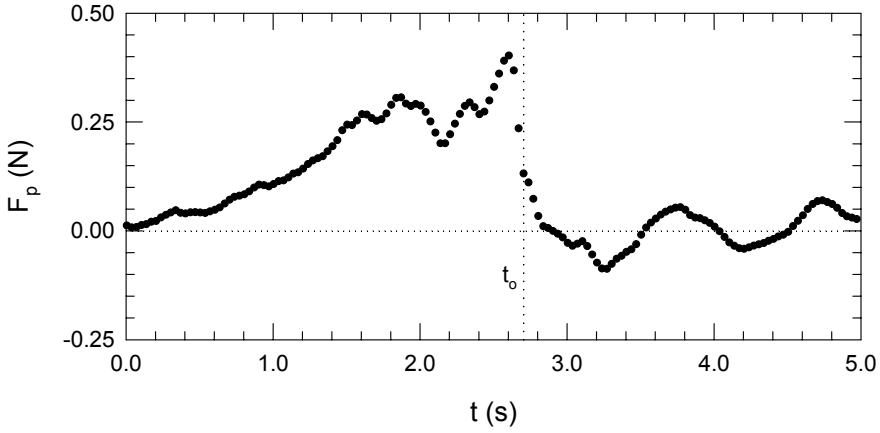

c)

Figure 4.22. Average unsteady potential force, a) 15 cm canopy at $Re_{Do} = 3.0 \times 10^4$; b) 15 cm canopy at $Re_{Do} = 5.9 \times 10^4$; c) 30 cm canopy at $Re_{Do} = 6.0 \times 10^4$.

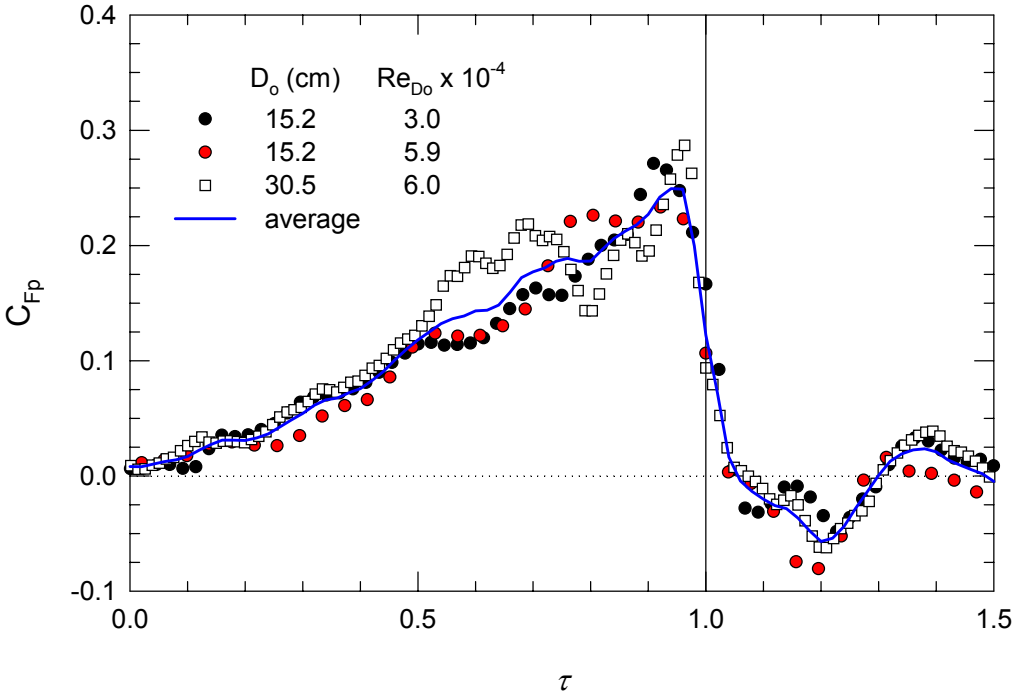

Figure 4.23. Unsteady potential force coefficient.

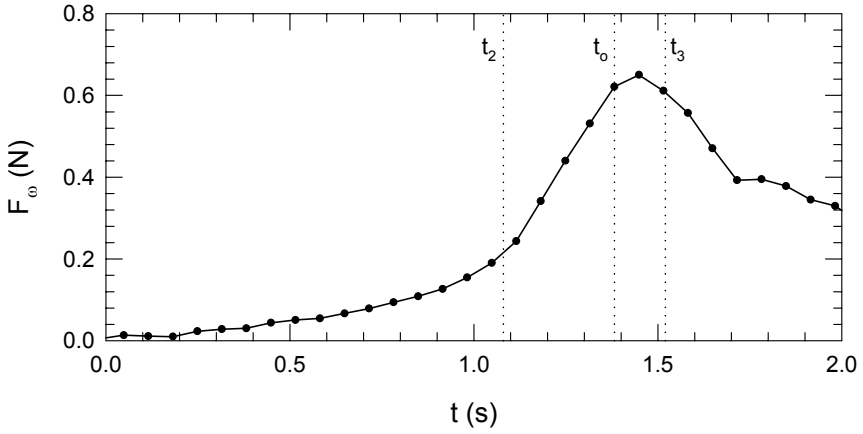

a)

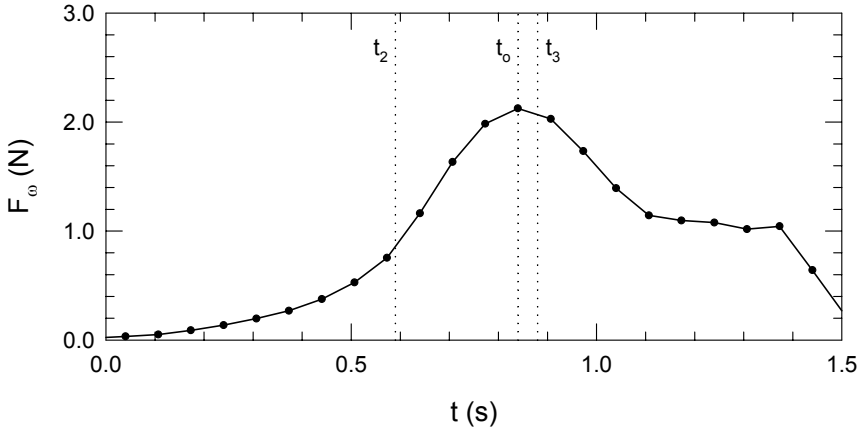

b)

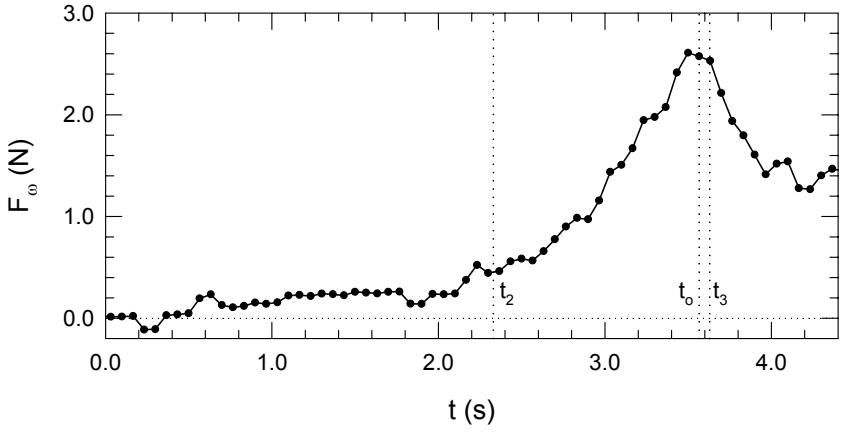

c)

Figure 4.24. Average force due to wake vorticity, a) 15 cm canopy at $Re_{Do} = 3.0 \times 10^4$; b) 15 cm canopy at $Re_{Do} = 5.9 \times 10^4$; c) 30 cm canopy at $Re_{Do} = 6.0 \times 10^4$.

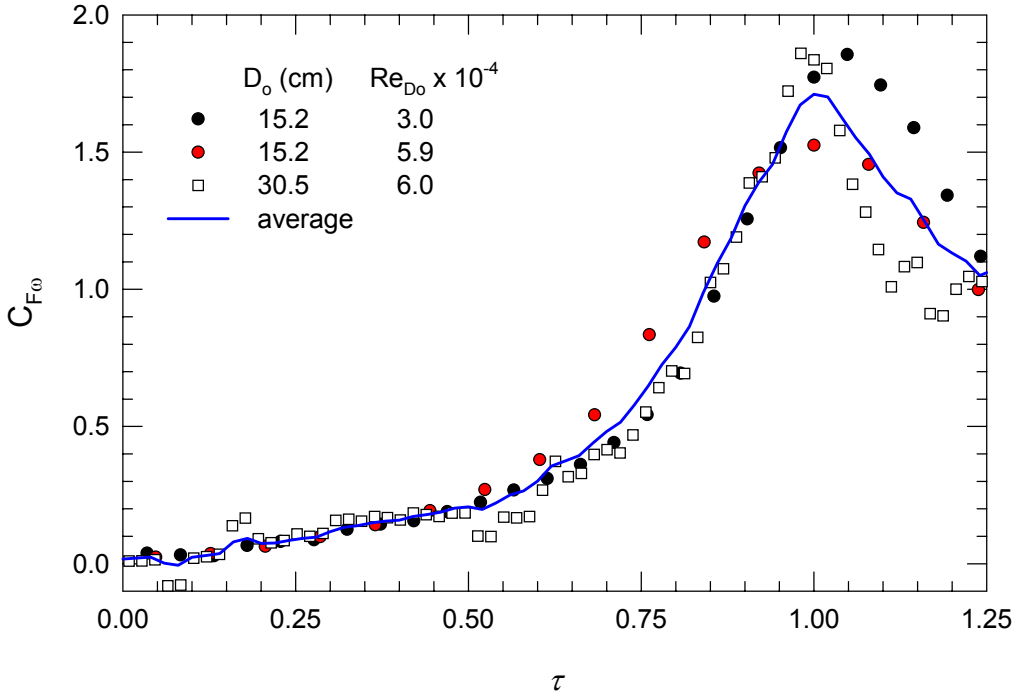

Figure 4.25. Force coefficient due to the impulse in the canopy wake.

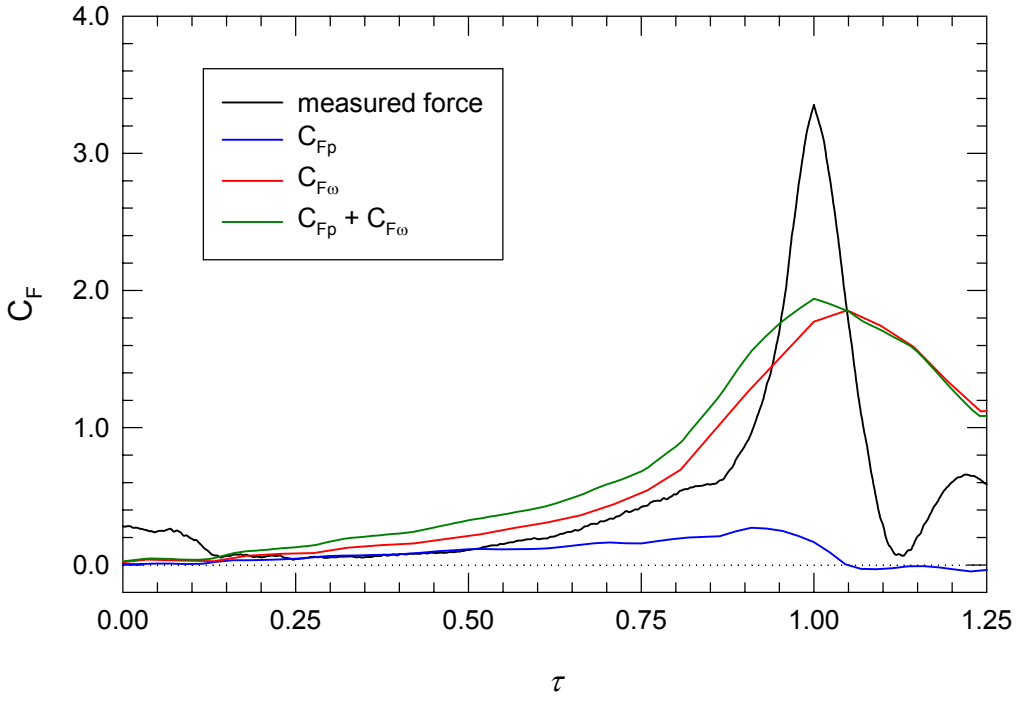

Figure 4.26. Force coefficient estimates from the summation of the unsteady potential force and the force due to the vorticity in the wake for a 15 cm canopy at $Re_{Do} = 3.0 \times 10^4$.

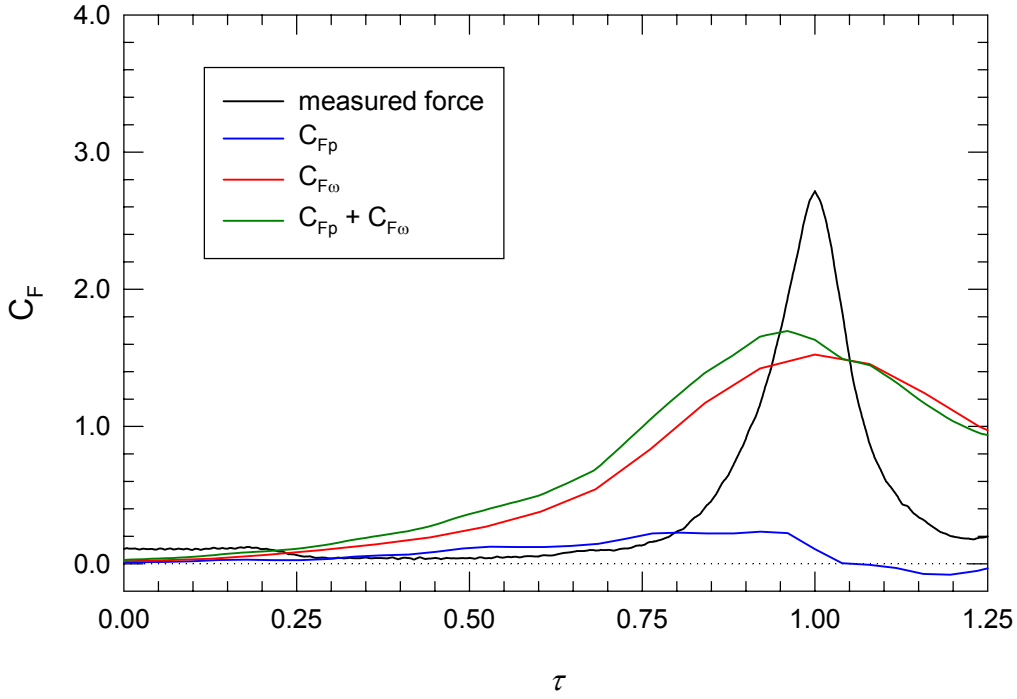

Figure 4.27. Force coefficient estimates from the summation of the unsteady potential force and the force due to the vorticity in the wake for a 15 cm canopy at $Re_{Do} = 5.9 \times 10^4$.

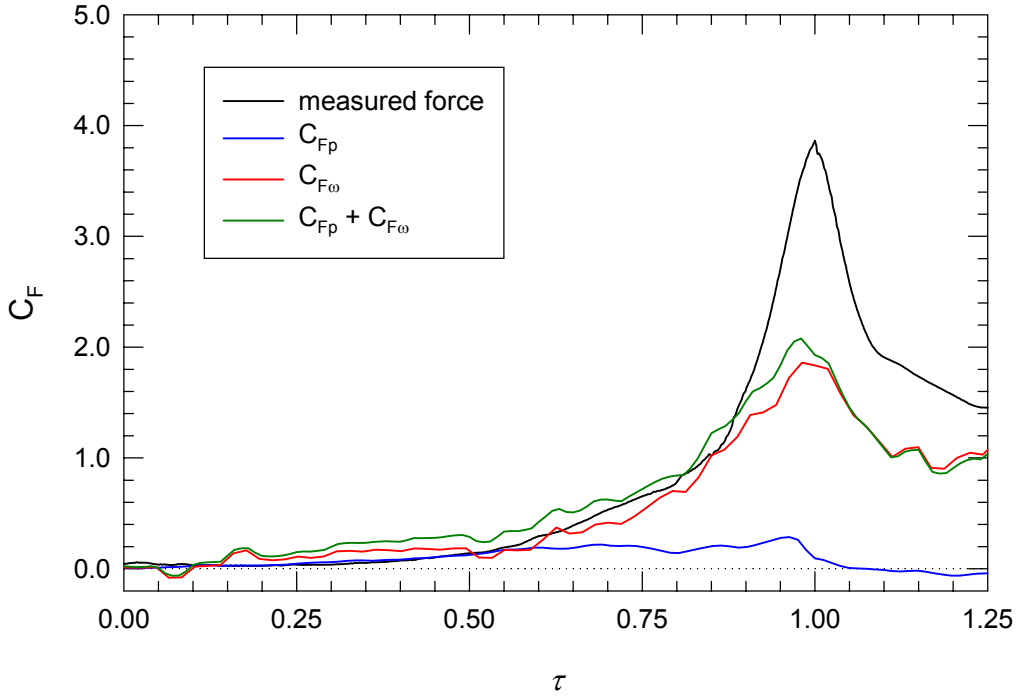

Figure 4.28. Force coefficient estimates from the summation of the unsteady potential force and the force due to the vorticity in the wake for a 30 cm canopy at $Re_{Do} = 6.0 \times 10^4$.

5. Conclusions

The flow field in the wake of a small scale flexible generic round parachute canopy was investigated. The research focused on the inflation of a canopy in a constant freestream velocity under an infinite mass condition and a fully inflated canopy. The canopy wake was measured by the PIV method in a two-dimensional plane that was parallel to the freestream. The vorticity field was computed from the velocity field measurements. Simultaneous measurements of the drag force and the overall canopy geometry allowed for the correlation between the canopy dynamics and the near wake flow field.

The experiments were performed in a water tunnel to allow for longer canopy inflation times than would be present in a wind tunnel. The effects of Reynolds number and canopy size were examined by testing at three freestream velocities, which ranged from a nominal 20 cm/s to 40 cm/s, and selecting two different canopy diameters (15.2 cm and 30.5 cm). The Reynolds number ranged from $3.0 - 6.0 \times 10^4$. A qualitative assessment of the overall canopy dynamics of the small scale canopies showed characteristics similar to those seen in full scale canopies (with the possible exception of the canopy behavior during the early stages of inflation). These characteristics included a cyclic breathing of the canopy diameter for a fully inflated canopy, a large opening shock during the canopy inflation, and the over-expansion of the canopy diameter during the inflation process. The geometric characteristics of the model in the early stage of the inflation process showed a marked difference with a full scale inflation, a result of the higher stiffness of the canopy models.

Analysis of the shedding characteristics of the fully inflated canopy in a constant freestream flow identified the source of the canopy "breathing" cycle. The cyclic expansion and contraction of the diameter of a flexible parachute canopy corresponds to the shedding of successive vortex rings into the wake. This "breathing" motion corresponded to a normalized breathing frequency of 0.56 ± 0.03. A similar vortex shedding frequency was found to exist that remained at a constant Strouhal number of 0.54 ± 0.04 over the studied Reynolds number range. The normalized shedding frequency was confirmed by two methods, namely by *i.*) spectral analysis of the radial velocity field in the near wake, and *ii.*) by tracking the position of the shed vortices in the wake. This shedding frequency has not been reported in past studies of disks or spheres. The non-rigid nature of the canopy structure may lend to the formation of this shedding frequency. It was also observed that the vortex rings form symmetrically around the canopy at lower Reynolds numbers, and the formation becomes asymmetric with the vortex rings becoming twisted and distorted immediately as the Reynolds number approaches 6.0×10^4, the limit of our experiments.

Examination of the flow field surrounding the inflating canopy revealed that the kinematics of the flow field is an important element of the canopy inflation process. During the early stages of the inflation, the boundary layer on the canopy surface remains attached to the canopy material and the wake of the canopy has minimal extent. This results in the canopy only experiencing a small amount of force from the fluid even though the canopy diameter has grown a substantial amount. Once the curvature of the canopy can no longer support an attached boundary layer, it begins to separate from the canopy surface near the apex region and the wake of the canopy increases in size with a

corresponding increase in the force. At this point the force rapidly increases to its maximum value as the separation point of the boundary layer moves upstream from the canopy apex region towards the canopy skirt. The force then plunges precipitously to levels seen for a fully inflated canopy in a steady flow. Once the boundary layer becomes separated from the canopy at the skirt, it commences to roll-up into a large vortex ring (termed the unloading vortex) near the outer edges of the canopy. The canopy diameter is drawn out to its over-expanded state at this point and then proceeds to the cyclic breathing seen in a steady state canopy. The unloading vortex is eventually shed from the canopy and is convected downstream where it begins to form the wake of the steady state canopy.

The force the canopy experiences from the fluid was estimated from an unsteady potential flow force and a force associated with the rate of change of the fluid impulse. For a canopy in a constant freestream (*i.e.* the canopy does not decelerate) the unsteady potential flow force can be estimated from the rate of change of the volume enclosed by the canopy. While the fluid impulse is a consequence of the vorticity containing portions of the flow. It was shown that the unsteady potential force contributed to no more than 10% of the total peak opening force and only provided a significant portion of the opening force during the early stages of the inflation process. It should also be noted that the *rms*-value of the fluctuating unsteady potential force of the fully inflated canopy is less than 10% of the total drag force and 20% of the *rms*-value of the force. A large portion of the total opening force was the result of the time rate of change of the fluid impulse. The formation of the wake behind the canopy during inflation results in the production of vorticity, and the bulk displacement of this vorticity in the flow causes the

large opening shock force. Once the large amplitude displacement of the vorticity stops, the force approaches levels seen for a canopy in a steady flow (*i.e.* steady descent).

These conclusions show that the temporal evolution of the inflation process should not be exclusively modeled with just an apparent mass term. Consideration of the temporal evolution of the vorticity generated during the inflation needs to be included in the modeling efforts. Also the data and knowledge obtained from this research should aid in the validation of the computational models now being developed.

6. Recommendations for Future Research

Flow field measurements in the near wake of a canopy, in a finite mass condition, should be performed in order to examine and understand the flow physics of a decelerating canopy. It is known that during a finite mass inflation, the peak opening force occurs before the canopy is fully inflated (at the filling time). The question arises, how does this flow field differ from that seen in an infinite mass inflation? It is expected that the when the boundary layer separates from the canopy, the force will rapidly increase forming the opening shock; similar to what is seen in the infinite mass case. However, in the finite mass case, the boundary layer is expected to separate sooner in the inflation process than that seen in the infinite mass case. This would result in the opening shock occurring earlier in the inflation process. However to verify this hypothesis, it is necessary to measure and study the flow field around a canopy inflating in a decelerating flow.

The apparent and included masses of a canopy (under a finite mass condition) should be estimated from measurements of the enclosed canopy volume and the deceleration of the freestream velocity. Based on these estimates, the unsteady potential flow forces could be calculated and compared with estimates of the force associated with the rate of change of the fluid impulse. This would show how the unsteady potential flow force contributes to the total force the canopy experiences from the fluid. It is also desirable to obtain higher spatial and temporal resolution of the velocity field in order to obtain a better estimate of the fluid impulse and how it changes with time. It would also be beneficial to measure the flow field in the interior of the canopy to obtain improved estimates of the force exerted on the canopy by the fluid.

In addition, experiments with the same level of detail should be performed at higher Reynolds numbers. This way the flow field would be examined over a larger Reynolds number range and it can be seen whether the conclusions drawn in this research could be applicable to higher Reynolds numbers. It is also expected that at higher Reynolds numbers, the geometric behavior of the canopy would more closely match that seen in a full scale canopy inflation. The higher Reynolds number can be achieved by increasing the freestream velocity and by using larger canopy models. In the testing facilities utilized in this research, the freestream velocity could be increased up to approximately 60 cm/s which would result in a Reynolds number for the 30 cm canopy of 1.8×10^5. The experiments could also be conducted in a wind tunnel which would allow for a larger freestream velocity and therefore a larger Reynolds number. However, performing PIV experiments in air introduces new technical difficulties and the relative stiffness of the canopy would higher in air than in water.

Finally, the results presented here should be used to verify computational fluid dynamic (CFD) models being developed for parachute inflation. This research provides a database of detailed flow field measurements which can be used to verify the results of the CFD models. The fluid-structure interaction models being developed show great promise for being able to predict the flow around a highly flexible body but to date no data has been available for verification purposes.

7. References

Accorsi, M., Lu, K., Leonard, J., Benney, R., and Stein, K., "Issues in Parachute Structural Modeling: Damping and Wrinkling," 15th CEAS/AIAA Aerodynamic Deceleration Systems Technology Conference, Toulouse, France, June 8-11, 1999, AIAA Paper 99-1729.

Balligand, H. and Higuchi, H., "Experimental Investigation of the Wake Behind a Solid Disk," Sandia Report, SAND 90-7083, Dec., 1993.

Berndt, R.J. and DeWeese, J.H., "Filling Time Prediction Approach for Solid Cloth Type Parachute Canopies," Proceedings of AIAA 1st Aerodynamic Deceleration Systems Conference, Houston, TX, September 1966, pp. 17-32.

Berger, E., Scholz, D., and Schumm, M., "Coherent Vortex Structures in the Wake of a Sphere and a Circular Disk at Rest and Under Forced Vibrations," *Journal of Fluids and Structures*, Vol. 4, 1990, pp. 231-257.

Bigon, M. and Regazzoni, G., The Morrow Guide to Knots, trans. Piotrowska, M., Quill, 1982.

Bixby, H.W., Ewing, E.G., and Knacke, T.W., Recovery Systems Design Guide, U.S. Air Force, USAF Report AFFDL-TR-78-151, Dec. 1978.

Carrington, D., "Da Vinci's Parachute Flies," *BBC News Online*, June 27, 2000.

Cockrell, D.J., The Aerodynamics of Parachutes, AGARDograph No. 295, 1987.

DeSantis, G.C., "The Internal and External Flow Field Associated with Parachutes During Inflation," U.S. Army Natick Lab., Technical Report, 1970.

Eaton, J.A., "Added Fluid Mass and the Equations of Motion of a Parachute," *Aeronautical Quarterly*, Vol. 34, Aug. 1983, pp. 226-242.

French, K.E., "Inflation of a Parachute," *AIAA Journal*, Vol. 1, No. 11, Nov., 1963, pp. 2615-2617.

French, K.E., "Model Law for Parachute Opening Shock," *AIAA Journal*, Vol. 2, No. 12, Dec., 1964, pp. 2226-2228.

Fuchs, H.V., Mercker, E., and Michel, U., "Large-Scale Coherent Structures in the Wake of Axisymmetric Bodies," *Journal of Fluid Mechanics*, Vol. 93, Part 1, 1979, pp. 185-207.

Gharib, M., Rambod, E., and Shariff, K., "A Universal time scale for vortex ring formation," *Journal of Fluid Mechanics*, Vol. 360, 1998, pp. 121-140.

Heinrich, H.G. and Noreen, R.A., "Analysis of Parachute Opening Dynamics with Supporting Wind Tunnel Experiments," AIAA 2nd Aerodynamic Deceleration Systems Conference, El Centro, California, Sept. 23-25, 1968, AIAA Paper 68-924.

Heinrich, H.G., "Opening Time of Parachutes Under Infinite-Mass Conditions," *Journal of Aircraft*, Vol. 6, No. 3, May-June, 1969, pp. 268-272.

Heinrich, H.G. and Noreen, R.A., "Analysis of Parachute Opening Dynamics with Supporting Wind-Tunnel Experiments," *Journal of Aircraft*, Vol. 7, No. 4, July-Aug., 1970, pp. 341-347.

Heinrich, H.G. and Hektner, T.R., "Flexibility as a Model Parachute Performance Parameter," *Journal of Aircraft*, Vol. 8, No. 9, Sept., 1971, pp. 704-709.

Heinrich, H.G., "A Linearised Theory of Parachute Opening Dynamics," *Aeronautical Journal*, Dec., 1972, pp. 723-731.

Higuchi, H. and Takahashi, F., "Flow Past Two-Dimensional Ribbon Parachute Models," *Journal of Aircraft*, Vol. 26, No. 7, July, 1989, pp. 641-649.

Higuchi, H., "Visual Study on Wakes Behind Solid and Slotted Axisymmetric Bluff Bodies," *Journal of Aircraft*, Vol. 28, No. 7, July, 1991, pp. 427-430.

Higuchi, H., Anderson, R.W., and Zhang, J., "Three-Dimensional Wake Formations Behind a Family of Rectangular Polygonal Plates," *AIAA Journal*, Vol. 34, No. 6, June, 1996, pp. 1138-1145.

Higuchi, H., Balligand, H., and Strickland, J.H., "Numerical and Experimental Investigations of the Flow Over a Disk Undergoing Unsteady Motion," *Journal of Fluids and Structures*, Vol. 10, No. 7, Oct., 1996, pp. 705-719.

Ibrahim, S.K., "Potential Flowfield and Added Mass of the Idealized Hemispherical Parachute," *Journal of Aircraft*, Vol. 4, No. 2, Mar.-Apr., 1967, pp. 96-100.

Johari, H. and Desabrais, K.J., "Scaling for Solid Cloth Parachutes," 16th AIAA Aerodynamic Deceleration Systems Technology Conference, Boston, Massachusetts, May 21-24, 2001, AIAA Paper 2001-2007.

Karamcheti, K., Principles of Ideal-Fluid Aerodynamics, Robert E. Krieger Publishing, 1980.

Klimas, P.C., "Internal Parachute Flow," *Journal of Aircraft*, Vol. 9, No. 4, Apr., 1972, pp. 313-314.

Klimas, P.C., "Helium Bubble Survey of An Opening Parachute Flowfield," *Journal of Aircraft*, Vol. 10, No. 9, Sept., 1973, pp. 567-569.

Klimas, P.C., "Fluid Mass Associated with an Axisymmetric Parachute Canopy," *Journal of Aircraft*, Vol. 14, No. 6, June, 1977, pp. 577-580.

Klimas, P.C. and Rogers, D.F., "Helium Bubble Survey of a Parachute-Opening Flowfield Using Computer Graphics Techniques," *Journal of Aircraft*, Vol. 14, No. 10, Oct., 1977, pp. 952-958.

Klimas, P.C., "Inflating Parachute Canopy Differential Pressures," *Journal of Aircraft*, Vol. 16, No. 12, Dec., 1979, pp. 861-862.

Knacke, T.W., Parachute Recovery Systems Design Manual, Para Publishing, 1992.

Lamberson, D., Higuchi, H., and van Rooij, M., "Characteristics of Flow within Concave-nosed Bodies," 15th CEAS/AIAA Aerodynamic Deceleration Systems Technology Conference, Toulouse, France, June 8-11, 1999, AIAA Paper 99-1738.

Lee, C.K., "Modeling of Parachute Opening: An Experimental Investigation," *Journal of Aircraft*, Vol. 26, No. 5, May, 1989, pp. 444-451

Lee, C.K, "Radial Reefing Method for Accelerated and Controlled Parachute Opening," *Journal of Aircraft*, Vol. 31, No. 5, Sept.-Oct., 1994, pp. 1124-1129.

Lee, C.K., Natick Soldier Center, Private Communication, 1998.

Lighthill, J., "Fundamentals Concerning Wave Loading on Offshore Structures," *Journal of Fluid Mechanics*, Vol. 173, 1986, pp. 667-681.

Lingard, J.S., "The Aerodynamics of Parachutes During the Inflation Process," Ph.D. thesis, Department of Aeronautical Engineering, University of Bristol, England, October 1978.

Macha, J.M., and Buffington, R.J., "An Experimental Investigation of Wall-Interference Effects for Parachutes in Closed Wind Tunnels," Sandia Report, SAND89-1485, Sept., 1989.

McVey, D.F., and Wolf, D.F., "Analysis of Deployment and Inflation of Large Ribbon Parachutes," *Journal of Aircraft*, Vol. 11, No. 2, Feb., 1974, pp. 96-103.

Müller, W., "Parachutes for Aircraft," National Advisory Committee for Aeronautics, Technical Memorandums, No. 450, October 28, 1927.

Noca, F., "On the Evaluation of Instantaneous Fluid-Dynamic Forces on a Bluff Body," GALCIT Report FM96-5, Aug. 12, 1996.

Noca, F., Shiels, D., and Jeon, D., "A Comparison of Methods for Evaluating Time-Dependent Fluid Dynamic Forces on Bodies, Using Only Velocity Fields and Their Derivatives," *Journal of Fluids and Structures*, Vol. 13, 1999, pp. 551-578.

O'Hara, F., "Notes on the Opening Behavior and the Opening Forces of Parachutes," *Journal of the Royal Aeronautical Society*, Vol. 53, Nov., 1949, pp. 1053-1062.

Panton, R.L., Incompressible Flow, Wiley and Sons, 1996.

Payne, P.R., "A New Look at Parachute Opening Dynamics," *Aeronautical Journal*, Feb., 1973, pp. 85-93.

Pepper, W.B. and Reed, J.F., "Parametric Study of Parachute Pressure Distribution by Wind Tunnel Testing," *Journal of Aircraft*, Vol. 13, No. 11, Nov., 1976, pp. 895-900.

Peterson, C.W., Strickland, J.H., and Higuchi, H., "The Fluid Dynamics of Parachute Inflation," *Annual Review of Mechanics*, Vol. 28, pp. 361-387.

Purvis, J.W., "Theoretical Analysis of Parachute Inflation Including Fluid Kinetics," *Journal of Aircraft*, Vol. 19, No. 4, Apr., 1982, pp. 290-296.

Raffel, M., Willert, C.E., and Kompenhans, J., Particle Image Velocimetry – A Practical Guide, Springer, 1998.

Reddy, K.R., "Unsteady Vortex Flow Past an Inflating, Decelerating Wedge," *Journal of Aircraft*, Vol. 11, No. 7, July, 1974, pp. 427-429.

Roberts, B.W., "Aerodynamic Inflation of Shell Type, Parachute Structures," *Journal of Aircraft*, Vol. 11, No. 7, July, 1974, pp. 390-397.

Roberts, B.W., "Drag and Pressure Distribution on a Family of Porous, Slotted Disks," *Journal of Aircraft*, Vol. 17, No. 6, June, 1980, pp. 393-401.

Sahu, J., Edge, H., Heavey, K., Stein, K., and Benney, R., "Comparison of Numerical Flow Field Predictions for Army Airdrop Systems," 15th CEAS/AIAA Aerodynamic Deceleration Systems Technology Conference, Toulouse, France, June 8-11, 1999, AIAA Paper 99-1715.

Sarpkaya, T., "Methods of Analysis for Flow Around Parachute Canopies," 11th AIAA Aerodynamic Deceleration Systems Technology Conference, San Diego, California, Apr. 9-11, 1991, AIAA Paper 91-0825.

Stein, K.R., "Simulation and Modeling Techniques for Parachute Fluid-Structure Interactions," Ph.D. dissertation, Department of Aerospace Engineering, University of Minnesota, December 1999.

Stein, K., Benney, R., Tezduyar, T., Kalro, V., Leonard, J., and Accorsi, M., "3-D Computation of Parachute Fluid-Structure Interactions: Performance and Control," 15th CEAS/AIAA Aerodynamic Deceleration Systems Technology Conference, Toulouse, France, June 8-11, 1999, AIAA Paper 99-1714.

Stein, K., Benney, R., Kalro, V., Tezduyar, T.E., Leonard, J., and Accorsi, M., "Parachute Fluid-Structure Interactions: 3-D Computation," *Computer Methods in Applied Mechanics and Engineering*, Vol. 190, 2000, pp. 373-386.

Strickland, J.H., "Prediction Method for Unsteady Axisymmetric Flow Over Parachutes," Journal of Aircraft, Vol. 31, No. 3, May-June, 1994, pp. 637-643.

Taylor, G.I., "On the Shape of Parachutes," The Scientific Papers of Sir Geoffrey Ingram Taylor, Volume III, Aerodynamics and The Mechanics of Projectiles and Explosions, edit. Batchelor, G.K., 1963, pp. 26-37.

Taylor, J.R., An Introduction to Error Analysis, 2nd Ed., University Science Books, 1997.

Willert, C.E., and Gharib, M., "Digital Particle Image Velocimetry", *Experiments in Fluids*, Vol. 10, 1991, pp. 181-193.

Wolf, D., "A Simplified Dynamic Model of Parachute Inflation," *Journal of Aircraft*, Vol. 11, No. 1, Jan., 1974, pp. 28-33.

Wolf, D., "Parachute Opening Shock," 15th CEAS/AIAA Aerodynamic Deceleration Systems Technology Conference, Toulouse, France, June 8-11, 1999, AIAA Paper 99-1702.

Yavuz, T., "Determining and Accounting for a Parachute Virtual Mass," *Journal of Aircraft*, Vol. 26, No. 5, May, 1989, pp. 432-437.

Appendix A: Image Processing Routine

The basic canopy geometry was extracted in an automated fashion from the images of the canopy recorded in the experiments. The basic canopy geometry including the canopy diameter, height, cross-sectional area, and estimates of the volume enclosed by the canopy. The image processing routine is shown graphically in Figure A.1. The image process was done using the graphical programming language WiT. The routine shown in Fig. A.1 is the actual program used to process the data in this research.

The processing procedure consisted of thresholding the image into a binary format, then performing a blob detection on the binary image to select the largest blob which represented the image of the canopy. The extents of the blob were then extracted as measures of the canopy diameter and height. The cross-sectional area of the canopy was estimated by counting the number of pixels in the canopy blob. The volume was estimated assuming each column of pixels from the centerline outward in the canopy blob was revolved around the centerline to form a ring. Then the volume of all these rings was summed to estimate the total volume of the canopy. Since this calculation used only half of the canopy in the volume estimate (columns from the centerline of the canopy out), the volume was estimated twice from each side of the canopy centerline. Then the average of these two volume estimates was calculated to give a final best estimate for the volume enclosed by the canopy.

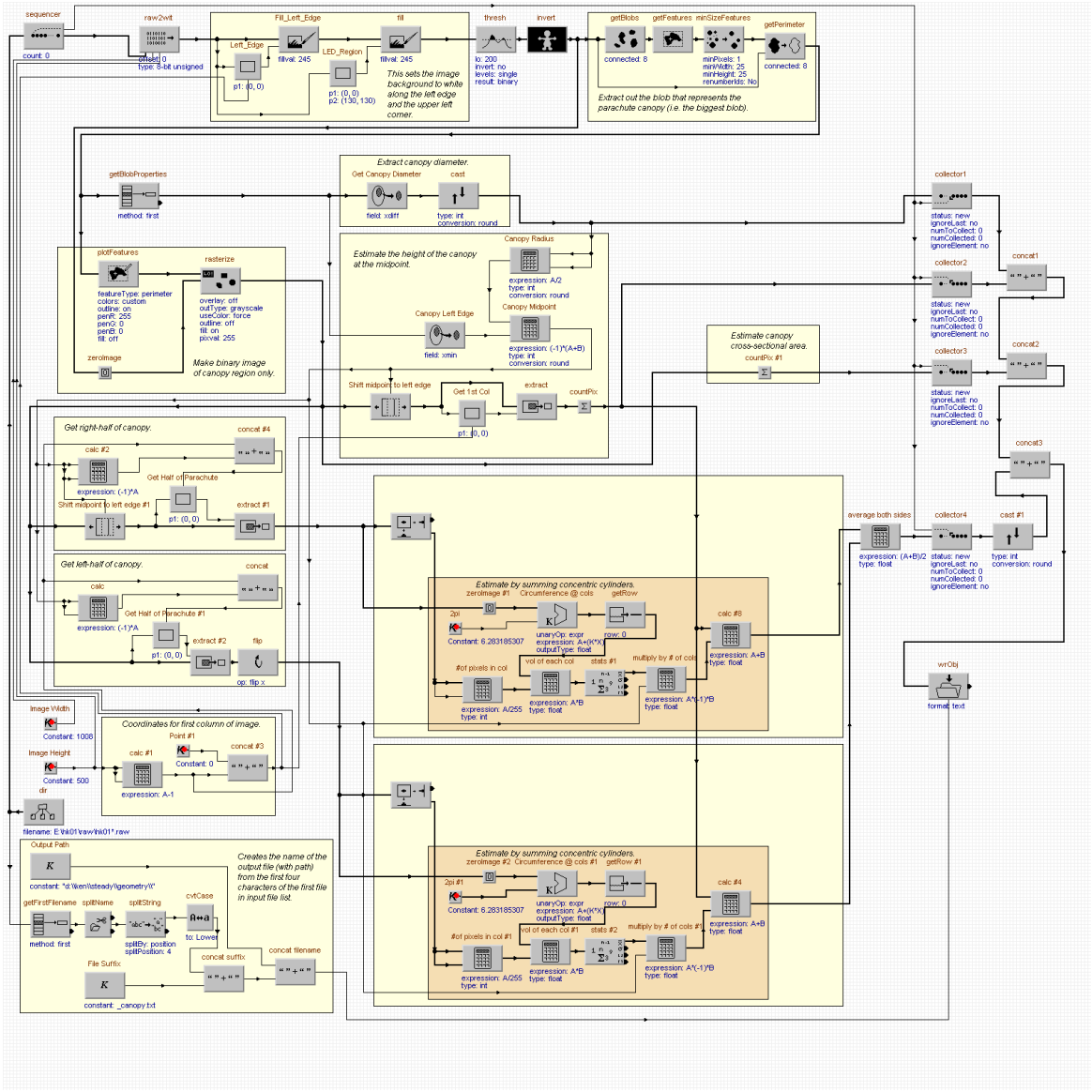

Figure A.1. The image processing routine used to calculate the canopy geometry.

Appendix B: Electrical Wire Diagrams

The output of the load cell was amplified before being measured by a data acquisition system in a computer. The wiring diagram of the amplifier is shown in Fig. B.1. The canopy deployment was controlled by a circuit which synchronized the force measurements with the camera and the stepper motor which pulled the deployment tube. Figure B.2 shows the wiring schematic of the deployment control circuit.

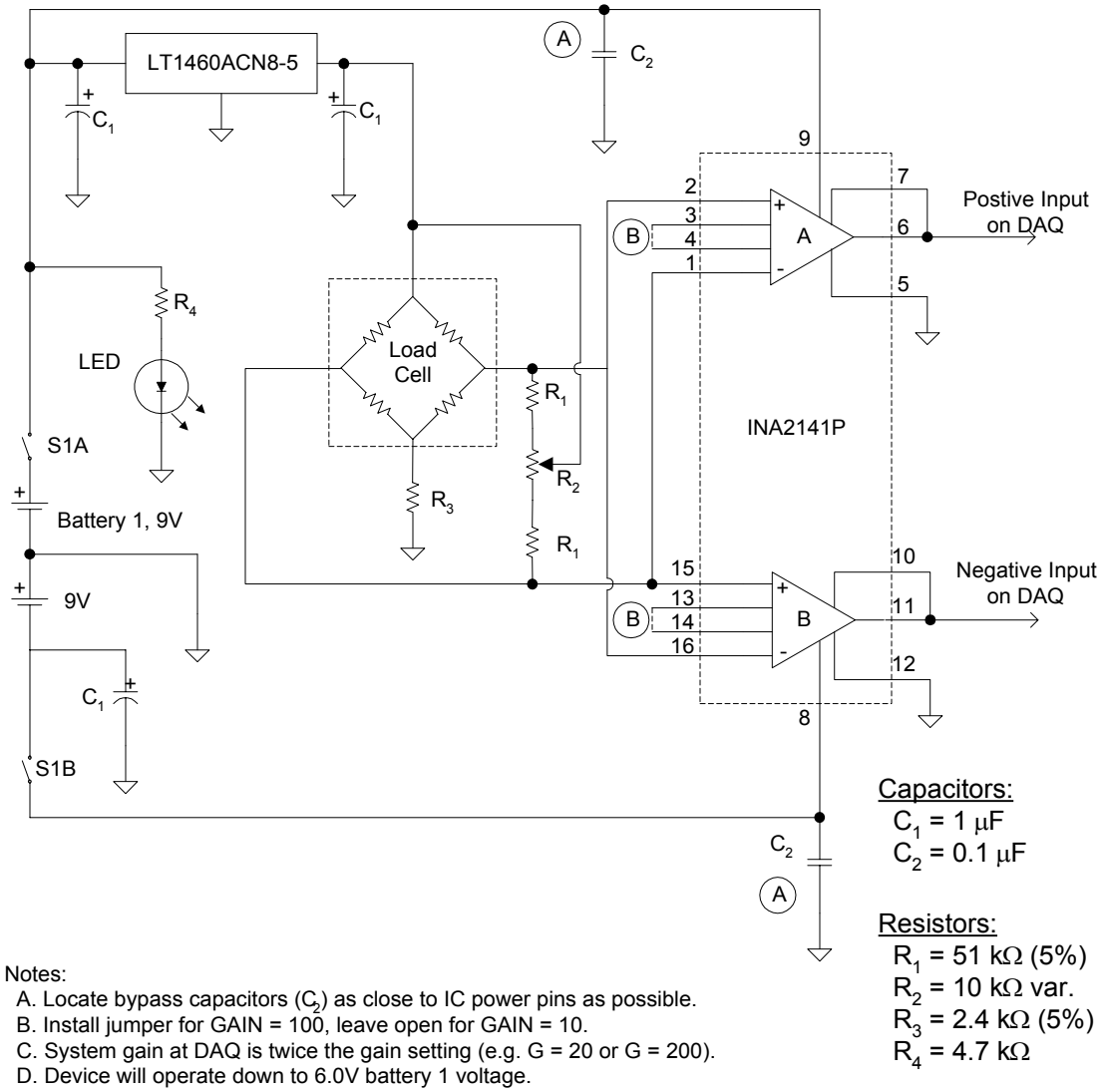

Figure B.1. Wiring diagram of the load cell amplifier.

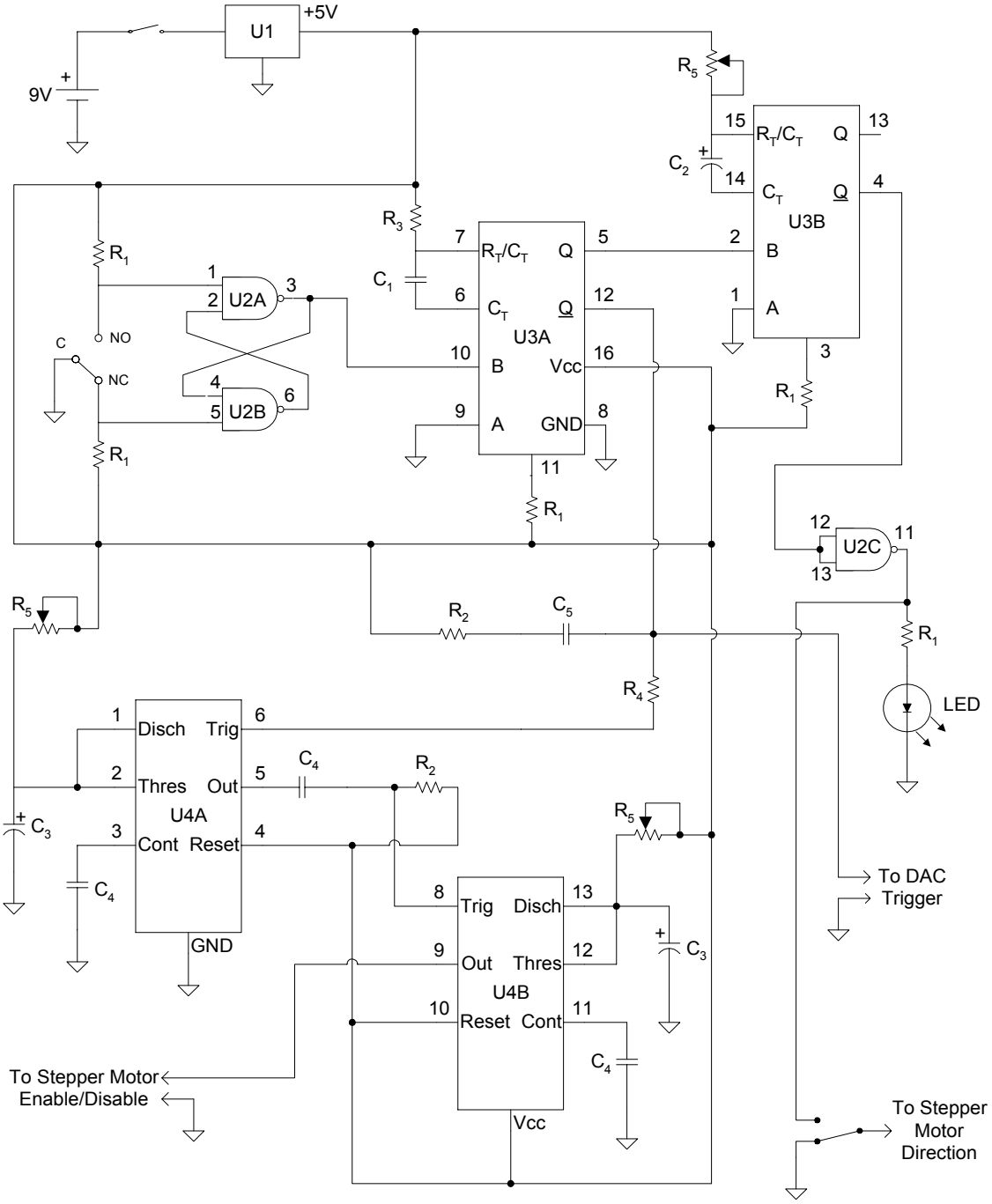

Integrated Circuits:	Resistors:	Capacitors:
U1 = Voltage Regulator	R_1 = 1 kΩ	C_1 = 100 pF
U2 = 74LS00	R_2 = 22 kΩ (5%)	C_2 = 10 μF
U3 = 74LS123	R_3 = 38 kΩ (5%)	C_3 = 100 μF
U4 = NE556	R_4 = 1 MΩ (5%)	C_4 = 0.05 μF
	R_5 = 500 kΩ var.	C_5 = 0.005 μF

Figure B.2. Wiring diagram of deployment control circuit.